Technical University of Denmark

DTU

Improved Internal Reference Oxygen Sensors Using Composite Oxides as Electrodes

Hu, Qiang; Mogensen, Mogens Bjerg; Hansen, Karin Vels

Publication date:
2012

Document Version
Publisher's PDF, also known as Version of record

[Link back to DTU Orbit](#)

DTU Library
Technical Information Center of Denmark

Improved Internal Reference Oxygen Sensors Using Composite Oxides as Electrodes

Dissertation

In partial fulfillment of the requirements
for the degree of Doctor of Philosophy

Qiang Hu

Department of Energy Conversion and Storage

Technical University of Denmark

August 2012

Academic Advisors:

Mogens Mogensen
Department of Energy Conversion and Storage
Technical University of Denmark
DK-4000 Roskilde
Denmark

Karin Vels Hansen
Department of Energy Conversion and Storage
Technical University of Denmark
DK-4000 Roskilde
Denmark

The study was carried out in the time period between September 2009 and August 2012.

Thesis Abstract

The thesis describes the research on and development of an internal reference oxygen sensor (IROS). The IROS is potentiometric and uses the equilibrium pO_2 of the binary mixture of Ni/NiO as the reference pO_2. The sensing electrode of the IROS are made from metallic Pt or the composite of $(La_{0.75}Sr_{0.25})_{0.95}MnO_{3\pm\delta}$ (LSM25) and 8 mol % yttria stabilized zirconia (8YSZ), with/without samaria doped ceria (SDC) impregnation. The composite sensing electrodes are verified superior to Pt in terms of a lower polarization resistance and an extended working temperature range. Cell performance is evaluated comprehensively and the evaluation is targeted to the performance indicators that relate closely to the practical application. IROSes show high accuracy, good stability, fast response, good tolerance to thermal and pO_2 cycling and easy recoverability when Ni is depleted. Both cell fabrication and performance show good reproducibility. Apart from the excellent performance the IROSes are fabricated by an inexpensive and flexible method. Therefore, the IROSes present in this thesis may be commercialized in the future.

Theoretical investigations on IROS are carried out. The electronic leak of an electrolyte made from 8YSZ is evaluated quantitatively and figures that may be used to design the depletion period of an IROS due to the electronic leak of 8YSZ are provided. One dimensional numerical simulations are performed to study the variation in cell voltage during the process of gas mixing, and the asymmetric behavior in cell response is revealed. The errors in pO_2 measurement are analyzed. The temperature dependence of the equilibrium potentials of ten candidates of binary mixtures including Fe/FeO, Pb/PbO, Cr/Cr_2O_3 are evaluated with respect their use in IROSes that are less sensitive to temperature fluctuations.

Electrochemical reduction of NiO is studied. The kinetics of electrochemical reduction of NiO can be described by the Avrami equation. The electrochemical reduction of NiO may require an induction period. The maximum reaction rate is obtained when 2 - 11 % NiO is reduced. The increasing resistance in NiO reduction can be exclusively ascribed to one arc in impedance spectra. The pO_2-dependent part of the resistances of the composite electrodes is determined. SDC impregnation reduces significantly the polarization resistance of the composite of LSM25/8YSZ.

Designs that may extend the application of IROSes are provided. Based on the concepts and fundamentals of the IROS, internal reference sensors that detect other gas species such as hydrogen, chlorine and bromine may be developed.

Dansk resumé

Denne afhandling beskriver udviklingen af en iltsensor med en intern reference elektrode (IROS) og undersøgelser af dens egenskaber. Den interne reference elektrode udnytter det veldefinerede oxygen partialtryk i den binære blanding af Ni og NiO som reference. IROSens måleelektrode er enten en metallisk platin eller en keramisk komposit af $(La_{0.75}Sr_{0.25})_{0.95}MnO_{3\pm\delta}$ (LSM25) og 8 mol % yttria-stabiliseret zirconia (8YSZ) med eller uden imprægnering af samaria-doteret ceria (SDC). Den keramiske måleelektrode udmærker sig ved både at have en lavere polarisationsmodstand og at kunne bruges i et større temperaturinterval – især ved lavere temperaturer - end platinelektroden. IROSen udmærker sig ved stor præcision, god stabilitet, hurtigt respons samt god tolerance over for cykliske temperatur- og pO$_2$-variationer. Desuden kan sensoren nemt regenereres elektrolytisk, når referenceelektrodens Ni-indhold er brugt op. Cellerne er reproducerbare og kan fabrikeres med billige og fleksible metoder. På denne baggrund skønnes det, at denne nyudviklede IROS kan kommercialiseres i fremtiden.

Der er foretaget teoretiske beregninger af den oxygen lækage, der skyldes elektronledningsevnen i en elektrolyt lavet af 8YSZ. Dette er udmøntet i grafer, der kvantitativt kan bruges til at designe en sensor med en forudbestemt levetid. Endimensionale numeriske simuleringer er udført for at studere cellespændingens tidsafhængighed ved gasskift. Her blev den asymmetriske opførsel mellem skift fra højt til lavt oxygenpartialtryk og tilbage tilskrevet potentialets logaritmiske afhængighed af oxygen partialtrykket. Fejlkilderne i pO$_2$-målingerne er blevet analyseret. Temperaturafhængighederne af ligevægtspotentialerne af ti binære metal/metaloxid blandinger, der kan være kandidater til referenceelektroden, er blevet evalueret. Disse inkluderer Fe/FeO, Pb/PbO, Cr/Cr$_2$O$_3$, der alle er mindre følsomme overfor temperaturfluktuationer end Ni/NiO.

Kinetikken i den elektrokemiske reduktion af NiO er undersøgt og kan beskrives med Avrami-ligningen, der beskriver faseomdannelser. Den elektrokemiske reduktion af NiO kan indeholde en induktionsperiode. Den maksimale reaktionshastighed opnås, når mellem 2 og 11 % af NiO er reduceret. Den stigende modstand under reduktionen kan tilskrives en enkelt bue i impedansspektrene. Den pO2-afhængige del af modstanden af den kompositte elektrode er bestemt. SDC-imprægnering kan i signifikant grad reducere polarisationsmodstanden af den kompositte LSM25/8YSZ-elektrode.

Designs, der kan udvide mulighederne for anvendelsen af IROSen, er angivet. På grundlag af principperne for IROS'en, er det muligt at udvikle sensorer med interne referencer, der kan detektere andre gasser, som f.eks. hydrogen, klor og brom.

Preface

This thesis is submitted to the Technical University of Denmark as a partial fulfillment of the requirements for the degree of PhD. The work presented in this thesis was carried out from September 2009 to August 2012 at the Department of Energy Storage and Conversion at the Technical University of Denmark. The work was financed by the Programme Commission on Sustainable Energy and Environment, The Danish Council for Strategic Research, via the Strategic Electrochemistry Research Center (SERC) (www.serc.dk), contract No. 2104-06-0011.

I would like to thank my supervisors:

- Research Professor Mogens Mogensen, Department of Energy Storage and Conversion, for valuable suggestions, discussions and inspiration. I am grateful deeply for his sustained efforts and support and for always having a moment for discussion. He has been a constant source of infinite knowledge and of contagious inspiration, energy and enthusiasm.

- Senior Scientist Karin Vels Hansen, for daily supervision and inspiring discussions. Without her efforts the thesis and my publications would not have been finished. Thank her very much for the training and guidance that she gave to me in the three year study in Denmark.

I am indebted deeply to Torben Jacobsen who has shared his time, attention and ideas to make my study a fruitful and stimulating experience. Without his patience and guidance my research would not have been possible. I benefit so much from him, professionally and personally.

I would also like to record here my appreciation to Martin Søgaard for his provision of the facilities for the long-term stability test of one year. I am grateful to his suggestions and advice during my experiments.

I deeply appreciate all other colleagues at the Department for providing an excellent research environment. Special thanks go to Ming Chen for the valuable discussion on thermodynamics, Karsten Agersted for his help in preparation of the sealing glass, Johan Hjelm for his help in the ink preparation, Eugen Stamate for his help in magnetron sputtering, and YiLin Liu and Karl Tor Sune Thydén for their assistance in SEM.

I appreciate the friendship of Alfred Samson, Mohammed Hussain, Rasmus Rode Mosbæk, Martin Nielsen who have made my stay in the Department enjoyable.

Contents

1 Introduction

This chapter gives a background introduction of oxygen sensors, focusing on internal reference oxygen sensors. The state-of-the-art of the internal reference oxygen sensor is presented with the challenges in developing a reliable cell discussed. Internal reference oxygen sensors have been desired due to the compact structure and flexible installation and application. However, reliable cells are not available so far. A hermetic seal is vital to make an internal reference oxygen sensor functional but it is difficult to realize. Though Pt is the dominate electrode material in oxygen sensors it is possible to replace Pt by ceramics including oxides that have superior performance in terms of electrode activities and tolerance to harsh application conditions.

1.1 Oxygen sensors and their classification

The first commercial oxygen sensor was developed by Bosch in 1976 and now oxygen sensors play a key role in pollution control through automobile engine management, optimization of industrial boilers, steel, cement industries, biological and food processing plants, control of chemical processes and scientific studies [1, 2]. Some oxygen sensors work at ambient conditions where oxygen is either dissolved in some media (liquid or solid) or oxygen measurements have to be made under ambient, low temperature conditions. These conditions exist in medical, food processing and waste management industries. The oxygen sensors used under ambient conditions include Clark type cells [3], paramagnetic cells [4] and optical cells [5, 6]. Most practical applications demand an oxygen sensor to be operated at an elevated temperature from 300 to 1000 ºC. Based on the number of oxygen sensors in service, the predominant use of oxygen sensors is in the control of the ratio of air to fuel, λ, in the combustion engine of automobiles. Due to this wide application oxygen sensors are massively produced. In 1983 Bosch GmbH produced 50 million sets of oxygen sensors and now more than 10 million sets of oxygen sensors are yearly produced for car emission control in Japan [1]. The demand of oxygen sensors in USA from 1996 to 2000 was about 40 million every year, in Europe, it increased from 12 million in 1996 to 25 million in 2002, and in Japan, 6.6 million in 1994 and 7.3 million in 1997 followed by a steady growth. The major oxygen sensor manufactures include Robert Bosch GmbH (Germany), NGK Spark Plug Co. Ltd (Japan), Delphi Automotive Systems (USA), Denso Corp. (Japan) and U-Jecs (Japan) [2].

For high temperature applications oxygen sensors based on ceramics are the most practical. The high temperature oxygen sensors can in general be classified into three kinds: potentiometric cells, amperometric cells

and resistive semiconductor cells. The schematic structures of the thee kinds of cells are shown in Figure 1.1. Potentiometric cells measure the equilibrium voltage of cells according to the Nernst equation. The potentiometric cells need a reference pO_2, p_R and the cell voltage varies logarithmically with the pO_2 at the sensing electrode, p_S. These cells provide reproducible, stable and accurate measurements of even ppm levels of oxygen. Limitations of potentiometric oxygen sensors are their complex structures and these sensors not suitable for engines employing lean burn technology. The amperometric oxygen sensor is also called limiting current amperometric sensor and do not require a reference oxygen volume. By imposing a diffusion barrier, i.e., a small orifice or porous media, between the sample gas and the electrode, an amperometric cell is operated in a diffusion limiting mode. The magnitude of the limiting current is proportional to the rate at which oxygen can diffuse through the diffusion barrier. For a steady diffusion, the limiting current flowing through the cell is linearly dependent on the pO_2 at the sensing electrode. Limitations of amperometric oxygen sensors include the complex packaging and the difficulties in designing and controlling the diffusion barrier. The resistive oxygen sensor is based on semiconductors such as (doped) TiO_2 [7]. The defect concentrations within a resistive oxygen sensor vary exponentially with the pO_2 at the sensing electrode, which causes a corresponding variation in the resistance of the cell. The resistance of the cell can thus be used as a measure of the pO_2 in the sample gas. Limitations of the resistive cells include an unstable output and poor resistance against harsh operation conditions. The base resistance usually drifts with time. The performance of an oxygen sensor typically is evaluated in terms of: sensitivity, selectivity, response time, reproducibility, stability, temperature dependency and power consumption [2].

p_R: pO_2 at the reference electrode
p_S: pO_2 at the sensing electrode

$$R \propto p_s^{\frac{1}{n}}$$

(a): resistive cell
measures the resistance

$$V_{cell} = \frac{RT}{4F} \ln \frac{p_s}{p_R}$$

(b): potentiometric cell
measures the cell voltage

$$I \propto p_s$$

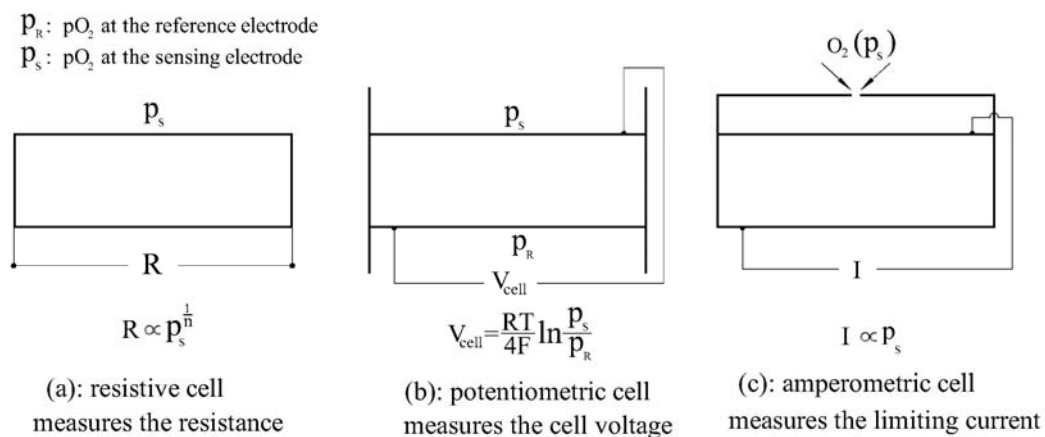(c): amperometric cell
measures the limiting current

Figure 1.1. Schematic structure and working principles of (a)an resistive oxygen sensor, (b) a potentiometric oxygen sensor and (c) an amperometric oxygen sensor. p_R and p_S are the pO_2 at the reference electrode and the sensing electrode, respectively.

1.2 Internal reference oxygen sensors

Potentiometric oxygen sensors work by the Nernst equation:

$$V_{cell} = \frac{RT}{4F} \ln \frac{p_S}{p_R} \tag{1.1}$$

where V_{cell} is the cell voltage, R is the gas constant, 8.314 J·mol^{-1}·K^{-1}, T is the temperature in Kelvin, F is the Faraday constant, 96485 C·mol^{-1}. Potentiometric oxygen sensors use an oxide ion conductor, e.g. stabilized ZrO_2, CeO_2, ThO_2, as the solid electrolyte to separate sample gas from reference gas. Yttria stabilized zirconia (YSZ) is the most commonly used solid electrolyte at present. The cell voltage of a potentiometric oxygen sensor is developed by virtue of the pO_2 difference (strictly speaking, the oxygen fugacity difference) between the two electrodes. The reference gas has been air or pure oxygen at a known pressure or on occasion an equilibrium mixture of reactive gases (e.g. H_2/H_2O or CO/CO_2) for which oxygen partial pressures can be calculated [8, 9]. Figure 1.2 presents the schematic structure of a potentiometric oxygen sensor. The cell needs a thermocouple to detect the cell temperature, T, and an inner tube to deliver the reference air, meanwhile the reference air must be isolated from the sample gas. Delivering the reference gas to the sensor makes the cell structure complex and can become a difficult or impossible task in large industrial equipment applications [9-11].
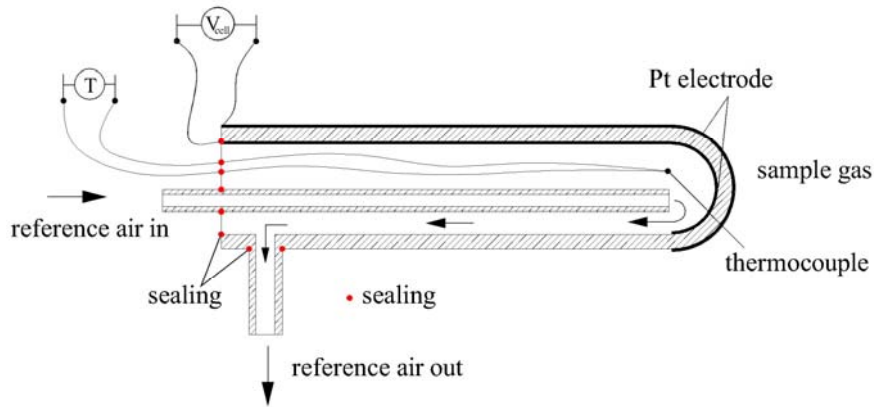
Figure 1.2. Schematic structure of a potentiometric oxygen sensor.

There have been efforts to develop potentiometric oxygen sensors with an internal reference [9-19]. With an internal reference, the cell structure becomes much more compact, which is important to improve mechanical robustness, application adaptability and performance stability of the cell. Haaland [9], Hetrick et al. [14], Maskell et al.[20] and Kaneko et al.[21] fabricated pump-gauge devices that consisted of a pump for transmitting oxygen into a small sealed or semi-sealed volume, and a potentiometric gauge for determining the ratio of the

partial oxygen pressure in the sample gas and in the enclosed volume. The cells were subjected to difficulties such as output stability, accuracy and robustness.

A simple way of providing an internal reference pO$_2$ is by using the equilibrium pO$_2$ of a co-existing mixture of a metal and its oxide. As given by the Gibbs phase rule, a thermodynamically equilibrated mixture of a metal and its stoichiometric oxide fixes a pO$_2$ at a given temperature. Without special statement, the internal reference oxygen sensor (IROS) in this thesis denotes this kind of oxygen sensor. A schematic structure of a planar IROS is presented in Figure 1.3. The cell consists of an internal reference electrode (IRE), an electrolyte, a sensing electrode (SE) and a seal. A hermetic seal is necessary for isolating the internal reference electrode from environments and is crucial to make an internal reference oxygen sensor operational.

1: sensing electrode (SE) 2: electrolyte
3: internal reference electrode (IRE)
4: metalic contacts/coating to the IRE
5: seal   6: metal lead
V$_{cell}$: voltage between IRE/SE, a measure of pO$_2$
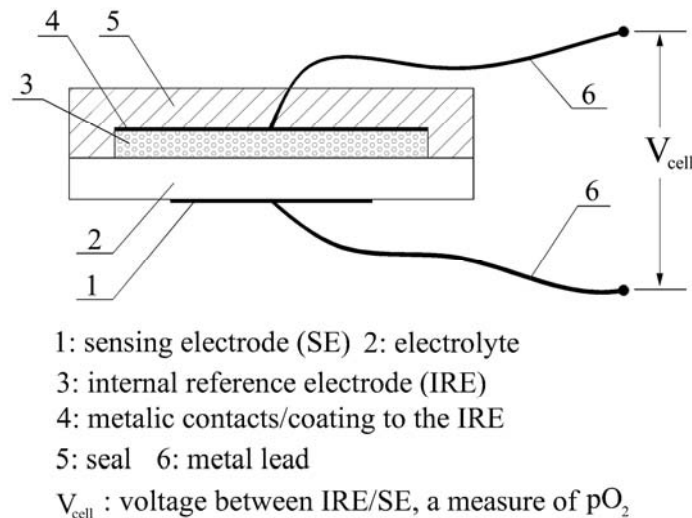
Figure 1.3. Schematic illustration of an IROS. It consists of an IRE, an electrolyte, a SE and a sealing layer. V$_{cell}$ is the voltage between the IRE and the SE, which is used for the pO$_2$ measurement.

The equilibrium pO$_2$ of the binary mixture is usually very small, i.e., the equilibrium pO$_2$ is 5.5×10^{-17} bar at 700 ºC for the binary mixture of Ni/NiO. Such kinds of binary mixture systems have been reviewed by Maskell et al. [8, 22] and several attempts have been carried out to develop IROSes. Monreal et al. [11] developed tubular oxygen sensors which used a Pd/PdO binary mixture to generate an internal reference pO$_2$, Pt or Ag as the sensing electrodes, and a vitrified enamel cap as the seal. Their cells, with the lower detection limit reaching 10^{-39} atm, were able to work with a high accuracy in the tested temperature range from 450 to 650 ºC. Mortimer et al. [10] made tubular IROSes, starting from the binary powder mixtures of Ni/NiO or Pd/PdO. The authors found that the sealing system should be further improved to extend the working life. Chowdhury et al. [16] made a

tubular IROS starting from the mixture of Ni/NiO with a ratio of 9:1. The much larger proportion of Ni was assumed to make enough Ni powder survive the following high temperature treatments such as electrode sintering and cell sealing. For instance, sealing of the sensor was realized at 1400 ºC. van Setten et al. [17] made planar IROSes using Ni/NiO as the binary mixture. The electrode fabrication and sealing were realized by pulsed laser deposition (PLD). The binary mixture of Ni/NiO was *in situ* formed by a coulometric titration technique and the starting material was NiO rather than the mixture of Ni/NiO. Spirig et al. [19] used a special grain boundary sliding technique, which needs pressurized high temperature treatments (> 1200 ºC) for bonding sensor components, to develop several cells with three kinds of binary mixtures (Ni/NiO, Pd/PdO and Ru/RuO$_2$) and Kaneko et al. [23] developed Pd/PdO based cells with the binary mixture embedded into a ceramic superstructure. Apart from the above solid state IROSes, liquid internal reference oxygen sensors were also developed by Kaneko et al. [18] and Zhuiykov [24]. The published stability of IROSes is rarely longer than 100 hrs. The stability was mentioned to be in the order of months for the cells developed by Spirig et al. [19], however, due to the drift problem the cells needed to be operated in a 'pump-out' mode, which is an operation to remove the oxygen from the internal reference electrode, in order to measure the cell voltage during pO$_2$ changes. Thus, IROSes have never been successfully commercialized to an appreciably extent due to reasons such as poor reproducibility, unreliable measurements, costly fabrication and frequent maintenance.

1.3 Sealing of the internal reference electrode and leak sources

A hermetic seal is necessary to isolate the IRE from the external atmosphere. But realizing a hermetic seal has been very difficult. The seal must keep gas tight and survive the harsh conditions such as extremely low/high pO$_2$ levels and fast temperature changes. Challenges also result from matching the thermal expansion of cell components such as electrolyte, IRE and seal, and from realizing an acceptable chemical compatibility among cell components, i.e., effectively mitigating/avoiding the reactions among cell components at an elevated temperature. In most of cases the seal is made of glass and a successfully sealing requires a good wettability of the sealing glass on the IRE. The sealing glass must soften at an approximate temperature with respect to the application condition and the glass sintering temperature. If the sealing glass softens at a temperature much lower than the application temperature it may lose the functionality in practical operations due to deformation. If the sealing glass softens at a very high temperature, i.e., > 1200 ºC, then the undesired reactions between the glass and the IRE may become so serious that the IRE is damaged during the process of glass sintering.

Leakage is believed commonly to be an important reason accounting for the short lifetime of an IROS. The possible leak sources were discussed by Kaneko et al. [21]. Figure 1.4 illustrates the possible leak sources. Leak 1 is due to an electronic conduction of the electrolyte. Though a potentiometric oxygen sensor normally uses an oxide with high ionic conductivity, i.e., doped zirconia, as the electrolyte, a tiny but finite electronic conductivity of the electrolyte is always encountered. The electronic leak of an electrolyte is caused by the diffusion of electronic defects such as electrons and holes of the electrolyte and is a thermal activated process. To meet the condition of electronic neutrality, the diffusion of electrons/holes is accompanied by an oxide ion transfer, which consequently results in an oxygen leak. Leak 2 is caused by the oxygen molecules that permeate through a non hermetic seal or a non dense electrolyte. Leak 3, the electrochemical leak, results from the metallic contacts that are used for sealing and/or electrical connecting the IRE. In some cases metallic foils [21] such as gold foils or a layer of Au/Ag coated by PLD or magnetron sputtering [17] are used to cover the IRE for sealing. If these metallic contacts/coating form a percolating connection for electrons between the IRE and the sections of the electrolyte exposed to the external atmosphere, they can serve as a passage of low resistance for electron transfer. In this case the triple phase boundary (TPB) [25] is thus formed inside and outside the seal and oxygen molecules can then be reduced at the side of high pO_2 and be evolved at the side of low pO_2.

1: sensing electrode   2: electrolyte
3: internal reference electrode (IRE)
4: metalic contacts/coating over the IRE
5: seal   6: metal lead
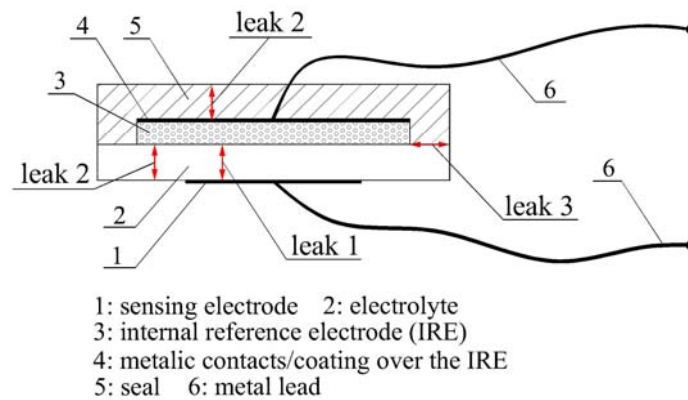
Figure 1.4. Possible leak sources of an IROS. Leak 1: the electronic leak of electrolyte. Leak 2: the oxygen molecule leak due to a non hermetic seal or a non dense electrolyte. Leak 3: the electrochemical leak caused by metallic contacts covering the IRE.

Any leak will cause oxygen to be transferred into or out of the internal reference electrode. One of the functional components of the binary mixture will consequently be consumed, making the IROS gradually lose its functionality. So leaks should be avoided as much as possible. Apparently, leak 2, the oxygen molecule leak, and leak 3, the electrochemical leak, can be avoided if the cell structure design and fabrication are carried out

6

carefully and with sufficient fabrication expertise. For example, a hermetic seal and a dense electrolyte have been reported by several studies [11, 17, 19, 26] . Formation of the TPB is a prerequisite for the electrochemical leak to take place. If all metal contacts to the IRE are carefully fabricated and have no connection to the electrolyte on its course out of the seal, the electrochemical leak can also be avoided. Contrary to the oxygen gas leak and the electrochemical leak, the electronic leak of electrolyte cannot be eliminated as it is an intrinsic characteristic of the oxide serving as the electrolyte. The electronic leak of electrolyte will be discussed and its influence on the lifetime of an IROS will be evaluated in chapter 2 of this thesis.

1.4 Electrode materials

Noble metals such as Pt are dominant electrode material for oxygen sensors due to historical reasons. It is well known that electrode microstructure is important for the sensor performance in terms of stability, response speed and reliability [2, 8, 27-29] and must be carefully designed, realized and maintained to achieve a good performance. However, under practical harsh working conditions (high temperature, dusty and "poisonous" compounds), the microstructure of metal electrodes can hardly be maintained in the long term. On the other hand, since ceramic including oxides is generally refractory in nature and is characteristic of high resistance to severe working conditions, there have been efforts to develop ceramic electrodes for gas sensors. Some perovskites, fluorites and their doped families are known to possess a large range of electronic, ionic and catalytic properties [30-34], which are important for developing the electrode material of gas sensors. Studies have confirmed the superiority in morphology maintenance of $LaMnO_3$, $La(Sr)CoO_3$ and the much better sulfur resistance of terbia doped YSZ in high sulfur (10 - 20 % SO_2) environment over Pt, respectively [27, 35-37]. The composites based on $La_{1-x}Sr_xMnO_{3\pm\delta}$ (LSM) and 8 mol % yttria stabilized zirconia (8YSZ) have a good electrochemical performance and are widely used for the oxygen electrode of solid oxide fuel cell (SOFC) [38-40] and solid oxide electrolysis cell (SOEC) [41, 42], respectively. The properties of these composites are intensively studied with focuses on stability, reproducibility, and electrochemical mechanism and activity [25, 39, 43, 44]. Additional advantages of ceramic electrodes include the relative easiness in electrode microstructure design and cell cost reduction. The cost of ceramic materials is much lower than that of precious metals such as Pt, and ceramic electrode microstructures can be designed to optimize the electrochemical properties of the electrodes [43, 45-48].

1.5 Objective of the thesis

It is known from above that reliable IROSes are not available so far and theoretical studies on IROS, i.e., electrode processes, measurement errors and electronic conduction of the electrolyte are rarely carried out. Though Pt is the dominant electrode material for oxygen sensors, it is possible to replace Pt by ceramics including oxides in order to achieve a superior cell performance. Therefore the objectives of this thesis are to:

1) Develop robust and reliable IROSes that are based on electrodes made from oxides.
2) Comprehensively evaluate cell performance with respect to the practical application.
3) Establish fundamentals of an IROS and investigate the electrode processes of an IROS.

1.6 Thesis layout

The state-of-the-art of IROS is given in this chapter with the challenges in IROS development outlined. Chapter 2 presents theoretical studies of an IROS, focusing on the electronic conduction of the electrolyte, rate of gas mixing, errors in pO_2 measurement and candidates of binary mixtures that may be used to provide the reference pO_2. Fabrication of a functional IROS is shown, step by step, in Chapter 3 and evaluation of cell performance is provided in Chapter 4. The evaluation of cell performance includes the thermal cycling between 25 and 684 °C and a stability test of 8677 hrs, i.e., about one year. Chapter 5 and 6 deal with electrode processes of an IROS. Electrochemical reduction of NiO is discussed in Chapter 5 and the determination of the pO_2-dependent part of the resistance of sensing electrode is shown in Chapter 6. The general discussion and conclusion are given in Chapter 7 and a brief outlook is presented in Chapter 8 where the recommendations for future research on and development of IROS are provided.

References

1. N. Yamazoe, Toward innovations of gas sensor technology, Sens. Actuators, B, 108 (2005) 2-14.
2. R. Ramamoorthy, P. K. Dutta and S. A. Akbar, Oxygen sensors: materials, methods, designs and applications, J. Mater. Sci., 38(2003) 4271-4282.
3. C. Wu, T. Yasukawa, H. Shiku and T. Matsue, Fabrication of miniature Clark oxygen sensor integrated with microstructure, Sens. Actuators, B, 110(2005) 342-349.

4. A. C. Manning, R. F. Keeling and J. P. Severinghaus, Precise atmospheric oxygen measurements with a paramagnetic oxygen analyzer, Global Biogeochem. Cycles 13(1999) 1107-1115.

5. T. Okada and M. Kaneko, Molecular Catalysts for Energy conversion, Springer-Verlag, Berlin (2009).

6. B. J. Basu, A. Thirumurugan, A. R. Dinesh, C. Anandan and K.S. Rajam, Optical oxygen sensors coating based on the fluorescence quenching of a new pyrene derivative, Sens. Actuators, B, 104(2005) 15-22.

7. J. W. Fergus, Doping and defect association in oxides for use in oxygen sensors, J. Mater. Sci., 38(2003) 4259-4270.

8. W. C. Maskell and B. C. H. Steele, Solid state potentiometric oxygen gas sensors, J. Appl. Electrochem., 16(1986) 475-489.

9. D. M. Haaland, Internal-Reference Solid-Electrolyte Oxygen Sensor, Anal. Chem., 49(1977) 1813-1817.

10. A. G. Mortimer and G. P. Reed, Development of a robust electrochemical oxygen sensor, Sens. Actuators, B, 24-25(1995) 328-335.

11. F. J. G. Monreal and G. Vitter, Measurement of low oxygen pressures with a solid-state electrolyte miniaturized sensor, J. Phys. E: Sci. Instrum., 16(1983) 361-364.

12. N. Rajabbeigi, B. Elyassi, A. Khodadadi, S. S. Mohajerzadeh and M. Sahimi , A novel miniaturized oxygen sensor with solid-state ceria-zirconia reference, Sens. Actuators, B, 100(2004) 139-142.

13. N. Rajabbeigi, B. Elyassi, A. A. Khodadadi, S. Mohajerzadeh, Y. Mortazavi and M. Sahimi, Oxygen sensor with solid state CeO_2-ZrO_2-TiO_2 reference, Sens. Actuators, B, 108(2005) 341-345.

14. R. E. Hetrick and W. C. Vassell, Transistor Action Using ZrO_2 Electrochemical Cells, J. Electrochem. Soc., 128(1981) 2529-2536.

15. T. M. Gür and R. A. Huggins, Oxygen sensor, US Patent 5,827,415(1998).

16. A. K. M. S. Chowdhury, S. A. Akbar, S. Kapileshwar, and J. R. Schorr, A Rugged Oxygen Gas Sensor with Solid Reference for High Temperature Applications, J. Electrochem. Soc., 148(2001) G91-G94.

17. E. van Setten, T. M. Gür, D. H. A. Blank, J. C. Bravman and M. R. Beasley, Miniature Nernstian oxygen sensor for deposition and growth environments, Rev. Sci. Instrum., 73(2002) 156-161.

18. H. Kaneko, T. Okamura and H. Taimatsu, Characterization of zirconia oxygen sensors with a molten internal reference for low-temperature operation, Sens. Actuators, B, 93(2003) 205-208.

19. J. V. Spirig, R. Ramamoorthy, S. A. Akbar, J. L. Routbort, D. Singh and P. K. Dutta, High temperature zirconia oxygen sensor with sealed metal/metal oxide inernal reference, Sens. Actuators, B, 124(2007) 192-201.

20. W. C. Maskell, H. Kaneko and B. C. H. Steele, Miniature oxygen pump-gauge. III, Application of a periodic current waveform, J. Appl. Electrochem., 17(1987) 489-494.

21. H. Kaneko, W. C. Maskell and B. C. H. Steele, Miniature oxygen pump-gauge. I. Leakage considerations, Solid State Ionics, 22(1987) 161-172.

22. W. C. Maskell, Progress in the development of zirconia gas sensors, Solid State Ionics, 134(2000) 43-50.

23. H. Kaneko, T. Okamura, H. Taimatsu, Y. Matsuki and H. Nishida, Performance of a miniature zirconia oxygen sensor with a Pd-PdO internal reference, Sens. Actuators, B, 108(2005) 331-334.

24. S. Zhuiykov, 'In situ' diagnostics of solid electrolyte sensors measuring oxygen activity in melts by a developed impedance method , Meas. Sci. Technol., 17(2006) 1570-1578.

25. S. B. Adler, Factors governing oxygen reduction in solid oxide fuel cell cathodes, Chem. Rev., 104(2004) 4791-4843.

26. Q. Hu, T. Jacobsen, K. V. Hansen and M. Mogensen, Improved internal reference oxygen sensor with composite ceramic electrodes. J. Electrochem. Soc., 159(2012) B811-B817.

27. E. L. Brosha, R. Mukundan, D. R. Brown, F. H. Garzon, J. H. Visser, M. Zanini, Z. Zhou and E. M. Logothetis, CO/HC sensors based on thin films of $LaCoO_3$ and $La_{0.8}Sr_{0.2}CoO_{3-\delta}$ metal oxides, Sens. Actuators, B, 69(2000) 171-182.

28. L. Heyne and D. den Engelsen, The speed of response of solid electrolyte galvanic cells for gas sensing, J. Electrochem. Soc., 124(1977) 727-735.

29. J. E. Anderson and Y. B. Graves, The transient response of ZrO_2 oxygen sensors to step changes in gas composition, J. Appl. Electrochem., 12(1982) 335-341.

30. N. Yamazoe and Y. Teraoka, Oxidation catalysis of perovskites - relationships to bulk structure and composition (valency, defect, etc.), Catal. Today, 8(1990) 175-199

31. A. Trovarelli, Catalysis by ceria and related materials, Imperial College Press, London (2002).

32. M. A. Keane, Ceramics for catalysis, J. Mater. Sci., 38(2003) 4661-4675.

33. E. J. Baran, Structural chemistry and physicochemical properties of perovskite-like materials, Catal. Today, 8(1990) 133-151.

34. T. Nakamura, M. Misono and Y. Yoneda, Reduction-oxidation and catalytic properties of $La_{1-x}Sr_xCoO_3$, J. Catal., 83(1983) 151-159.

35. F. H. Garzon, R. Mukundan, R. Lujan and E. L. Brosha, Solid state ionic devices for combustion gas sensing, Solid State Ionics, 175(2004) 487-490.

36. E. L. Brosha, R. Mukundan, D. R. Brown, F. H. Garzon and J. H. Visser, Development of ceramic mixed potential sensors for automotive applications, Solid State Ionics, 148(2002) 61-69.

37. F. H. Garzon, R. Mukundan and E. L. Brosha, Solid-state mixed potential gas sensors: theory, experiments and challenges, Solid State Ionics, 136-137(2000) 633-638.

38. S. M. Haile, Fuel cell materials and components, Acta Materialia 51(2003) 5981-6000.

39. S. P. Jiang, Development of lanthanum strontium manganite perovskite cathode materials of solid oxide fuel cells: a review, J. Mater. Sci., 43(2008) 6799-6833.

40. C. Sun, R. Hui and J. Roller, Cathode materials for solid oxide fuel cells: a review, J. Solid State Electrochem., 14(2010) 1125-1144.

41. A. Hauch, S. D. Ebbesen, S. H. Jensen, and M. Mogensen, Solid oxide electrolysis cells: Microstructure and Degradation of the Ni/Yttria-Stabilized Zirconia Electrode, J. Electrochem. Soc., 155(2008) B1184-B1193.

42. J. E. O'Brien, C. M. Stoots, J. S. Herring and J. Hartvigsen, Hydrogen Production Performance of a 10-Cell Planar Solid-Oxide Electrolysis Stack, J. Fuel Cell Sci. Technol., 3(2006) 213-219.

43. F. Tietz, A. Mai and D. Stöer, From powder properties to fuel cell performance: A holistic approach for SOFC cathode development, Solid State Ionics, 179(2008) 1509-1515.

44. A. Hagen, Y. L. Liu, R. Barfod, and P. V. Hendriksen, Assessment of the Cathode Contribution to the Degradation of Anode-Supported Solid Oxide Fuel Cells, J. Electrochem. Soc., 155(2008) B1047-B1052.

45. V. V. Kharton, F. M. B. Marques and A. Atkinson, Transport properties of solid oxide electrolyte ceramics: a brief review, Solid State Ionics, 174(2004) 135-149.

46. S. P. Jiang, A review of wet impregnation—An alternative method for the fabrication of high performance and nano-structured electrodes of solid oxide fuel cells, Mater. Sci. Eng. A, 418(2006) 199-210.

47. S. P. Jiang and S. H. Chan, A review of anode materials development in solid oxide fuel cells, J. Mater. Sci., 39(2004) 4405-4439.

48. S. P. Jiang, Activation, microstructure, and polarization of solid oxide fuel cell cathodes, J. Solid State Electrochem., 11(2007) 93-102.

2 Theory of the internal reference oxygen sensor

This chapter provides a theoretical analysis of an IROS with an emphasis on the development of cell voltage, depletion period of the internal reference electrode, rate of gas mixing and errors in measurements. The works of this chapter are important for practical cell design and fabrication. Though the analysis is carried out by mathematical modeling, the experimental verification will be seen, at least partially, in the following chapters. Parts of this chapter have been submitted as Q. Hu, T. Jacobsen, K. V. Hansen and M. Mogensen, "The depletion period due to an electronic conduction of the electrolyte of the internal reference oxygen sensor", Solid State Ionics (2012).

2.1 Cell voltage, leak current and depletion period of an IRE

An IROS develops a cell voltage based on the difference in fugacity of oxygen between the internal reference electrode (IRE) and the sensing electrode (SE). This difference in pO_2 between the two electrodes also causes a difference in electrochemical potentials of the charge carriers within the electrolyte. These charge carriers can be electrons, holes and oxide ions, depending on the defect structures of the electrolyte. Driven by the difference in the electrochemical potential, the charge carriers are transferred across the electrolyte. For an IROS to be able to output a cell voltage equal to the thermodynamic value, a "pure" conduction of oxide ions of the electrolyte is necessary. In practice an oxide often has a measurable electronic conductivity (even though it may be very low), which then brings the question of how the electronic conduction of an electrolyte influences the cell voltage of an IROS. More importantly, the electronic conduction is accompanied by a permeation of oxide ions (see section 1.3 of chapter 1), which consumes one of the component of the binary mixture of the IRE. The equilibrium pO_2 of a binary mixture of a non-noble metal and its oxide is generally very low, i.e., the equilibrium pO_2 of Ni/NiO is 5.5 x 10^{-17} bar at 700 °C. In most of cases it is the metal component of the binary mixture that is consumed by the permeating oxide ions. An IROS loses the functionality on the depletion of either of the components of the binary mixture. It is therefore worthwhile investigating the effects of the electronic conduction of an electrolyte on the cell voltage and on the period in which the component of binary mixture is depleted. Due to the prevailing application, 8YSZ and the binary mixture of Ni/NiO are taken as the electrolyte and the IRE, respectively, for the cell studied below.

The structure of an IROS is noted as IRE(O$_2$, p$_R$)|Elyt|SE(O$_2$, p$_S$) with Elyt denoting electrolyte, p$_R$ and p$_S$ designating pO$_2$ at the internal reference and at the sensing electrode, respectively. The concentrations of holes and electrons of 8YSZ are known to be proportional to pO$_2$ to powers of ¼ and -¼ , respectively [1]. Usually the pO$_2$ at the sensing electrode is much larger than the pO$_2$ at the internal reference electrode, p$_S$ >> p$_R$, which results in significant differences in the concentration, and therefore in the chemical potential of electrons and holes within the electrolyte between the interfaces of IRE/Elyt and SE/Elyt. As a result, holes in the electrolyte transfers from the interface of SE/Elyt to the interface of IRE/Elyt and electrons transfers in an opposite direction. To avoid charge accumulation oxide ions simultaneously transfer in the same direction as the holes. These processes are illustrated in Figure 2.1.
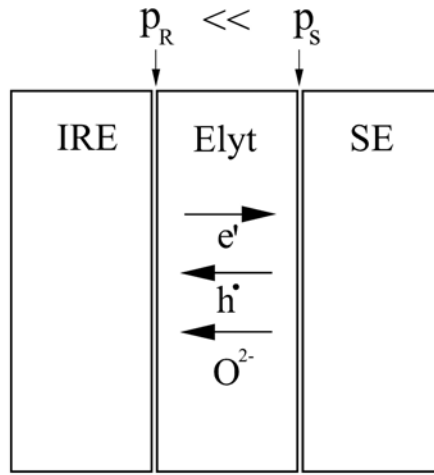

Figure 2.1. Transfer of electrons, holes and oxide ions in the electrolyte of an IROS under a significant difference in pO$_2$ between the interfaces of SE/Elyt and IRE/Elyt. The pO$_2$ at the sensing electrode is assumed to be much larger than the reference pO$_2$, which is quite normal in practice.

Neglecting as usual the cross terms in the transport coefficient matrix [2, 3], the current density of individual charge carriers, i.e., oxide ions, i, electrons, e, and holes, h, can be expressed as:

$$i_k = -\frac{\sigma_k}{z_k F}\nabla\overline{\mu}_k, \ k=i,e,h \tag{2.1}$$

where σ_k, $\overline{\mu}_k$ and z_k are the conductivity, electrochemical potential and charge number of charge carrier k, respectively, and F is the Faraday constant, 96485 C·mol^{-1}. The electrical chemical potential, $\overline{\mu}_k$, is the sum of a chemical part and an electrical part:

13

$$\overline{\mu}_k = \mu_k + z_k F \phi \tag{2.2}$$

where μ_k is the chemical potential of species k and Φ is the Galvani potential. Assume two equilibria of the defect reaction within the electrolyte:

$$\frac{1}{2} O_2 + 2e' \leftrightarrow O^{2-} \tag{2.3}$$

$$e' + h^\bullet \leftrightarrow 0 \tag{2.4}$$

One obtains the corresponding conditions of equilibrium in terms of electrochemical potentials:

$$\nabla \overline{\mu}_e = \frac{1}{2} \nabla \overline{\mu}_{O^{2-}} - \frac{1}{4} \nabla \mu_{O_2} \tag{2.5}$$

$$\nabla \overline{\mu}_e = -\nabla \overline{\mu}_h \tag{2.6}$$

The current carried by the electronic defects of electrons and holes is called leak current in this thesis. The area specific leak current, namely the leak current density, i_{eh}, should be compensated by the current density of oxide ions in the electrolyte, meaning:

$$i_{eh} = -i_i \tag{2.7}$$

From the equations above, the electrochemical potential of electrons, $\overline{\mu}_e$, can be expressed as a function of the chemical potential of oxygen as:

$$\nabla \overline{\mu}_e = -\frac{1}{4} \frac{\sigma_i}{\sigma_e + \sigma_h + \sigma_i} \nabla \mu_{O_2} \tag{2.8}$$

The cell voltage in fact is the difference in the electromotive potential, π, between the two electrodes and the electromotive potential is defined [4] as:

$$\pi = -\frac{\overline{\mu}_e}{F} \tag{2.9}$$

Therefore, in the light of Eq. (2.8), the cell voltage can be calculated by:

$$V_{cell} = \pi_{IRE} - \pi_{SE} \tag{2.10}$$

or

$$V_{cell} = \frac{1}{4F} \int_{SE}^{IRE} \frac{\sigma_i}{\sigma_h + \sigma_e + \sigma_i} d\mu_{O_2} \tag{2.11}$$

Eq. (2.11) shows how the fraction of the total conductivity by the oxide ion influences the cell voltage of an

IROS. It was implied in reference [5] that the term inside the integral of Eq. (2.11), $\dfrac{\sigma_i}{\sigma_h + \sigma_e + \sigma_i}$ is equal to the

transport number of oxide ions, t_i. The transport number of oxide ions is the fraction of total current carried by the oxide ion [6]. For a heavily doped oxide such as 8YSZ, the concentration of oxide vacancies is almost fixed by the concentration of the dopant such as yttria, thus with Eq. (2.1) and the definition of the electrochemical potential in Eq. (2.2), the current density carried by oxide ion can be in fact described as:

$$i_i = -\sigma_i \nabla \phi \tag{2.12}$$

According to Eq. (2.1), (2.6) and (2.12), the transport number of oxide ions in the electrolyte is equal to:

$$t_i = \frac{i_i}{i_i + i_e + i_h} = \frac{\sigma_i}{\sigma_i + \sigma_e + \sigma_h - \dfrac{(\sigma_e + \sigma_h)}{F} \cdot \dfrac{\nabla \mu_e}{\nabla \phi}} \tag{2.13}$$

Thus only if the term of $\dfrac{(\sigma_e + \sigma_h)}{F} \cdot \dfrac{\nabla \mu_e}{\nabla \phi}$ is negligible Eq. (2.11) can be approximated as:

$$V_{cell} = \frac{1}{4F} \int_{SE}^{IRE} t_i d\mu_{O_2} \tag{2.14}$$

However in an IROS the gradient of the chemical potential of electrons is large and the gradient of the Galvani potential is rather small (see below), it is thus risky to calculate the cell voltage by Eq. (2.14) even the term of $\dfrac{(\sigma_e + \sigma_h)}{F}$ is small.

If the conductivity of oxide ions is dominant, meaning $\sigma_i \gg (\sigma_e + \sigma_h)$, and the fugacity of oxygen is equal to oxygen partial pressure, Eq. (2.11) can then be approximated by the well-known Nernst equation:

$$V_{eq} = \frac{RT}{4F} \ln \frac{p_S}{p_R} \tag{2.15}$$

where V_{eq} is the Nernst equilibrium cell voltage. If the electrolyte is made from ceria or doped ceria that are well-known mixed conductors of oxide ion and electrons/holes [7], the cell voltage will be numerically lower than the equilibrium voltage V_{eq} to an noticeable extent. If the electrolyte is made from doped zirconia, i.e., 8YSZ, a "purely" ionic conductor, the cell voltage will be very close to the equilibrium voltage.

Neglecting electrode polarizations of both electrodes and in the light of Eq. (2.1) to (2.6), the leak current density, i_{eh}, can be calculated by:

$$i_{eh} = \frac{\sigma_e + \sigma_h}{F} \nabla \overline{\mu}_e \tag{2.16}$$

15

which may be alternatively expressed in terms of the cell voltage of Eq. (2.14) and the equilibrium voltage of Eq. (2.16) [8, 9]:

$$i_{eh} = -\sigma_i \frac{V_{eq} - V_{cell}}{L} \qquad (2.17)$$

where L is the electrolyte thickness.

The leak current causes a permeation of oxygen, which results in the oxidation of Ni in the IRE:

$$Ni + O^{2-} \leftrightharpoons NiO \qquad (2.18)$$

Neglecting the kinetics of the oxidation reaction, Ni in the IRE is consumed at a rate R_{Ni}, in a unit of mol·m^{-2}·s^{-1},

$$R_{Ni} = \frac{i_{eh}}{2F} \qquad (2.19)$$

Let $N_{Ni,IRE}$ be the area specific load of Ni of the IRE, then Ni will be exhausted in a period of time, τ, which is equal to:

$$\tau = \frac{N_{Ni,IRE}}{i_{eh}} \qquad (2.20)$$

The period of time, τ, will hereafter be referred to as the depletion period. It needs to be noted that the above calculations do not take in account the resistances from electrode processes, i.e., oxygen molecules dissociation, incorporation and evolution of oxide ions at the interface of electrode/electrolyte, and the resistance of the reaction of Ni oxidation. So the above calculation gives a conservative estimation of the depletion period. The practical depletion period should be longer than the estimated above.

Eq. (2.11) is the key equation to determine the cell voltage, the leak current density and the depletion period. The conductivities inside the integral are functions of the concentration of the charge carriers:

$$\sigma_k = u_k c_k |z_k| F, k = i, e, h \qquad (2.21)$$

where c_k, and u_k are the concentration (mol·m^{-3}) and mobility (m^2·V^{-1}·s^{-1}) of charge carrier k. Solutions for Eq. (2.11) and Eq. (2.17) have been given by T. Jacobsen et al., [4] and H. Näfe [8, 9], respectively, and both solutions agree well on results [10].

The below presents the results based on the solution provided by H. Näfe [8, 9] and the calculation was carried out with assumptions of an electrolyte made of 8YSZ and an IRE with the Ni load of 0.1 mmol·cm^{-2}. The electronic properties of 8YSZ measured by Park et al. [1] are experimentally valid in the temperature range 800

– 1050 °C and the pO_2 range of 10^{-7} – 0.21 bar, but extrapolations of the formulae were used in calculations. The Ni load of 0.1 mmol·cm^{-2}, is typical in the cells shown in this thesis.

Figure 2.2 presents profiles of the electromotive potential and the Galvani potential as functions of the relative location in the electrolyte, x/L. Note the Galvani potential is in a unit of microvolt (μV). The electrolyte thickness is 200 μm and IRE and SE locate at the right and left sides, respectively. The electromotive potential and the Galvani potential of the IRE are taken as references. The calculation gives a leak current density of 0.01 mA·cm^{-2}. The profile of Galvani potential is linear, showing a constant ionic conductivity. The Galvani potential varies slightly, less than 7 μV, across the electrolyte and the cell voltage is actually equal to the equilibrium cell voltage, 705 mV. The electromotive potential varies significantly in a narrow section close to the IRE.
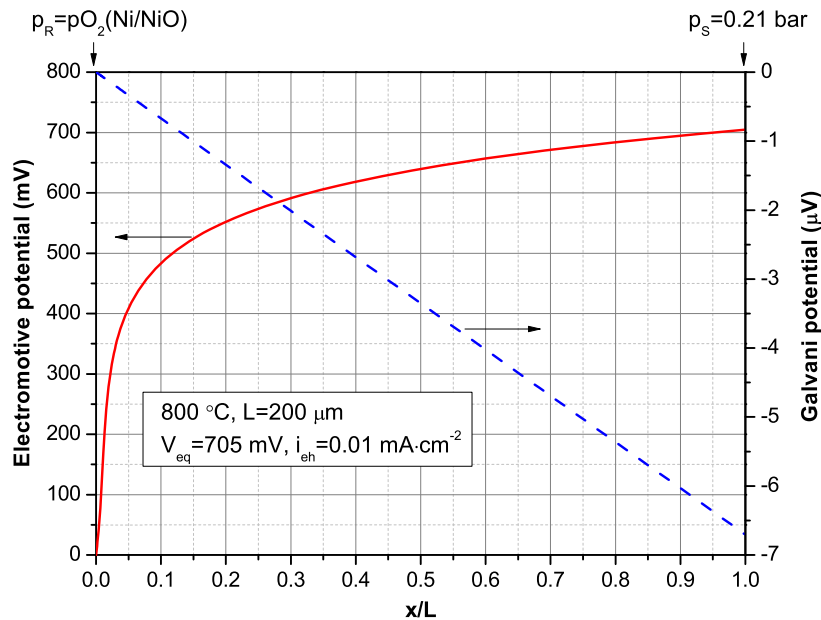

Figure 2.2. Profiles of the electromotive potential and the Galvani potential across the electrolyte of an IROS. "x/L" is the relative location in the electrolyte. The reference pO_2, p_R, is the equilibrium pO_2 of the binary mixture of Ni/NiO at 800 °C and the pO_2 at the sensing electrode, p_S, is 0.21 bar. The electromotive potential and the Galvani potential of the IRE are taken as references.

Figure 2.3 shows profiles of the concentrations of electrons and holes. The calculation conditions are same as those of Figure 2.2. The hole concentration increases, while the electron concentration decreases towards the interface of SE/Elyt. Except in a very narrow section close to the IRE, the hole concentration is much larger than

the electron concentration. Corresponding to the profiles of electromotive potential in Figure2.2, the concentrations of electrons and holes vary significantly in a narrow section close to the IRE.
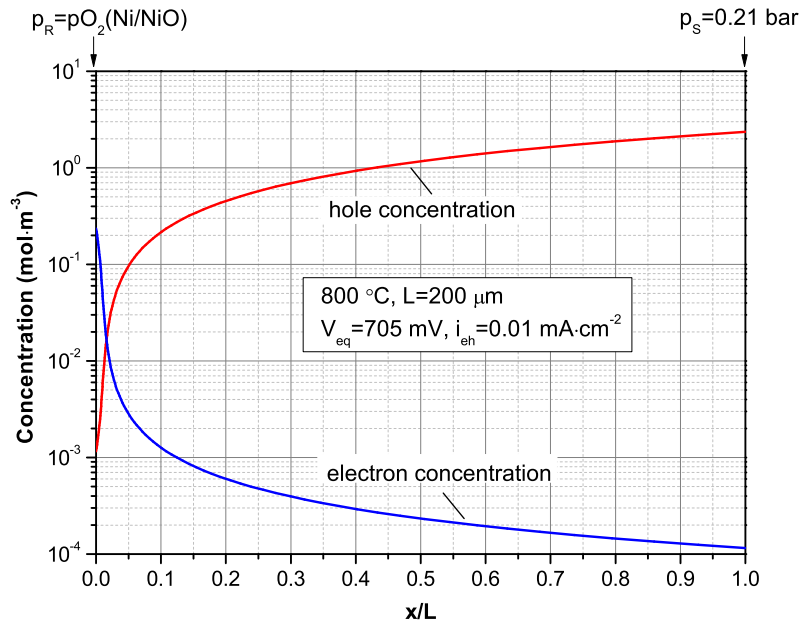

Figure 2.3. Profiles of electron concentration and hole concentration across the electrolyte of an IROS. "x/L" is the relative location in the electrolyte. The hole concentration increases, while the electron concentration decreases towards the interface of SE/Elyt. Both concentrations vary significantly in a narrow section close to the IRE.

Figure 2.4 shows the effects of electrolyte thickness on the leak current density in a temperature range of 500 - 800 °C. The leak current density decreases with increasing electrolyte thickness, and the higher the temperature the larger is the leak current density. Considering the fact that the diffusivity of holes is about 10 times larger than that of electrons in 8YSZ [1] and the fact that the hole concentration is much larger than the electron concentration in most parts of the electrolyte (see Figure 2.3), the electronic conduction in 8YSZ is mainly carried out by hole diffusion. Meanwhile, the Galvani potential gradient is very small in an oxide ion conductor such as 8YSZ (see Figure 2.2), hence the electrochemical potential of holes in Eq. (2.1) can by approximated by the chemical potential of holes. Therefore the leak current density can be estimated from the diffusion flux of holes. For example, by estimating the concentration gradient of holes from the difference in concentration at the interfaces of IRE/Elyt and SE/Elyt, divided by the electrolyte thickness, and along with the hole diffusivity, the diffusion flux of holes can be obtained and it gives the equivalent leak current density of 0.0104 mA·cm^{-2} for the condition of Figure 2.3. Taking into account the electron conduction, the numerical calculation gives a leak

current density of 0.0107 mA·cm^{-2} for the identical conditions. The difference caused by ignoring electron conduction is actually very small.
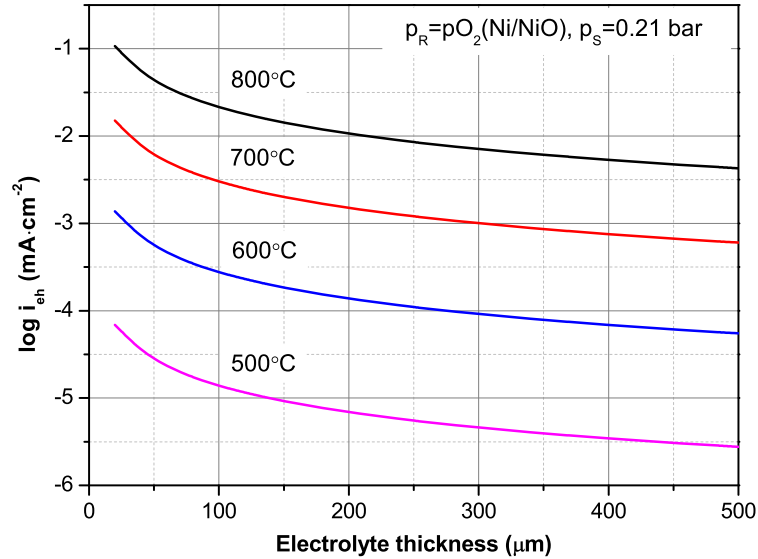

Figure 2.4. Leak current density as a function of electrolyte thickness and temperature. The electrolyte is assumed to be made from 8YSZ.

Figure 2.5 shows the depletion period as a function of temperature and the pO$_2$ at the sensing electrode, p$_S$, with 0.5, 1 and 2 year(s) indicated. The Ni load is 0.1 mmol·cm^{-2} and the electrolyte thickness is 200 μm in the calculation. The depletion period that decreases with increasing temperature is approximately proportional to the pO$_2$ at the sensing electrode to a power of -¼, i.e. $\tau \propto p_S^{-1/4}$. Figure 2.6 presents the depletion period as a function of electrolyte thickness and temperature with an assumption that the pO$_2$ at the sensing electrode is 0.21 bar. The depletion period increases with increasing the thickness of the electrolyte. From Figure 2.5 and 2.6, it appears that the depletion period of an IROS in fact can be designed to satisfy the requirement of a target application. Suppose an IROS is to be used at 700 °C and the pO$_2$ at the sensing electrode usually varies around 0.21 bar, then, as known from Figure 2.6, the electrolyte thickness needs to be larger than 250 μm to achieve a life time of at least a half year. If the pO$_2$ at the sensing electrode is different from 0.21 bar, one then needs to refer to Figure 2.5 for further designs. Figure 2.5 and 2.6 are calculated for a Ni load of 0.1 mmol·cm^{-2} but in practice the Ni load may be varied. As the depletion period is proportional to the Ni load as indicated by Eq. (2.20), the depletion period predicted by Figure 2.5 and 2.6 can be increased by increasing the amount of Ni in the IRE.

Different methods may be used to change the Ni load of an IRE. However if the cell fabrication starts directly from the powder mixture of Ni and NiO, it will be difficult to realize an expected Ni load in the fabricated cells, since the inadvertent oxidation of Ni during cell fabrication such as the sealing and electrode sintering at a high temperature such as 1300 °C is unavoidable. If the binary mixture of Ni/NiO is generated *in situ* by electrochemical reduction of NiO that is the method used in this thesis, the Ni load can then be readily and sophisticatedly controlled by adjusting the reduction current and time.

The depletion period predicted by the calculations above is verified, at least partly, by the stability test shown in chapter 4. The cell of the stability test had a Ni load of 0.09 mmol·cm^2 and an electrolyte thickness of 200 μm. The cell maintained a cell voltage very close to the theoretical value for a period longer than 6600 h and the predicated depletion period is $> 10^4$ h, i.e. the experimental result is in accordance with the prediction.
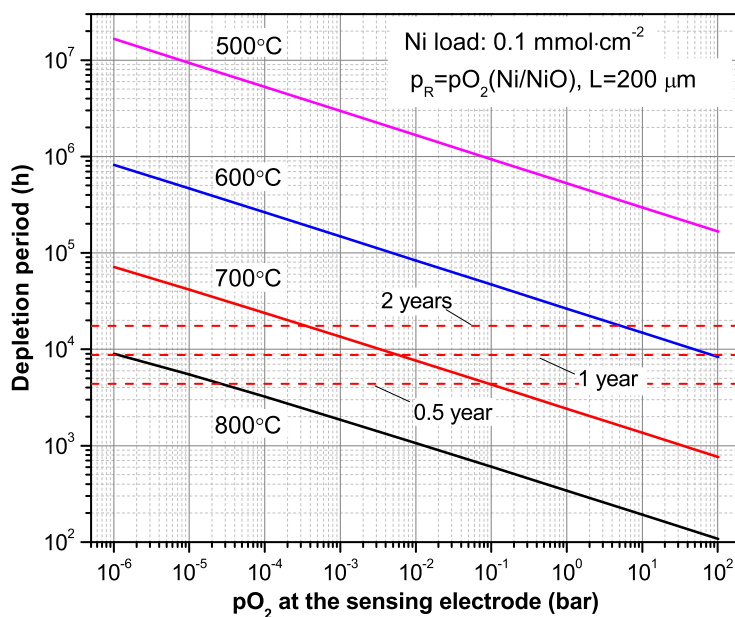

Figure 2.5. Depletion period as a function of temperature and the pO$_2$ at the sensing electrode with 0.5, 1 and 2 year(s) indicated.
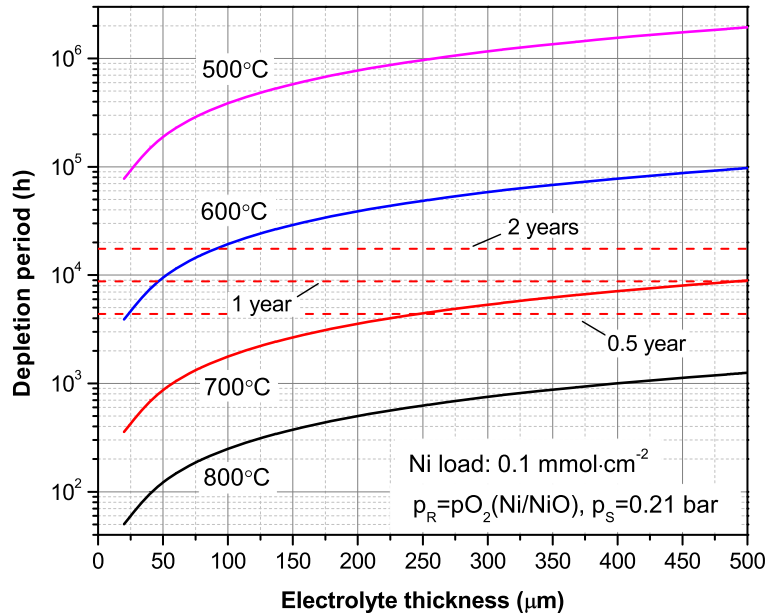
Figure 2.6. Depletion period as a function of electrolyte thickness and temperature with 0.5, 1 and 2 year(s) indicated.

2.2 Gas mixing and the corresponding variation in cell voltage

In practice oxygen sensors are installed in an setup. The time the entire cell setup takes to respond to a pO_2 change is important for real applications and consists of two parts: the response time of the setup and the response time of the cell. In this section only the response time of a simplified tube setup is considered. As the response time of a cell is determined by the rate of electrode processes taking place at a specific sensing electrode, it will be discussed later in chapter 7, after the determination of the resistance of the sensing electrodes used in this thesis.

Suppose an IROS is installed in a tube as illustrated in Figure 2.7 and the distance from the cell position to the inlet is z. Initially, t = 0, a gas mixture is flowing through the tube with a rate of u_G and the pO_2 at the inlet is pO_2^0. At a time t, t > 0, the gas composition at the inlet is changed from the initial value of pO_2^0 to a new value of $pO_{2, in}$. The response time of the setup is for this case defined as the time it takes for the pO_2 at the cell

position to reflect the new inlet condition, $pO_{2, in}$. Apparently, the response time of the setup depends on the design of the setup, i.e., the gas flow rate and the position where the cell is installed, and is in fact determined by the rate of gas mixing. Provided the electrode processes at the sensing electrode are fast enough so that it equilibrates always with the local pO_2, one would also like to know how the cell voltage varies during the process of gas mixing, i.e., the characteristics of the variation in cell voltage during the process of gas mixing.

As described by Bird et al. [11], the process of gas mixing is realized via gas motions of convection and diffusion. For the gas diffusions taking place in a gas mixture, the diffusion flux of individual gas species couples with each other and can be described by the dusty gas model (DGM) [12-16]. A code is hereby developed to simulate numerically the process of gas mixing and the corresponding variation in cell voltage. The details of the numerical simulation are given in the appendix of this chapter and the below presents only simulation results. For the reason of convenience the variation in pO_2 is shown by the equivalent variation in the molar fraction.
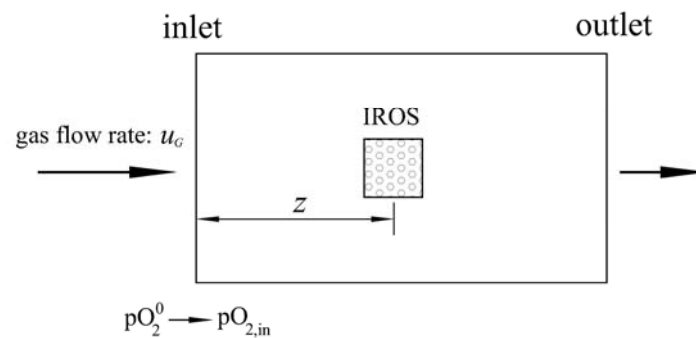

Figure 2.7. Schematic illustration of an IROS setup. An IROS is installed inside a tube and the distance from the cell position to the inlet is z. The pO_2 at the inlet is changed from the initial value pO_2^0 to a new value $pO_{2, in}$.

Figure 2.8 presents the variations in oxygen fraction during a cycling of oxygen fraction between 0.2 and 0.024, and the gas flow rate is 8.9 mm·s^{-1}. The gas mixing is seen to complete in about 30 seconds and the variations are symmetrical, meaning that the gas mixings are finished in an equal period and with an equal rate regardless the change direction of oxygen fraction, i.e., from high to low or vice versa. Figure 2.9 shows the variations in oxygen fraction during the same cycling of oxygen fraction but the gas flow rate is lower, 1.2 mm·s^{-1}. The variations of oxygen fraction are also symmetric, but the gas mixing does not complete even after 200 seconds. The gas flow rate has a substantial influence on the response time of a setup.
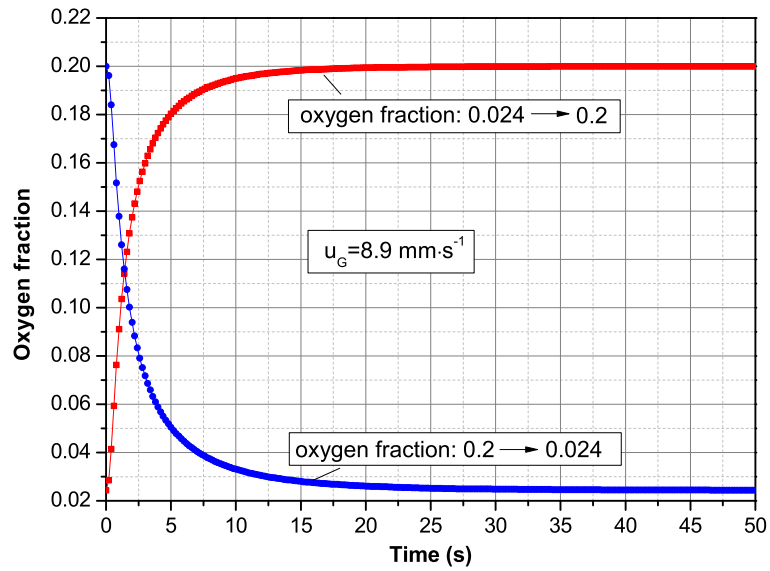
Figure 2.8. Variations in oxygen fraction during a cycling of oxygen fraction between 0.024 and 0.2. The gas flow rate is 8.9 mm·s⁻¹. The variations are symmetrical, meaning that the gas mixings are finished in an equal period and with an equal rate regardless the change direction of oxygen fraction.
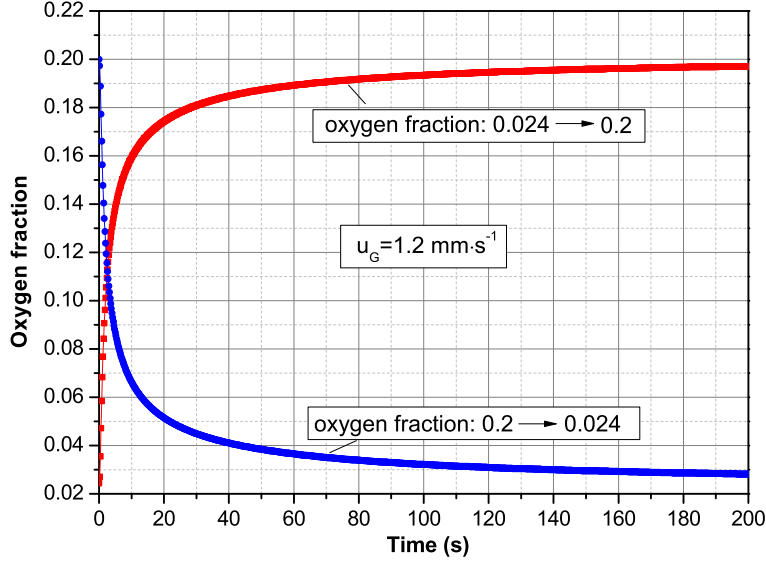
Figure 2.9. Variations in oxygen fraction during an oxygen fraction cycling between 0.024 and 0.2. The gas flow rate is 1.2 mm·s^{-1}. The gas mixing is finished in a much longer period due to the decreased gas flow rate.

Figure 2.10 shows the variation in cell voltage during the gas mixings shown in Figure 2.8. Noticeably, the symmetrical variations of oxygen fraction shown in Figure 2.8 manifest themselves asymmetrically in the plot of cell voltage. When the oxygen fraction is changed from low to high, the initial variation in cell voltage is more rapid than that in the inverse change, which is caused by the logarithmic dependence of the cell voltage on the pO_2 at sensing electrode. Differentiating the cell voltage in the Nernst equation of Eq. (2.15) with respect to the time, one has:

$$\frac{dV_{cell}}{dt} = \frac{RT}{4F} \cdot \frac{1}{p_S} \cdot \frac{dp_S}{dt} \tag{2.22}$$

where $\frac{dp_S}{dt}$ is the variation rate of the pO_2 at the sensing electrode. Note the variation rate of cell voltage, $\frac{dV_{cell}}{dt}$, depends inversely on the pO_2 at the sensing electrode. Therefore a lower p_S will result in a higher variation rate. Changing pO_2 from the fraction of 0.024 to 0.2, the initial variation rate of the cell voltage is more than 8 times larger than that in the inverse process. It must be pointed out that the variation in oxygen fraction during gas mixing is asymptotical and the exact time for a complete gas mixing is difficult to be identified.

24

From Eq. (2.22) the variation rate of cell voltage, $\dfrac{dV_{cell}}{dt}$, is seen to have a dependence on the cell temperature, indicated by the term $\dfrac{RT}{4F}$. Compared with the pO$_2$ at the sensing electrode that can vary by several orders of magnitude, the cell temperature varies in a rather limited extent, which means that the dependence of the variation rate of cell voltage on temperature will be weak. For example, increasing the cell temperature from 521 to 663 °C, the term $\dfrac{RT}{4F}$ increases slightly from 0.017 to 0.020. Figure 2.10 presents the variations in cell voltage when oxygen fraction changes from 0.024 to 0.2 at two cell temperatures, 521 and 663 °C. The variations of cell voltage are seen to finish in an (almost) equal period and with an (almost) equal rate.

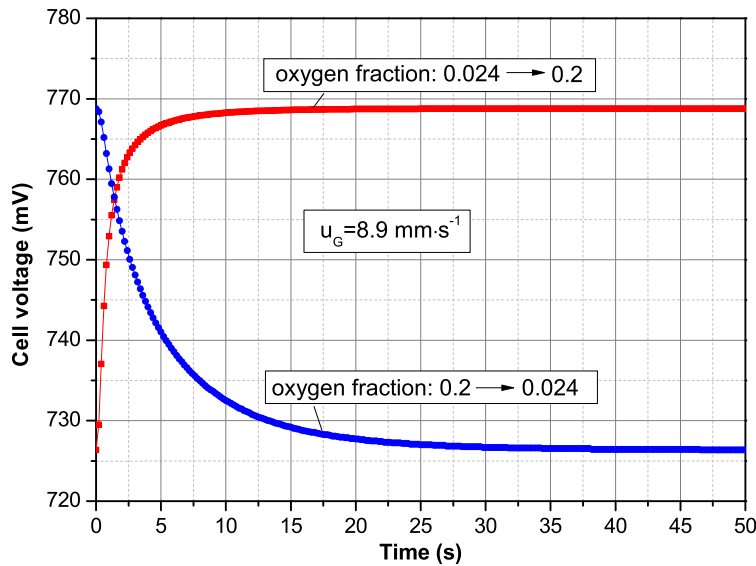Figure 2.10. Variations in cell voltage during the cycling of oxygen fraction between 0.024 and 0.2. The gas flow rate is 8.9 mm and the corresponding variations in oxygen fraction are shown in Figure 2.8. The variations of cell voltage appear asymmetrical and the initial variation rate of cell voltage, when oxygen fraction is changed from low to high, is larger than that in the inverse change.
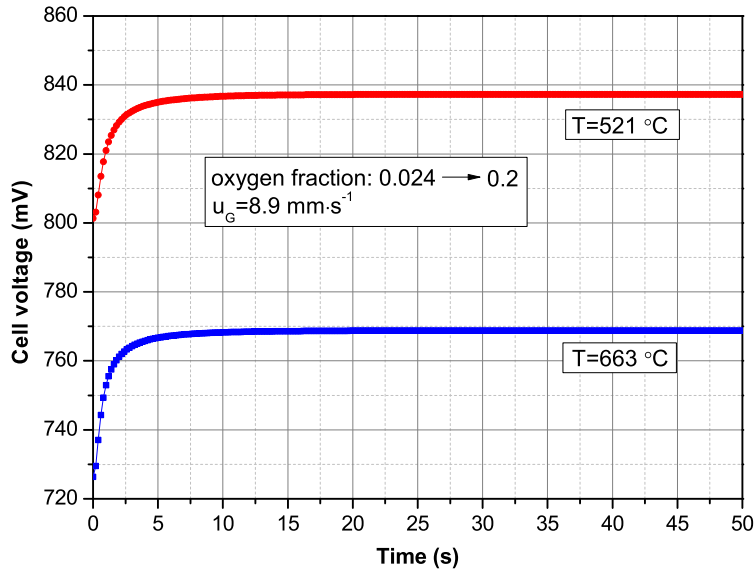
Figure 2.11. Variations in cell voltage at two cell temperatures, 521 and 663 °C. The oxygen fraction is changed from 0.024 to 0.2. The variation of cell voltage depends weakly on the cell temperature.

2.3 Measurement errors

2.3.1 Measurement error caused by voltage error

A potentiometric oxygen sensor including the IROS measures the pO_2 at sensing electrode by acquiring the cell voltage between the two electrodes. The pO_2 at the sensing electrode is calculated by:

$$p_S = p_R \exp(-\frac{4FV_{cell}}{RT})$$

(2.23)

A voltage error, if any, will be transferred to the determination of the pO_2 at the sensing electrode. Assuming that a voltage error, ΔV, exists and the correct cell voltage is V_{cell}, then the incorrect pO_2 at the sensing electrode, p_S', will be calculated to be:

$$p_S' = p_R \exp[-\frac{4F(V_{cell} + \Delta V)}{RT}]$$

(2.24)

The above equation is equivalent to:

26

$$p_S^{'} = p_S \exp(-\frac{4F\Delta V}{RT}) \qquad (2.25)$$

Therefore, the relative error in the pO$_2$ measurement, $\varepsilon = \dfrac{p_S^{'} - p_S}{p_S} \times 100\%$, is:

$$\varepsilon = [\exp(-\frac{4F\Delta V}{RT}) - 1] \times 100\% \qquad (2.26)$$

Figure 2.12 shows the relative error in pO$_2$ measurement, ε, as a function of the voltage error, ΔV, at a three temperatures, 500, 600 and 700 ºC. The error increases with decreasing temperature, and the voltage error has a significant influence as it takes a position in the exponent in Eq. (2.26). A small error in cell voltage such as 1 mV gives an error of 5 % in the pO$_2$ measurement at 600 ºC. Noticeably the curves in Figure 2.12 are not symmetrical in case of a large voltage error, meaning that the error is sensitive to the sign of voltage error. For example, at 600 ºC a voltage error of -6 mV results in an error of 38 % but a voltage error of 6 mV gives an error of -27 %.
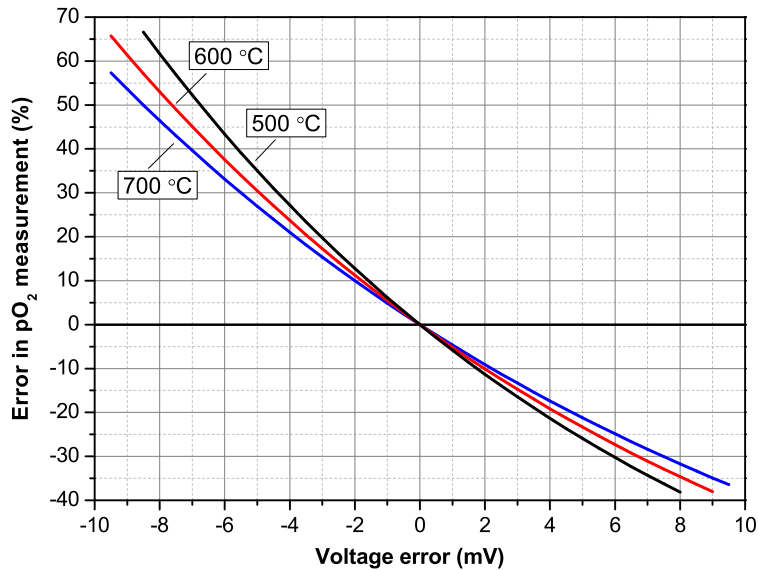

Figure 2.12. The relative error in pO$_2$ measurement due to the voltage error at three temperatures, 500, 600 and 700 ºC.

2.3.2 Voltage error caused by temperature error

Due to the significant influence of voltage error on a pO₂ measurement, the factors causing a voltage error must be examined carefully. For example the IROSes operated at a low temperature such as 300 ºC or the cells equipped with a thick electrolyte such as 1 mm have a large cell resistance. In this case, the voltmeter reading the cell voltage must have a large enough input resistance so that the voltmeter does not affect the cell voltage during measurement.

According to Eq. (2.15), temperature has an influence on cell voltage and the influence can be investigated by differentiating the cell voltage versus temperature:

$$\frac{dV_{cell}}{dT} = \frac{R}{4F}\ln\frac{p_R}{p_S} + \frac{RT}{4F}\frac{d\ln p_R}{dT} \tag{2.27}$$

Unlike the potentiometric oxygen sensor with an air reference, the reference pO₂ of an IROS depends on temperature to a noticeable extent. The last term in the right side of Eq. (2.27) usually cannot be eliminated. In order to assure an accurate measurement, the thermocouple measuring the cell temperature must be placed as close to the IRE as possible. In an IROS the reference pO₂ is determined by the equilibrium of the binary mixture of M/MO$_x$ (M: metal, MO$_x$: metal oxide):

$$MO_x = M + \frac{x}{2}O_2 \tag{2.28}$$

The dependence of the reference pO₂ on temperature can be obtained as:

$$\frac{dV_{cell}}{dT} = \frac{dE^0}{dT} - \frac{R}{4F}\ln p_S \tag{2.29}$$

where E^0 is the equilibrium potential of the binary mixture M/MO$_x$ versus the sensing electrode, SE, with p$_S$=1 bar. As seen from Eq. (2.29) the temperature dependence of the cell voltage, $\frac{dV_{cell}}{dT}$, is determined by the binary mixture serving as the internal reference electrode, indicated by $\frac{dE^0}{dT}$, and the pO₂ at the sensing electrode, p$_S$.

Provided the pO_2 at the sensing electrode, p_S, is 0.21 bar, a temperature fluctuation of 2.5 K will cause a fluctuation of 1 mV in the cell voltage for an IROS based on Ni/NiO[1], which will give a relative error of 5 % in a pO_2 measurement, as read from Figure 2.12. A small temperature dependence of cell voltage means that a cell is more resistant to a temperature disturbance and is thus desired in practice. Figure 2.12 shows the equilibrium potential versus SE (p_S= 1 bar) of ten binary mixtures in a temperature range of 200 - 800 ºC with the slopes,

$\dfrac{dE^0}{dT}$, given in the caption. All the investigated binary mixtures show a linear dependence of the equilibrium

potential on temperature. The slopes, $\dfrac{dE^0}{dT}$, are in a range of 0.30 - 0.55 mV· K^{-1}. Among the investigated binary

mixtures, Fe/FeO has the least temperature dependence, i.e., 0.33 mV· K^{-1}.
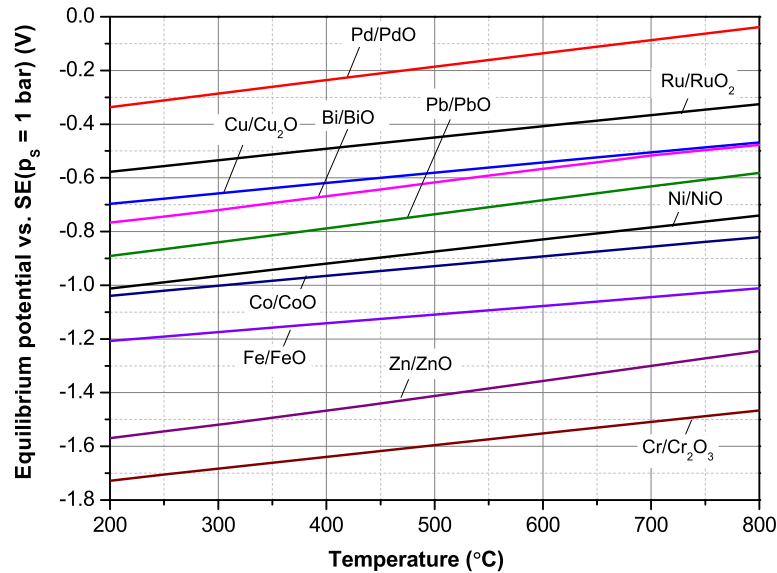
Figure 2.13. Equilibrium potentials of binary mixtures versus SE (p_S =1 bar). The slopes, in a unit of mV· K^{-1}, are: 0.50±0.01 (Pd/PdO), 0.42±0.01 (Ru/RuO$_2$), 0.38±0.01 (Cu/Cu$_2$O), 0.49±0.01 (Bi/Bi$_2$O$_3$), 0.52±0.01 (Pb/PbO), 0.46±0.01 (Ni/NiO), 0.36±0.01 (Co/CoO), 0.33±0.02 (Fe/FeO), 0.54±0.02 (Zn/ZnO), 0.44±0.01 (Cr/Cr$_2$O$_3$). The data are provided by FactSage^{TM} 5.5.

---

[1] Linearly fitting the thermodynamic data provided by FactSage^{TM} 5.5, the equilibrium potential of Ni/NiO versus SE (p_S =1 1bar) can be calculated in a temperature range of 20 – 800 ºC by:

$$E^0 = (0.458 \pm 0.004)T - (1230 \pm 2), \, vs.SE(p_S = 1bar)$$

where the equilibrium potential, E^0, is in a unit of mV and T is the thermodynamic temperature.

2.4 Conclusion

Oxides serving as the electrolyte of an IROS usually have an electronic conduction that will cause a leak current. The leak current density of an electrolyte made from 8YSZ can be estimated from the diffusion flux of holes. The electronic conduction of an electrolyte can be minimized to make the depletion period satisfy the target application up to duration of years.

The gas flow rate has a significant influence on the rate of gas mixing and therefore on the response time of a cell setup. The variations in oxygen fraction during a cycling of oxygen fraction are symmetrical, and the rate of gas mixing is independent of the change direction of oxygen fraction.

During a cycling of oxygen fraction, variations in cell voltage show asymmetry. When oxygen fraction is changed from low to high the initial variation rate of cell voltage is larger than that in the inverse change. The variation in cell temperature during gas mixing shows slight dependence on temperature.

Voltage errors have a substantial influence on the errors in pO_2 measurements. The voltage errors depend on the pO_2 at the sensing electrode and the composition of the binary mixture used to provide the reference pO_2. Ten binary mixtures are investigated and the dependences of the equilibrium potentials versus SE (p_S =1 bar) on temperature are in a range of 0.30 - 0.55 mV· K^{-1} and the binary mixture of Fe/FeO has the smallest temperature dependence of 0.33 mV· K^{-1}.

Appendix: The numerical simulation of gas mixing

The concentration of gas species k, c_k, is equal to $\dfrac{p_k}{RT}$ where p_K is the partial pressure of gas species k. During gas mixing the variation in the partial pressure of gas species k can be obtained by making a mass balance:

$$\frac{\partial}{\partial t}(\frac{p_k}{RT}) = -\nabla \cdot N_k \qquad\qquad (A2.1)$$

where N_k is the total mass flux in molar of gas species k, R is the gas constant and T is the thermodynamic temperature.

The total mass flux of species k, N_k, is the sum of the diffusion flux, N_k^D, and the viscous flux, N_k^V [11, 16, 17]:

$$N_k = N_k^D + N_k^V \qquad (A2.2)$$

In the framework of DGM the diffusion fluxes of individual component couple with each other [12-16]:

$$\nabla(\frac{p_k}{RT}) = \sum_{\substack{j=1 \\ j \neq k}}^{n} \frac{N_j^D p_k - N_k^D p_j}{D_{jk} P} - \frac{N_k^D}{D_k^K}, \quad k = 1,...,n \qquad (A2.3)$$

where D_k^K is the Knudsen diffusion coefficient of gas species k, P is the total pressure and D_{jk} is the binary diffusivity of gas species j and k [18]. The viscous flux of gas species k, N_k^V, is also referred to as the convection flux [17] and can be determined by the well-known Hagen-Poiseuille equation [11, 16]:

$$N_k^V = \frac{p_k}{RT} u_G \qquad (A2.4)$$

u_G is the convection velocity of the gas mixture and is determined by:

$$u_G = -\frac{d^2}{32\mu} \nabla P \qquad (A2.5)$$

where μ is the viscosity of the gas mixture [11], and d is the diameter of the tube in which the gas mixture flows.

Applying the above procedures to all gas species, the variations in all partial pressures can be expressed as:

$$\frac{1}{RT} \cdot \frac{\partial \overline{p}}{\partial t} = -\nabla \cdot \overline{N} \qquad (A2.6)$$

where both $\overline{p}$ and $\overline{N}$ are vectors, $\overline{p} = [p_1, p_2,..., p_n]^T$ and $\overline{N} = [N_1, N_2,..., N_n]^T$.

According to Eq. (A2.2) to (A2.4), and in the light of

$$\sum_{\substack{j=1 \\ j \neq k}}^{n} \frac{N_j^V p_k - N_k^V p_j}{PD_{jk}} = 0 \qquad (A2.7)$$

the vector of total fluxes can be written in the matrix form as:

$$M \cdot \overline{N} = B \qquad (A2.8)$$

The element of the matrix M, m_{ij}, is:

31

$$m_{ii} = \frac{1}{D_i^K} + \sum_{\substack{j=1 \\ j \neq i}}^{n} \frac{p_j}{PD_{ij}} \qquad (A2.9)$$

$$m_{ij} = -\frac{p_j}{PD_{ij}} \, (j \neq i) \qquad (A2.10)$$

and the element in the vector B, b_i, is:

$$b_i = -\frac{1}{RT} \cdot \nabla p_i - \frac{d^2 \cdot \nabla P}{32RT\mu} \cdot \frac{p_i}{D_i^K} \qquad (A2.11)$$

The initial condition is:

$$t=0, \ \overline{p} = \overline{p}^0 \qquad (A2.12)$$

The boundary conditions are:

$$t>0, \ \overline{p}(z=0) = \overline{p}_{in} \qquad (A2.13)$$

$$t>0, \ \nabla \cdot \overline{N}(z=\infty) = 0 \qquad (A2.14)$$

where $\overline{p}^0$ is the initial distributions of all partial pressures along the tube, $\overline{p}_{in}$ is the new partial pressures at the inlet when the gas composition is changed. Eq. (A2.14) is the boundary condition at the outlet and indicates that at a sufficiently/infinitely long distance the pO_2 changes at the inlet are not conveyed to the outlet. [19].

Due to the coupled individual diffusion fluxes, as shown by Eq. (A2.3), the analytic solution for above equations is not available so far [17]. The numerical solution is therefore developed in this study. The simulations are one dimensional and are carried out for the binary system of nitrogen and oxygen. The simulation length is 100 cm and the figures, i.e., Figure 2.8 - 2.11, show the pO_2/cell voltage variations at a position 2 cm from the inlet when the pO_2 at the inlet is changed. In simulations the total pressure at the inlet is set to 101350 Pa, 25 Pa higher than the atmospheric pressure. The inlet flow rate of nitrogen is 4 slph (standard liters per hour) and the inlet flow rate of oxygen changes between 0.1 and 1 slph, corresponding to a change in oxygen fraction between 0.024 and 0.2. These conditions will be met in the experiments presented in chapter 4.

The finite volume method [20] is used to discretize the calculation domain and the Crank-Nicolson method [21] is used to deal with the time dependent variables such as fluxes and partial pressures. Figure A2.1 presents the distribution of oxygen fraction along the simulation length, 50 seconds after the pO_2 change at the inlet. The gas flow rate is 8.9 mm·s^{-1}. One can see that the effect of the pO_2 change at the inlet is just conveyed to the position of 70 cm and the oxygen fraction at the outlet is unchanged. As seen from Figure 2.8, after 20 seconds the gas

mixing at z=2 cm has (almost) finished. So the boundary condition at the outlet will not influence the calculation at the sample position of 2 cm, i.e., the validity of the boundary condition of Eq. (A2.14) is satisfied in the simulation and the present results of Figure 2.8 are reliable. Similarly, the validity of the boundary condition of Eq. (A2.14) is satisfied in the simulation of the results shown in Figure 2.9.
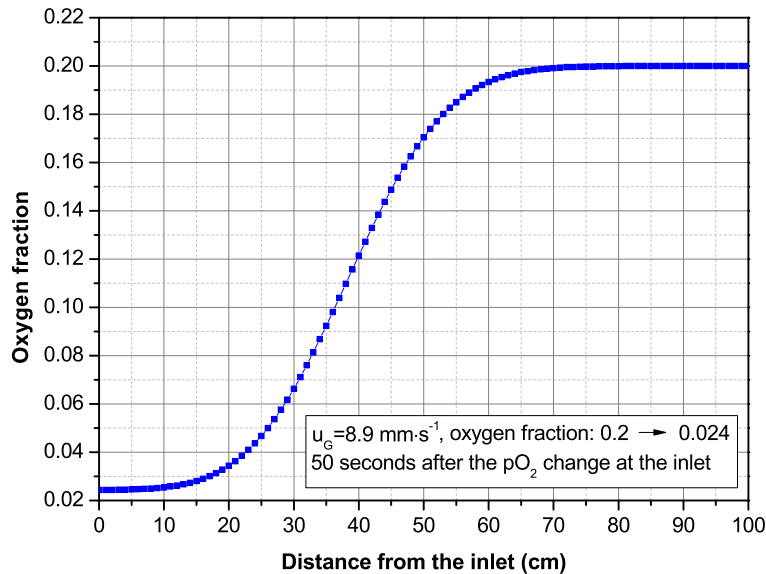
Figure A2.1. Distribution of oxygen fraction along the simulation length, 50 seconds after the pO_2 change at the inlet. The gas flow rate is 8.9 mm·s^{-1}. The effect of the pO_2 change at the inlet just reaches at the position of 70 cm.

References

1. J. H. Park and R. N. Blumenthal, Electronic Transport in 8 Mole Percent Y_2O_3-ZrO_2, J. Electrochem. Soc., 136(1989) 2867-2876.
2. H. Schmalzried, W. Laqua, and P. L. Lin, Crystalline oxide solid solutions in oxygen potential gradients, Z. Naturforsch., 34a(1979) 192-199.
3. M. Martin, Electrotransport and demixing in oxides, Solid State Ionics, 136-137(2000) 331-337.
4. T. Jacobsen and M. Mogensen, The course of oxygen partial pressure and electric potentials across an oxide electrolyte cell, ECS Trans., 13(2008) 259-273.

5. W. C. Maskell and B. C. H. Steele, Solid state potentiometric oxygen gas sensors, J. Appl. Electrochem., 16(1986) 475-489.

6. P. Atkins and J. de Paula, Atkins's physical chemistry, 7th Ed., Oxford university press, Oxford, 2002.

7. M. Mogensen, N. M. Sammes and G. A. Tompsett, Physical, chemical and electrochemical properties of pure and doped ceria, Solid state ionics, 129(2000) 63-94.

8. H. Näfe, Current-Voltage Relation and Charge Distribution in Mixed Ionic-Electronic Solid Conductors, J. Electrochem. Soc., 144(1997) 3922-3929.

9. H. Näfe, Solid electrolyte galvanic cell under load, J. Appl. Electrochem., 31(2001) 1235-1241.

10. Q. Hu, T. Jacobsen, K. V. Hansen and M. Mogensen, The depletion period due to an electronic conduction of the electrolyte of the internal reference oxygen sensor. Solid State Ionics (submitted).

11. R. B. Bird, W. E. Stewart and E. N. Lightfoot, Transport phenomena, 2nd, John Wiley & Sons, Inc., New York, 2002.

12. C. K. Ho and S. W. Webb, Gas transport in porous media, Springer, Dordrecht, 2006.

13. R. Suwanwarangkul, E. Croiset, M. W. Fowler, P. L. Douglas, E. Entchev and M.A. Douglas, Performance comparison of Fick's, dusty-gas and Stefan–Maxwell models to predict the concentration overpotential of a SOFC anode, J. Power Sources, 122(2003) 9-18.

14. R. Krishna and J.A. Wesselingh, The Maxwell-Stefan approach to mass transfer, Chem. Eng. Sci., 52(1997) 861-911.

15. E.A. Mason and A.P. Malinauskas, Gas transport in porous media: the dusty-gas model, Elsevier, New York, 1983.

16. R. E. Cunningham and R. J.J. Williams, Diffusion in gases and porous media, Plenum Press, New York, 1980.

17. L. Pisani, Multi-component gas mixture diffusion through porous media-A 1D analytical solution, Int. J. Heat Mass Transfer, 51(2008) 650-660.

18. E. N. Fuller, P. D. Schettler and J. Calvin Giddings, A new method for prediction of binary gas-phase diffusion coefficients, Ind. Eng. Chem., 58(1966) 18-27.

19. W. Shyy, Computational modeling for fluid flow and interfacial transport, Elsevier, Amsterdam, 1994.

20. S. V. Patankar, Numerical heat transfer and fluid flow, Hemisphere Pub. Corp., Washington, 1980.

21. J. W. Thomas, Numerical partial differential: finite difference methods, Springer, New York, 1995.

3 Cell fabrication

This chapter introduces step by step the procedures to fabricate an IROS with the underlying reasons given. Composite electrodes made from oxides are used in IROSes of this thesis and they are necessary to make an IROS be able to work recoverably and stably for a long term, i.e., more than 9 months. Parts of this chapter are included in a filed patent application, "Novel internal reference electrode and novel sensing electrode for an internal reference oxygen sensor, sensor employing same and use of the sensor", EP81909JHtra.

3.1 Advantages of composite electrodes and electrochemical reduction of NiO

The electrode processes within the sensing electrode (SE) can in general be expressed as:

$$O_2(g) + 2e^- \rightleftharpoons O^{2-} \qquad (3.1)$$

The electrode process needs a joint participation of oxygen molecules, electrons and oxide ions and therefore takes place at the triple phase boundary (TPB) [1]. Usually it is hard to find a material of single component that is versatilely active for oxygen molecule (dissociation), electron and oxide ion transport. For example, in the published IROSes Pt is the dominant electrode material. Though Pt has a good electron conductivity and a catalytic activity for oxygen molecule (dissociation) at a moderately high temperature such as 500 °C, it is only poorly surface conductive for oxide ions. The electrode process of Eq. (3.1) within a Pt based electrode is thus confined to a very narrow region close to the electrolyte that is normally a good oxide ion conductor such as yttria and/or scandia doped zirconia [2, 3], as illustrated by Figure 3.1.
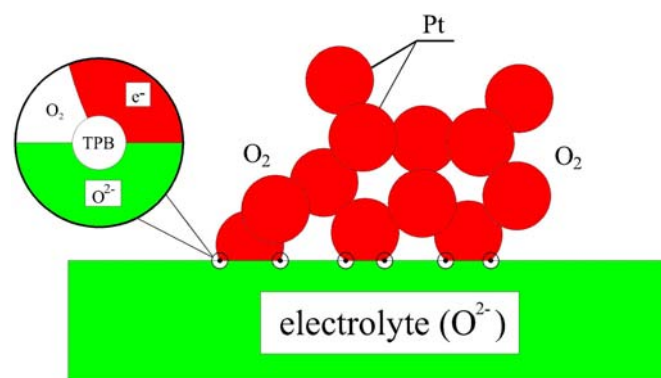

Figure 3.1. Illustration of the electrode of single component such as Pt. The TPB that is the site for the electrode process is confined to a narrow region close to the electrolyte.

Composite electrodes are widely used in solid oxide fuel cells and electrolyzes [4-8]. A composite electrode comprises at least two components and the individual component has a particular activity towards at least one of the three participants of the electrode process indicated by Eq. (3.1). Taking as an example the composite electrode consisting of $(La_{0.75}Sr_{0.25})_{0.95}MnO_{3\pm\delta}$ (LSM25) and 8 mol % yttria stabilized zirconia (8YSZ), 8YSZ is a well known oxide ion conductor [2, 3] and LSM25 has a good electronic conductivity [5, 9] and catalytic activity for oxygen molecule (dissociation). The TPB for the electrode process of Eq. (3.1) is thus significantly increased in the composite electrode. Correspondingly, the electrode is substantially activated that is desired by any electrochemical device including the IROS. The structure of a composite electrode consisting of two components is illustrated by Figure 3.2. In practice more than two components may be added to further improve the electrode performance [10].
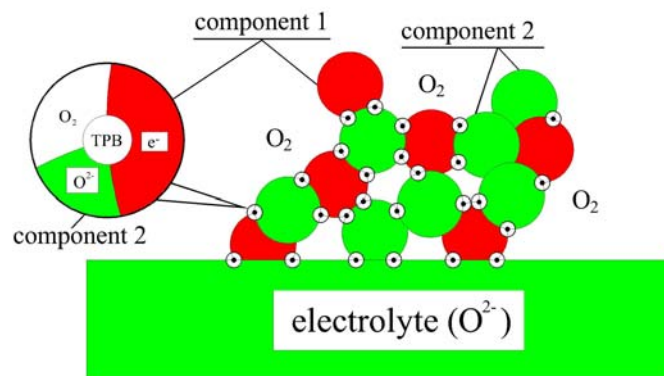

Figure 3.2. Illustration of a composite electrode with two components. The TPB is significantly extended to the entire electrode.

In the internal reference electrode (IRE) of an IROS, oxygen molecules do not necessarily exist. For example the equilibrium pO_2 of Ni/NiO is 5.6×10^{-18} bar at 663 °C, provided an electrode volume of 3.2×10^{-4} cm^3 (the typical IRE of the cells shown in later chapters has an area of 4x4 cm^2 and a thickness of 20 μm). The number of oxygen molecules within the electrode is thus equal to 0.01, meaning that no real oxygen molecule presents within the electrode. The general electrode process in the IRE may be expressed as:

$$MO_x + 2e^- \rightleftharpoons M + xO^{2-} \qquad (3.2)$$

As metal, M, is in general already a good electron conductor, a joint participation of metal oxide MO_x, metal and oxide ion is required for the electrode process indicated by Eq. (3.2), namely, an increased TPB is still desired to make the IRE active. However, so far the IRE of published IROSes consisted of a metal and its oxide only and the TPB were thus confined to the narrow region close to interface of electrolyte/electrode. Therefore the electrode activity is rather limited.

The prevailing method described in the literature to produce the IRE starts simply from mixing the powders of metal and its oxide. In 1995 van Setten et al. [11] generated *in situ* the binary mixture of Ni/NiO by electrochemical reducing NiO, which means that the fabrication of the IRE can start from the nickel oxide instead, and the inadvertent oxidation of Ni during cell fabrication, i.e., electrode sintering and sealing, is thus avoided. However the IRE of van Setten et al. [11] was still not composite, indicating that only the nickel oxide close the electrolyte could be reduced.

As reviewed in chapter 1 the binary mixtures of Ni/NiO and Pd/PdO are promising candidates for providing the reference pO_2. As cost is a key issue for practical applications, the binary mixture of Ni/NiO is selected in the present study and the binary mixture will be generated in the IRE by means of electrochemical reduction of NiO. The majority of cells presented later in this thesis will have composite sensing electrodes, but a few cells will be fabricated with a Pt sensing electrode in order to compare performance.

3.2 Sintering of the internal reference electrode

The IRE is made from a powder mixture of NiO (Alfa Aesar) and 8 mol % yttria stabilized zirconia (8YSZ) from Tosoh. Both powders contain a calcined part and an uncalcined part. Calcination of 8YSZ is performed at 1100 °C for 2 h and calcination of NiO is performed at 800 °C for 3 h. In the powder mixture, NiO, calcined NiO, 8YSZ and calcined 8YSZ powders, have a weight ratio of 3:3:2:2. Figure 3.3 shows the sintering curve of the powder mixture, measured by a thermodilatometer of NETZSCH DIL 402 C with a rate of 5 °C·min^{-1}. The sintering of the powder mixture is seen to be initiated from ca. 1100 °C. The powder mixture is then made into an ink with a terpineol based solvent. Figure 3.4 shows the TG-DTA curve of the ink, measured by a NETZSCH STA 409 CD with a rate of 5 °C·min^{-1}. The decomposition of the ink solvent is seen to take place from ca. 50 to 700 °C.
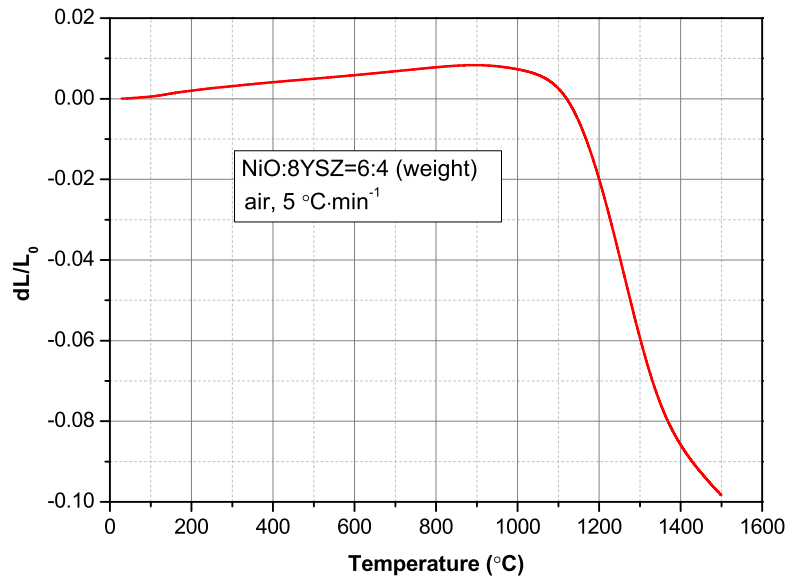
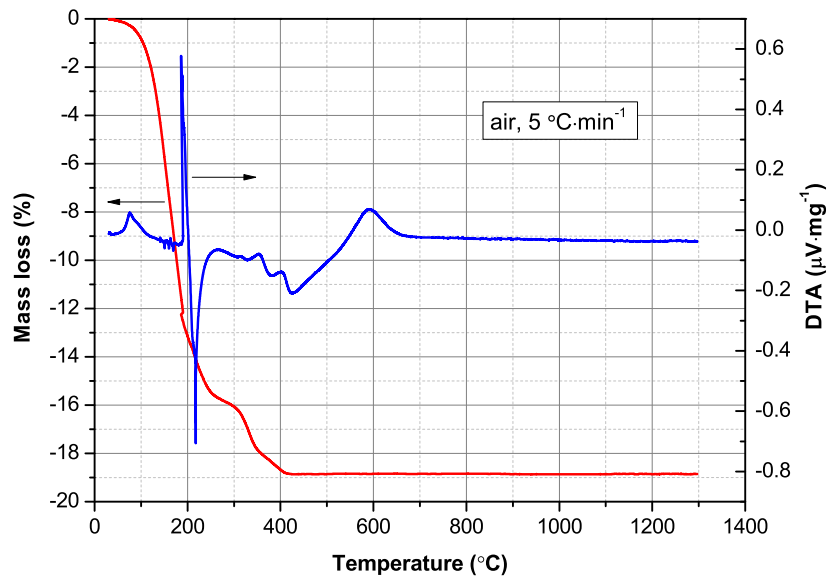Figure 3.3. Sintering of the powder mixture of NiO and 8YSZ with a weight ratio of 6:4.

Figure 3.4. TG-DTA measurement of the IRE slurry.

The ink is screen-printed on home-made tapes with a size of 10×10 or 5×10 mm^2. The tapes are made from 10 mol % Sc_2O_3 and 1 mol % Y_2O_3 stabilized zirconia (ScYSZ) from Daiichi or 8YSZ. After the screen printing, the tapes are sent for sintering. The temperature is increased slowly with a rate of 1 °C·min^{-1} to 700 °C and is held at 700 °C for 2 hours to facilitate the decomposition of the ink solvent. After that the temperature is increased with a relative larger rate of 2 °C·min^{-1} to 1350 °C and is held at 1350 °C for 2 h for sintering. After the sintering the temperature is decreased to room temperature at a rate of 2 °C·min^{-1}.

3.3 Sintering of the sensing electrode

After sintering the IRE, the tapes are screen printed by the sensing electrode ink on the opposite side. The sensing electrode ink is made from equal weight of $(La_{0.75}Sr_{0.25})_{0.95}MnO_{3\pm\delta}$ (LSM25) and 8YSZ, and is known to be sintered at 1050 °C. Graphite (Aldrich), used as pore former, is added into the ink with a weight ratio of 20 %. Figure 3.5 shows the TG-DTA curve of the graphite and the graphite is seen to burn out from ca. 600 °C. Figure 3.6 shows the TG-DTA curve of the sensing electrode ink with the addition of the graphite. The weight loss lasts until ca. 750 °C. After screen printing the sensing electrode ink, the tapes are heated to 800 °C with a rate of 1 °C·min^{-1} and the temperature is held at 800 °C for 2 h to remove completely the ink solvent and the graphite. Then the temperature is increased to 1050 °C with a rate of 2 ° C·min^{-1} and is held at 1050 °C for 2 h for sintering the sensing electrode. After the sintering, the temperature is decreased to room temperature with a rate of 2 °C·min^{-1}.

Pt is also used as the sensing electrode in some cells. The Pt electrode is s prepared by brushing Pt paste (FERRO) on the side opposite to the IRE, and then is sintered with an identical scheme of heat treatment.
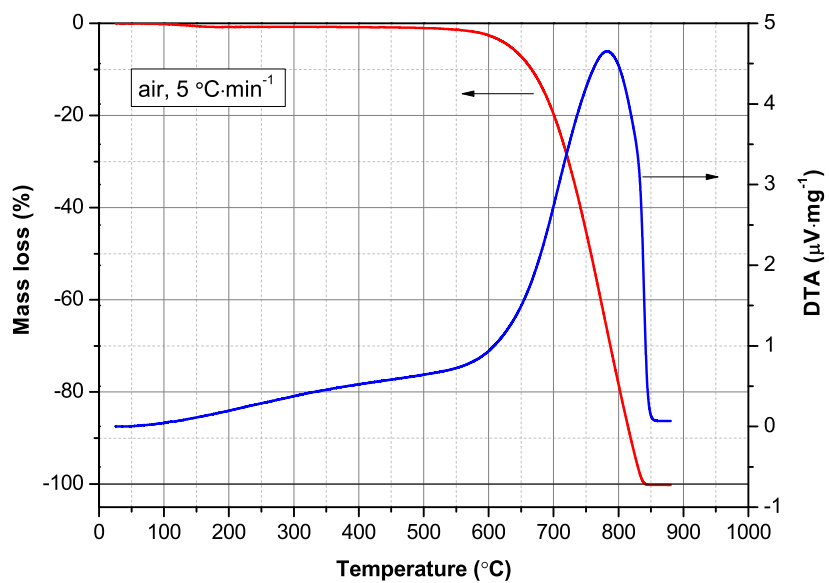
Figure 3.5. TG-DTA measurement of the graphite added to the sensing electrode ink.
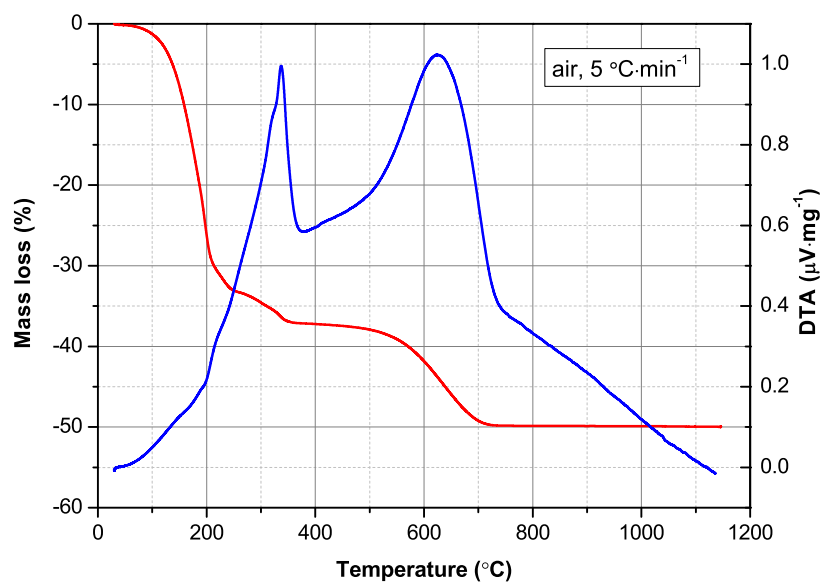

Figure 3.6. TG-DTA measurement of the sensing electrode ink with addition of the graphite.

3.4 Impregnation, coating and electrical connection of electrodes

Some IRE and/or SE are impregnated with 10 mol % Sm_2O_3 doped CeO_2, $Ce_{0.8}Sm_{0.2}O_{1.9}$ (SDC). The impregnation is performed by dripping a nitrate solution on the electrode surface and then decomposing the nitrate at 700 °C for 2 hours. The 1 M nitrate solution, $Ce_{0.8}Sm_{0.2}(NO_3)_x$, consisting of 20 mol % $Sm(NO_3)_3$ and 80 mol % $Ce(NO_3)_3$, is prepared from $Sm(NO_3)_3 \cdot 6H_2O$ (Alfa Aesar) and $Ce(NO_3)_3 \cdot 6H_2O$ (Alfa Aesar). Four times impregnation of SDC resulted in a load of ca. 6 mg·cm^{-2} for the IRE and ca. 3 mg·cm^{-2} for the SE. Figure 3.7 (a) shows the cross section of an IRE without SDC impregnation and (b) shows an IRE with SDC impregnation. Figure 3.8 (a) shows the cross section of an SE without SDC impregnation and (b) shows an SE with SDC impregnation. The SEM images were taken with a secondary electron detector and the acceleration voltage was 15 kV. Based on the calculation of CASINO v2.42 [12], the acceleration voltage of 15 kV will give a radius of the interaction volume of ca. 1 μm. As seen in Figure 3.7 the impregnated SDC particles, in a size of ca. 40 nano meters, cover the backbones of NiO and 8YSZ and penetrate to the interface of IRE/ScYSZ. As seen in Figure 3.8 (a) the sizes of the particles within the SE are less than 1 μm, the radius of the interaction volume. It is difficult to identify the individual particle composition and therefore the particle composition is not given. However, it can be seen in Figure 3.8 (b) that with the impregnation of SDC a large amount of fine particles that are in a size of ca. 40 nm and much smaller than those shown in Figure 3.8 (a) appear in the SE and cover the backbones of LSM25/8YSZ.
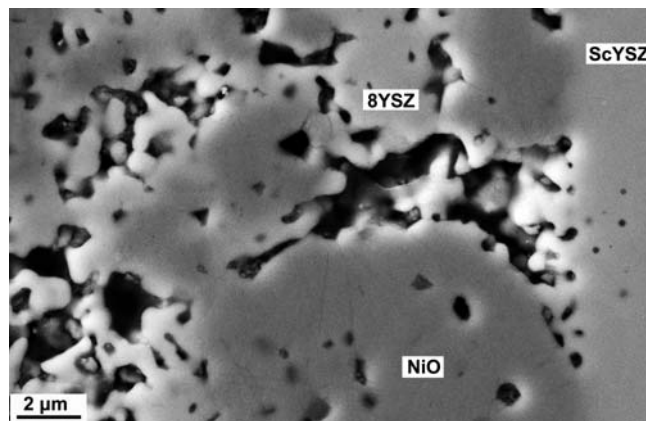
(a)
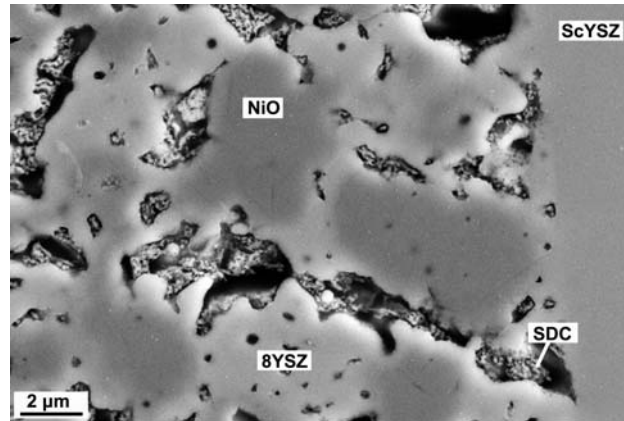
(b)

Figure 3.7. Cross section of (a) an IRE without SDC impregnation and (b) an IRE with SDC impregnation. The SEM images were taken with the secondary electron detector and the acceleration voltage was 15 kV. The impregnated SDC particles, in a size of ca. 40 nano meters, cover the backbones of NiO and 8YSZ and penetrate to the interface of IRE/ScYSZ.
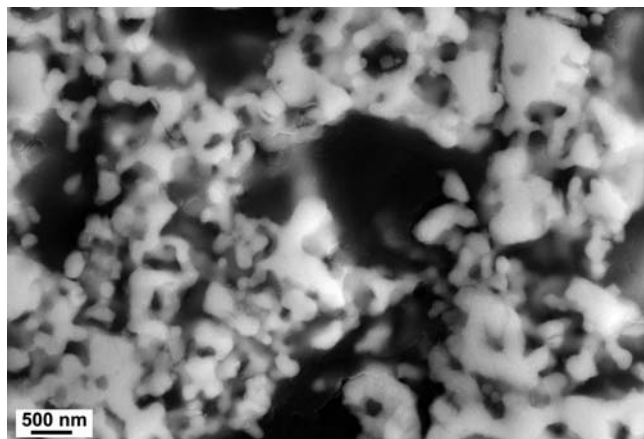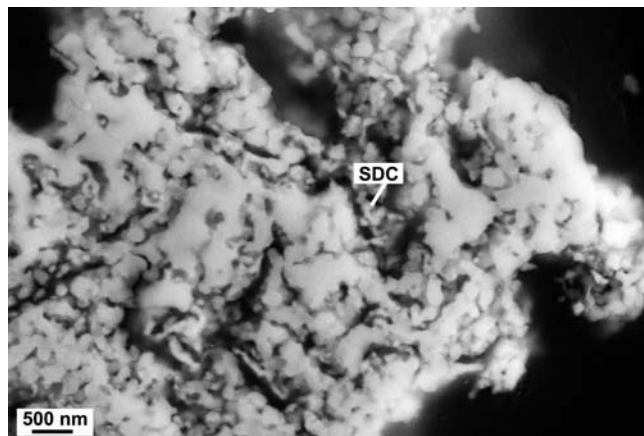

(a)

(b)

Figure 3.8. Cross sections of (a) an SE without SDC impregnation and (b) an SE with SDC impregnation. The SEM images were taken with the secondary electron detector and the acceleration voltage was 15 kV. The impregnated SDC particles, in a size of ca. 40 nano meters, cover the backbones of LSM25/8YSZ.

Some IREs have a gold coating that is applied by magnetron sputtering in argon under a pressure of 50 mTorr. The discharge voltage and current are 390 V and 400 mA, respectively, and the sputtering time is 1 hour.

After the preparation of IRE and SE, a Pt lead that is used for connecting the IRE with external circuits is adhered to the IRE by Pt paste, followed by a heat treatment at 700 °C for 1 hour. In some cells the Pt lead is replaced by an S-type thermocouple, by which the temperature of the IRE is able to be acquired. As known from Chapter 2 the IRE temperature is particularly important for an accurate pO_2 measurement.

3.5 Sealing of the IRE

After electrode preparation, SDC20 impregnation and electrical connection to the IRE, a glass seal is to be applied on the IRE. A glass, tagged as YS2B, is used to seal the IRE. The glass consists of SiO_2, 67.94 wt %, Al_2O_3, 14.91 wt %, Na_2O, 17.14 wt %. Figure 3.9 shows the equilibrium potentials versus pO_2=0.21 bar of Si/SiO_2, Al/Al_2O_3, Na/Na_2O, Zr/ZrO_2 and Ni/NiO in a temperature range between 500 and 800 °C. Note the equilibrium potentials of Zr/ZrO_2 and Al/Al_2O_3 are very close. The equilibrium potential of Ni/NiO is at least 600 mV above that of the rest. It is needed to be pointed out that the equilibrium potential of Zr/ZrO_2 is changed negligibly by a moderately doping of other oxides such as Y_2O_3. For example, at the temperatures of 900, 1000

43

and 1100 °C, the equilibrium potentials of Zr/ZrO$_2$ (versus pO$_2$=0.21 bar) where ZrO$_2$ is cubic by a doping of 10 mol % Y$_2$O$_3$ were measured to be -2.231, -2.178 and -2.126 V, respectively[13]. Based on the calculation of FactSage^{TM}5.5, the equilibrium potentials of Zr/ZrO$_2$ where ZrO$_2$ is monoclinic are -2.231, -2.180 and -2.129 V, respectively, for the corresponding temperatures. It is therefore reasonable to believe that with an appropriate potential applied on the IRE only NiO, rather than other oxides, i.e., the doped zirconia of the electrolyte and the glass constituting oxide, is reduced.

The glass powder is mixed with a polyethylenglycol based solution and is prepared to slurry. Figure 3.10 shows the TG-DTA measurement results of the glass slurry and the decomposition of the slurry solvent is seen to be finished until 500 °C. Three 8YSZ tapes, with a coating of the glass slurry, are heated at 760, 860 and 960 °C for 2 h, respectively, and their appearances are shown in Figure 3.11. At 760 °C, the glass starts to melt but cannot give a good wetness on the tape. At the temperature of 860 and 960 °C, the glass can wet completely the tape surface and the temperature 960 °C can give a somewhat better wetness of the tape. For the cells presented in this thesis sealing of the IRE is thus carried out at 960 °C. The influence of heat treatment scheme on the microstructure of the glass seal is investigated. Three glass samples were heated to 750 °C with a rate of 1 °C·min^{-1}, after a stay at 750 °C, these samples were heated to 960 °C with a rate of 2 °C·min^{-1} and stayed there for a while. After that the temperature was decrease with a rate of 2 °C·min^{-1}. The period in which the temperature was held at 750 and 960 °C, respectively, was varied and is listed in Table 3.1. The heat treatment scheme of sample 1 serves as the basis, and the temperature was held at 750 and 960 °C for 7 and 2 h, respectively.

Table 3.1. The stay periods at 750 and 960 °C, respectively, for the three samples.

Sample No.	Stay period at 750 °C (h)	Stay period at 960 °C (h)
1	7	2
2	1	2
3	7	7

The cross sections of the three samples are shown in Figure 3.12, and (a), (b) and (c) correspond to sample 1, 2 and 3 respectively. Bubbles are seen in all samples but they are not connected to each other, indicating that the seal is hermetic. Noticeably, the bubbles are distributed in a different way in the three samples. The bubbles distribution in sample 1 is relatively uniform and the maximum bubble size is around 100 μm. The heat

treatment scheme of sample 1 is therefore applied to the cells presented in this thesis. The bubble size varies significantly and excessively large bubbles are seen in sample 2 and 3. The largest bubbles in sample 2 and 3 can be in a size of 250 μm. The large bubbles will make the glass seal weak and make an IROS potentially fragile for the installation and operation, and should be avoided with the best possible. The bubbles are formed during the solvent decomposition and it is difficult for the bubbles to escape from the thoroughly melted glass due to the substantially increased viscosity. As known from Figure 3.10 and 3.11 the solvent decomposition lasts till 500 °C and the glass starts to melt at 760 °C, a long term such as 7 h stay at 750 °C is helpful for the bubbles to escape from the seal before the glass get completely melted. In the heat treatment scheme of sample 2, the stay period of 750 °C is reduced from the 7 h to 1 hr, which causes more bubbles rest in the glass, and the bubbles thereafter in the melted glass coalesce to large bubbles. In the heat treatment scheme of sample 3, the stay period at 750 °C is equal to that of sample 1 but the stay period of 960 °C is extended from 2 to 7 h, which also results in bubble coalesce into large bubbles. Based on the analysis of ImageJ 1.46r [14], the area fraction covered by the bubbles against the area of the glass seal is 5, 10 and 18 % for sample 1, 2 and 3, respectively. As the procedures of sample 1 gives the least bubble fraction, it is chosen as the standard procedure to seal the internal reference electrode.
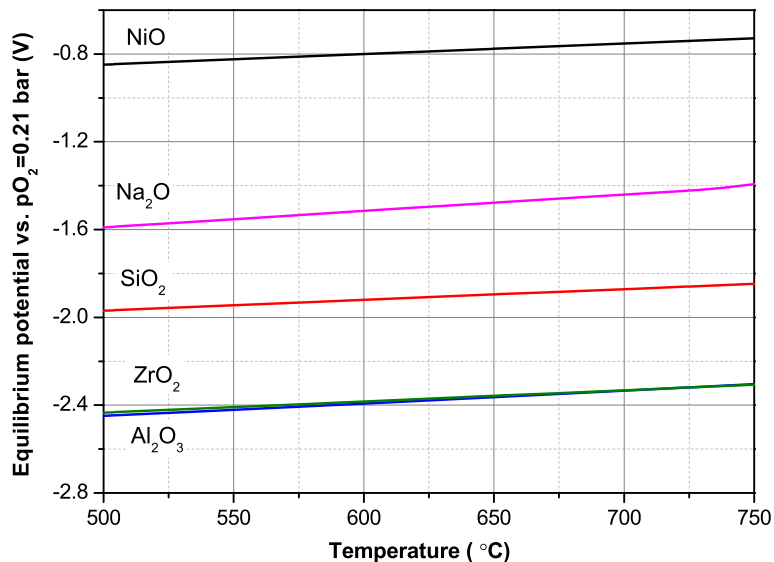
Figure 3.9. Equilibrium potentials versus pO_2=0.21 bar of Ni/NiO, Na/Na$_2$O, Si/SiO$_2$, Zr/ZrO$_2$ and Al/Al$_2$O$_3$ as functions of temperature. The data are obtained by FactSage^{TM} 5.5 [15]. Note the equilibrium potentials of Zr/ZrO$_2$ and Al/Al$_2$O$_3$ are very close.
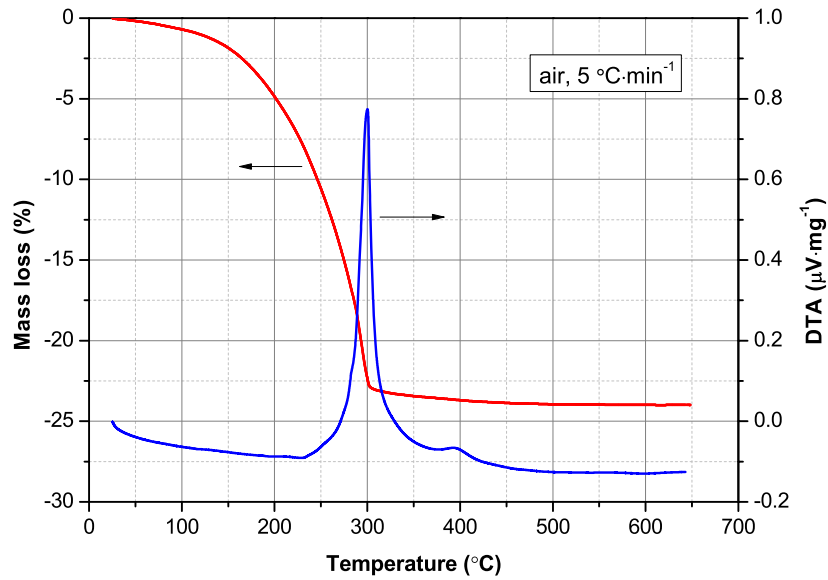
Figure 3.10. TG-DTA measurement of the glass slurry.
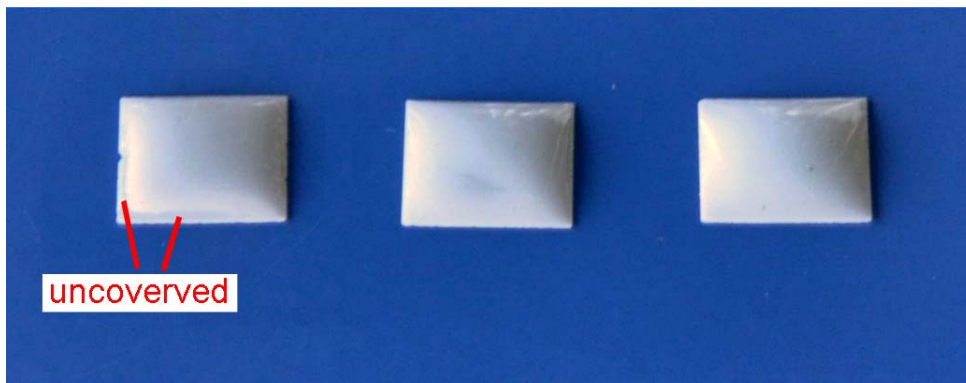
Figure 3.11. Glass coatings on 8YSZ tapes after sintering. From left to right the tapes with the glass coating are sintered at 760, 860 and 960 C, respectively, for 2 h. At 760 °C, the glass starts to melt but cannot give a good wetness on the tape. At the temperature of 860 and 960 °C, the glass can wet completely the tape surface and the temperature 960 °C can give a somewhat better wetness of the tape.
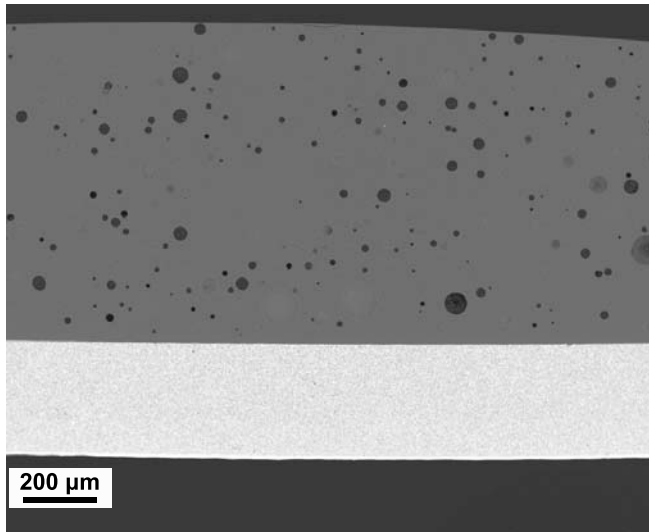
(a)
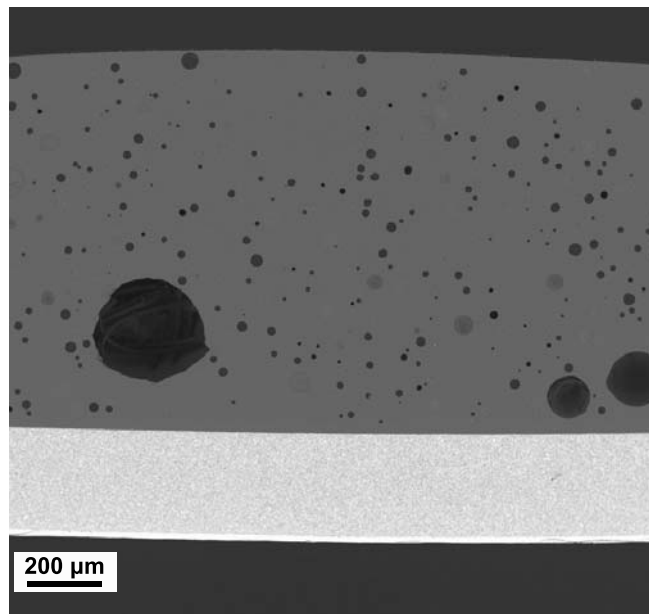
(b)
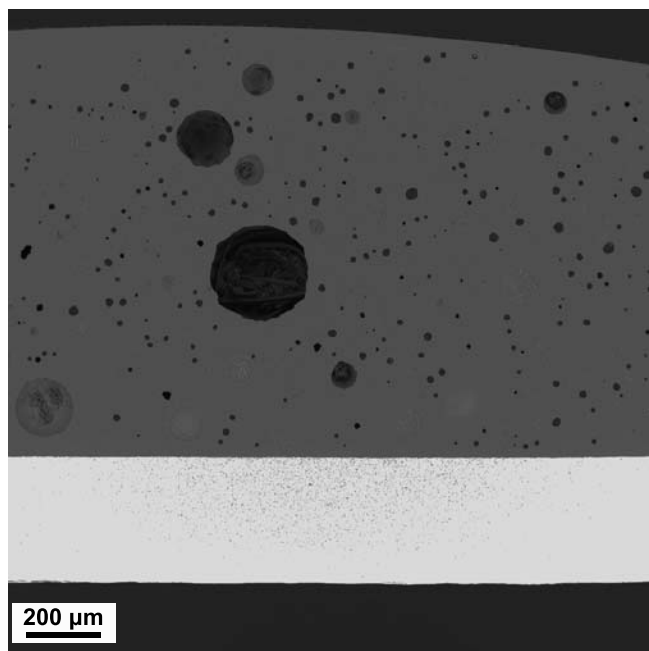
(c)

Figure 3.12. Cross section of glass seals with a varied heat treatment scheme. (a) sample 1, the temperature was held at 750 and 960 °C for 7 and 2 h, respectively. (b) sample 2, the temperature was held at 750 and 960 °C for 1 and 2 h, respectively. (c) sample 3, the temperature was held for 7 h at 750 and 960 °C, respectively.

3.6 Electrochemical reduction of NiO

After sealing the IRE, the IROS is as prepared. Figure 3.13 shows three IROSes based on composite sensing electrodes. The left two cells are fabricated with a size of 10×10 mm^2, and the right cell is fabricated in a smaller size of 5×10 mm^2 and has an integrated S-type thermocouple. Figure 3.14 shows the cross section of a cell with the cell components marked. The bubbles within the seal are distributed relatively uniformly. The contact between the Pt paste and the IRE is in that case not uniform and a portion of Pt paste has no access to the IRE.

To make an IROS functional the NiO within the IRE needs to be reduced partially to form *in situ* the binary mixture of Ni/NiO. The electrochemical reduction of NiO will be detailed in Chapter 5.
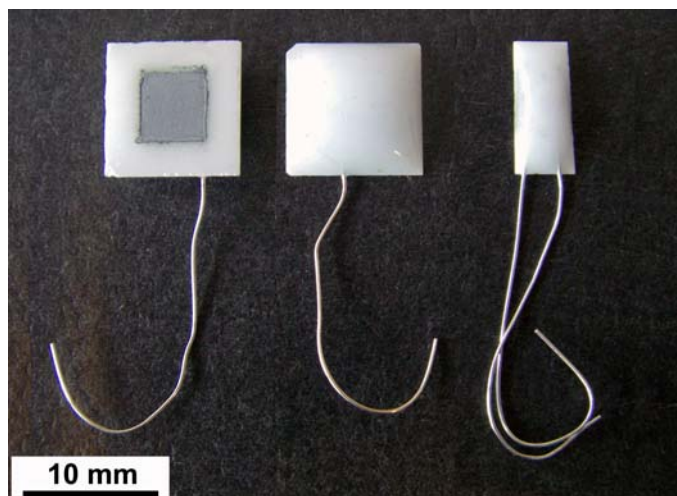
Figure 3.13. Three as-prepared IROSes based on composite sensing electrode. The left two cells are fabricated with a size of 10×10 mm^2, and the right cell is fabricated in a smaller size of 5×10 mm^2 and integrates an S-type thermocouple.
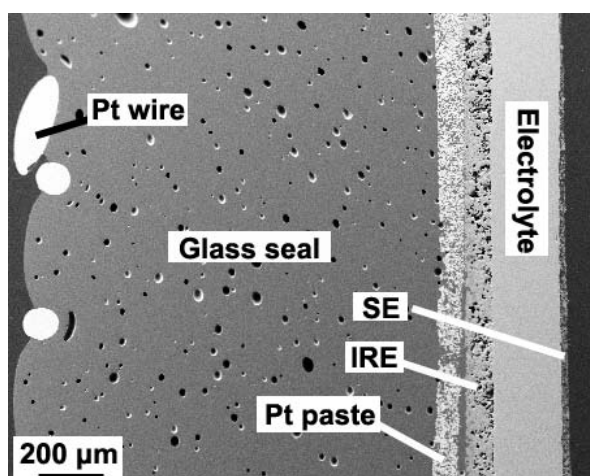
Figure 3.14. Cross section of an IROS and its components.

References

1. S. B. Adler, Factors governing oxygen reduction in solid oxide fuel cell cathodes, Chem. Rev., 104 (2004) 4791-4843.

2. A. Nakamura, J. B. Wagner, Jr., Defect structure, ionic conductivity, and diffusion in yttria stabilized zirconia and related oxide electrolytes with fluorite structure, J. Electrochem. Soc., 133(1986) 1542-1548.

3. V. V. Kharton, F. M. B. Marques and A. Atkinson, Transport properties of solid oxide electrolyte ceramics: a brief review, Solid State Ionics, 174(2004) 135-149.

4. S. M. Haile, Fuel cell materials and components, Acta Materialia 51(2003) 5981-6000.

5. S. P. Jiang, Development of lanthanum strontium manganite perovskite cathode materials of solid oxide fuel cells: a review, J. Mater. Sci., 43(2008) 6799-6833.

6. C. Sun, R. Hui and J. Roller, Cathode materials for solid oxide fuel cells: a review, J. Solid State Electrochem., 14(2010) 1125-1144.

7. A. Hauch, S. D. Ebbesen, S. H. Jensen, and M. Mogensen, Solid oxide electrolysis cells: Microstructure and Degradation of the Ni/Yttria-Stabilized Zirconia Electrode, J. Electrochem. Soc., 155(2008) B1184-B1193.

8. J. E. O'Brien, C. M. Stoots, J. S. Herring and J. Hartvigsen, Hydrogen Production Performance of a 10-Cell Planar Solid-Oxide Electrolysis Stack, J. Fuel Cell Sci. Technol., 3(2006) 213-219.

9. F. W. Poulsen, Defect chemistry modelling of Oxygen-stoichiometry, vacancy concentrations, and conductivity of $(La_{1-x}Sr_x)_yMnO_{3\pm\delta}$, Solid State Ionics, 129(2000) 145-162.

10. S. P. Jiang, A review of wet impregnation?An alternative method for the fabrication of high performance and nano-structured electrodes of solid oxide fuel cells, Mater. Sci. Eng. A, 418(2006) 199-210.

11. E. van Setten, T. M. Gür, D. H. A. Blank, J. C. Bravman and M. R. Beasley, Miniature Nernstian oxygen sensor for deposition and growth environments, Rev. Sci. Instrum., 73(2002) 156-161.

12. D. Drouin, A. R. Couture, R. Gauvin, P. Hovington, P. Horny, CASINO(v2.42), http://www.gel.usherb.ca/casino/.

13. W. Weppner, Formation of intermetallic Pt-Zr compounds between Pt electrodes and ZrO2 based electrolytes, and the decomposition voltage of yttria-doped ZrO_2, J. Electroanal. Chem., 84(1977) 339-350.

14. W. Rasband, ImagJ(v1.46r), http://imagej.nih.gov/ij/.

15. C. W. Bale, E. Bélisle, P. Chartrand, S. A. Decterov, G. Eriksson, K. Hack, I.-H. Jung, Y.-B. Kang, J. Melançon, A. D. Pelton, C. Robelin and S. Petersen, FactSage Thermochemical Software and Databases – Recent Developments, Calphad, 33(2009) 295-311.

4 Cell performance

This chapter presents an elaborate evaluation of IROS performance in terms of accuracy, stability, recoverability, response time and tolerances towards pO_2 cycling and thermal cycling. The cells used Pt or composite sensing electrode. The errors in cell voltage are less than 4 mV above 359 °C. The cells exhibit good stability (> 6600 h), extended working temperature range, good tolerance to thermal and pO_2 cycling, fast response and easy recoverability when Ni is depleted. The composite sensing electrode based on LSM25 and 8YSZ are proven superior over Pt to serve as the sensing electrode. Parts of this chapter are published in "Improved internal reference oxygen sensors with composite ceramic electrodes" J. Electrochem. Soc., 159(2012) B811-B817.

4.1 Experimental setups, devices and electrochemical test procedures

Two experimental setups were used to study cell performance and both setups comprised a rig and a tube. Figure 4.1 shows the smaller setup with an alumina rig inserted into a quartz tube. The setup was used to test response time and long term stability. The cell was usually placed 2 cm from the gas inlet. The quartz tube had an inner diameter of 25 mm and a length of 290 mm. The small setup had a slight leak and could only establish a pO_2 as low as 2×10^{-2} bar. Figure 4.2 shows the larger rig that was used to investigate response time, accuracy, recoverability and electrode processes, and was capable of testing four cells in one batch. During tests the rig was inserted into an alumina tube with an inner diameter of 69 mm and a length of 495 mm. This setup was able to maintain a pO_2 as low as 1×10^{-4} bar. The atmosphere in the setups was controlled by mass flow controllers (SLA5850, Brooks) and the source gas species included air, oxygen (N35, Air Liquid) and nitrogen (N48, Air Liquid). The pO_2 of the source nitrogen was 1.5×10^{-4} bar. The minimum and maximum flow rates of the mass flow controllers were 0.1 and 6 slph (standard liters per hour), respectively.
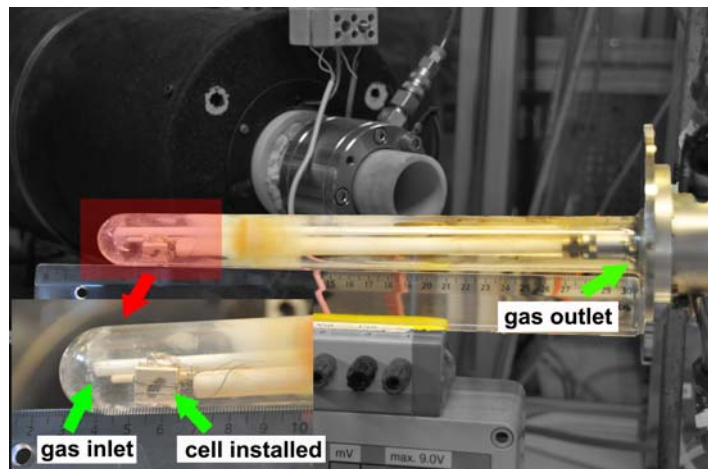
Figure 4.1. The small experimental setup with an alumina rig inserted into a quartz tube. The cell was usually placed 2 cm from the inlet.
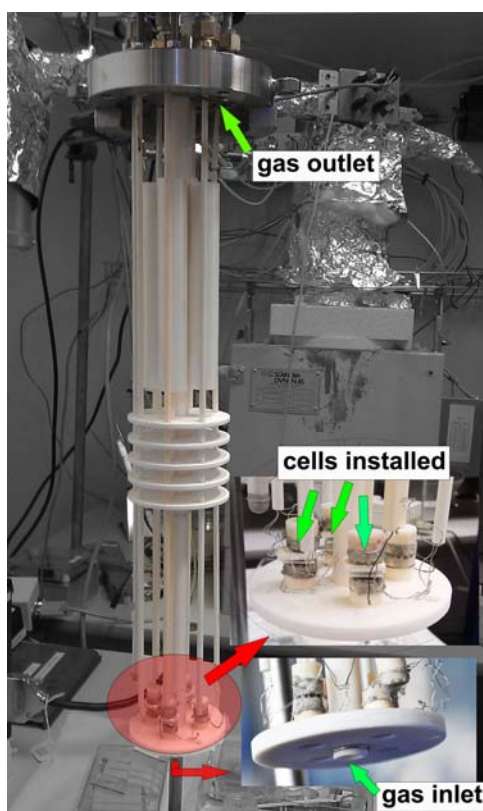

Figure 4.2. The large experiment rig that supports at most 4 cells to be tested in one batch.

Before an IROS becomes functional, the internal reference electrode (IRE) needs to be partially reduced to form the binary mixture of Ni/NiO. Voltage sweeps were performed on cells with an unreduced IRE in order to find an appropriate voltage to initiate NiO reduction. As the resistance of the sensing electrode (SE) was not negligible (see more details in Chapter 5), the voltage sweep could not be regarded as a potential sweep on the IRE. The IRE reduction and voltage sweep were carried out at 664 °C and in air. If nothing else is mentioned below, the IRE of a cell based on Pt sensing electrode was reduced at -1.1 V vs. SE (p_S=0.21 bar) and the IRE of a cell based on composite sensing electrodes (CSE) was reduced at -0.9 V vs. SE (p_S=0.21 bar). The reduction time was 65 minutes. Chronoamperometry was carried out during reduction and from the curve of current versus time the amount of reduced NiO was determined.

The microstructure and chemical composition of cells were investigated in a Zeiss Supra 35 field emission gun scanning electron microscope, equipped with a Noran System Six Model 3000 energy dispersive X-ray spectrometer, after sample polishing. The voltage sweeps, electrochemical impedance spectroscopy (EIS) and chronoamperometry were performed by a Solartron 1250 frequency response analyser along with a Solartron SI 1287 electrochemical interface. The electrochemical measurement software was Elchemea 5.1.3 that was developed in-house. In the accuracy tests, cell voltages were read by a Keithley 2700 multimeter and the stabilization period for a new test condition, i.e., pO_2 or temperature, was at least 2 h. The accuracy of Keithley 2700 in the voltage range of 1 V was ± (25 ppm of reading + 7 ppm of range). In the response time tests performed in the small setup the flow rate of nitrogen was kept at 4 slph while the flow rate of oxygen was switched between 0.1 and 1 slph. A Keithley KUSB-3108, with a much higher recording frequency ($\geq$ 1 Hz) and an accuracy of 0.01 % at a gain of 1, was used to record the change in cell voltage. In the response time tests carried out in the large setup the flow rate of nitrogen was switched between 6 and 0 slph while the flow rate of oxygen was switched between 0 and 6 slph at the same time. A Keithley 2700 was used to record the variation in cell voltage every 11 minutes. All the involved thermodynamic calculations such as the theoretical cell voltage are calculated by using FactSage[TM] 5.5.

4.2 Voltage sweeps

Voltage sweeps were performed on cells with an unreduced IRE in order to find an appropriate cell voltage to initiate NiO reduction. Figure 4.3 presents the first and the second sweeps on a cell with a structure of

IRE/ScYSZ/CSE. The voltage sweeps, with a rate of 5 mV·s⁻¹, were cyclically performed between 0 and -2.0 V four times, but only the sections between 0 to -1.15 V of the first and the second sweeps are presented for clarity, and the events taking place below -1.15 V had for this context only the effect of reducing more NiO, i.e., forming more and bigger Ni metal particles. The sweep curves became almost identical after the first sweep. A small peak occurred at ca. -100 mV during the first sweep but it did not reappear in the second sweep. After the small peak, the current density started to increase numerically below ca. -850 mV and the increase became significantly faster from ca. -1.0 V. After the first sweep, the IRE had an equilibrium potential of -767 mV vs. air, and an anodic current was obtained when the second sweep was initialized from 0 V. In the second sweep, the current changed from anodic to cathodic at -760 mV and then showed a significant increase, with a slope approximately equal to that in the first sweep when the IRE potential was below -1050 mV.
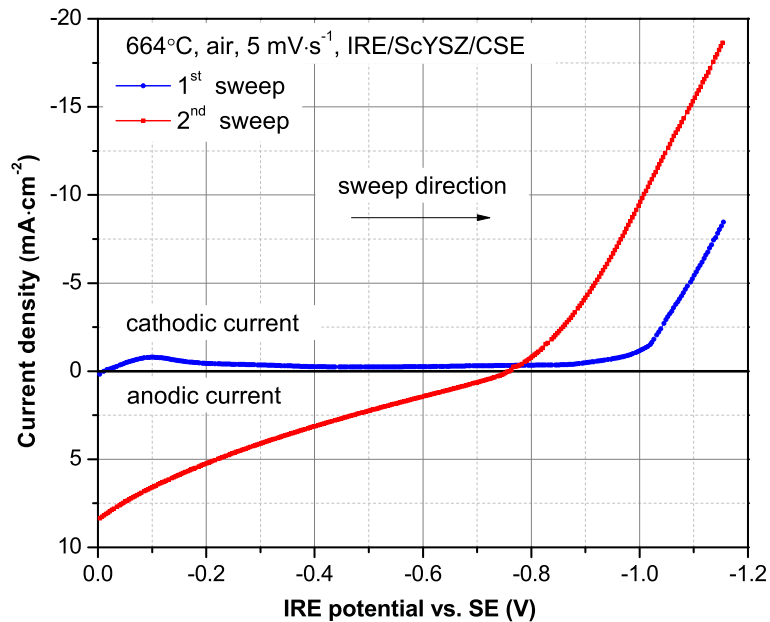
Figure 4.3. Voltage sweeps on an IROS with a structure of IRE/ScYSZ/CSE. Only the sections between 0 to -1.15 V of the first and the second sweeps are presented for clarity.

4.3 Response accuracy

Figure 4.4 shows the measured cell voltage, V_{cell}, of 5 cells with varied cell structures for three pO_2 levels, 1.64×10^{-2}, 0.21 and 1 bar, in a temperature range of 210 - 664 °C. The theoretical cell voltage, V_{theo}, is also given.

The '(SDC)' to the right of the electrode in cell structure notations means that the electrode had SDC impregnation. Above 450 °C the voltages of all cells agreed with the theoretical value well. Cell 1 that was based on a Pt sensing electrode had a larger voltage error. The voltage errors of cell 1 were ≤ 4 mV and ≤ 17 mV at 469 and 359 °C respectively. The voltage errors of other cells based on composite sensing electrodes were ≤ 2 mV and ≤ 4 mV at 469 ° and 359 °C respectively. The voltage error increased with decreasing temperature. At a low temperature of 263 °C, cell 5 that had both electrodes impregnated by SDC had the lowest voltage error of ≤ 16 mV among the five cells. (a) - (c) show that V_{cell} was significantly lower than V_{theo} at the temperatures below 260 °C. To ensure the measurement accuracy, 360 °C is the suggested lowest reliable operation temperature for cell 5 unless the cell voltage is calibrated against gases with well-known oxygen partial pressures. The cells with composite sensing electrodes show advantages over the one with Pt sensing electrode in the aspects of an extended working temperature range and smaller errors.
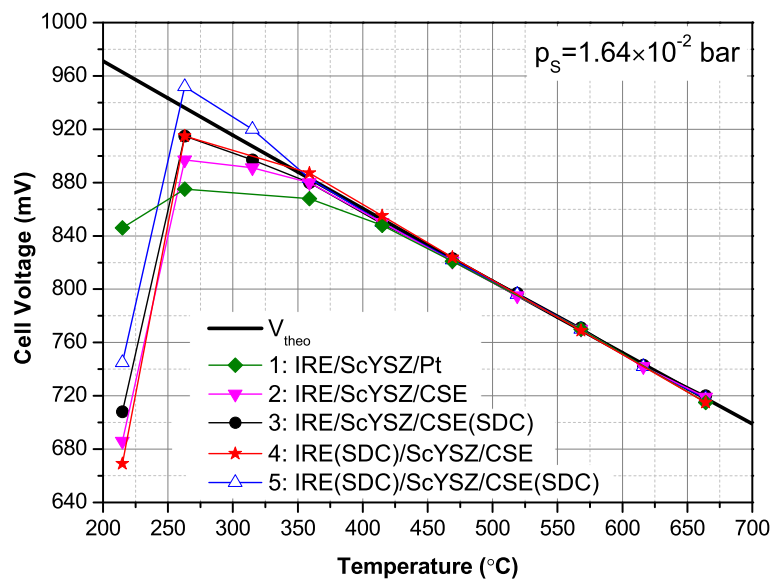
(a)
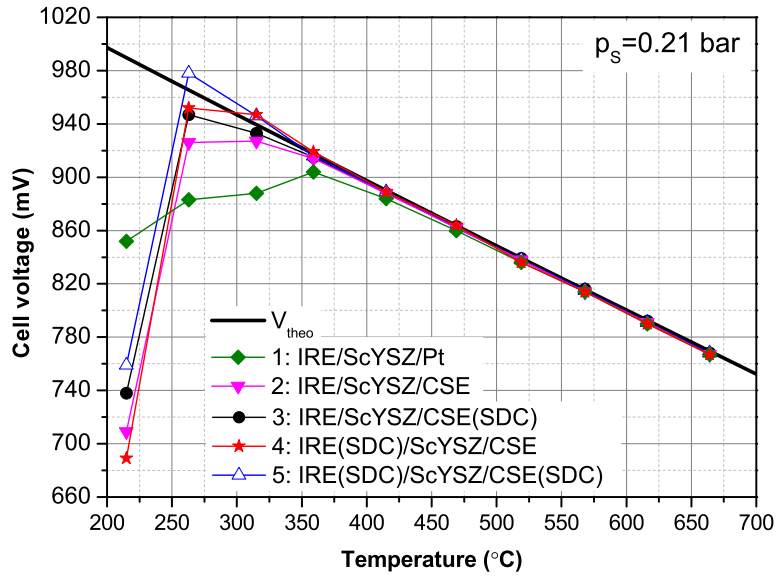
(b)
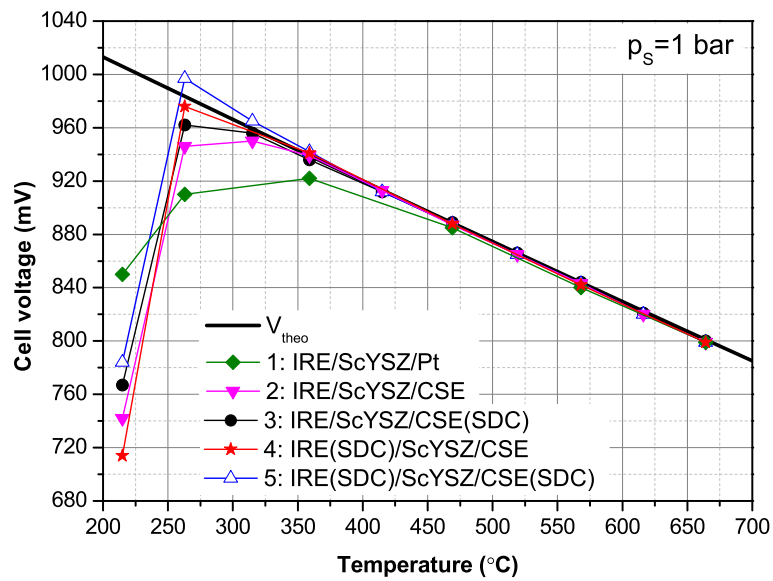
(c)

Figure 4.4. The measured cell voltage, V_{cell}, and the theoretical cell voltage, V_{theo}, at three pO_2 levels: (a) 1.64×10^{-2} bar, (b) 0.21 bar and (c) 1 bar. The composite sensing electrode shows advantages over Pt to serve as

56

the sensing electrode in terms of an extended working temperature range and a smaller error. Cell structures are given in the figure legends.

4.4 Response time

Figure 4.5 shows response time tests carried out in the small setup at four temperatures, i.e., 521, 568, 616 and 663 °C. During the tests the pO_2 inside the setup was cycled between 0.024 and 0.2 bar. The cell responded to the pO_2 variation quickly and it is found that: 1) the response time behaved asymmetrically, i.e., changing pO_2 from high to low took longer time than the inverse process. Upon changing pO_2 from 0.2 to 0.024 bar it took ca. 30 seconds at 663 °C to reach a stable cell voltage, whereas the cell voltage was stabilized within 15 seconds when the pO_2 was changed from 0.024 to 0.2 bar; 2) response time depended on temperature and a higher temperature resulted in a shorter response time. For example, when changing the pO_2 from 0.2 to 0.024 bar it took ca. 45 seconds at 521 °C to reach the stable voltage, whereas it took ca. 30 seconds at 663 °C. The measured cell voltages were a bit higher than the theoretical values, especially under the low pO_2 condition. As mentioned above, the small setup used for the response time tests had a small leak, and thus the relative errors at 0.024 bar in this setup were larger than at 0.2 bar. Dips in cell voltage are seen when pO_2 was changed back to 0.2 bar, which was possibly caused by the PID setting of the mass flow controllers. The dips were more pronounced at high temperatures such as 663 and 616 °C as the cell responded faster to a pO_2 variation at high temperature.
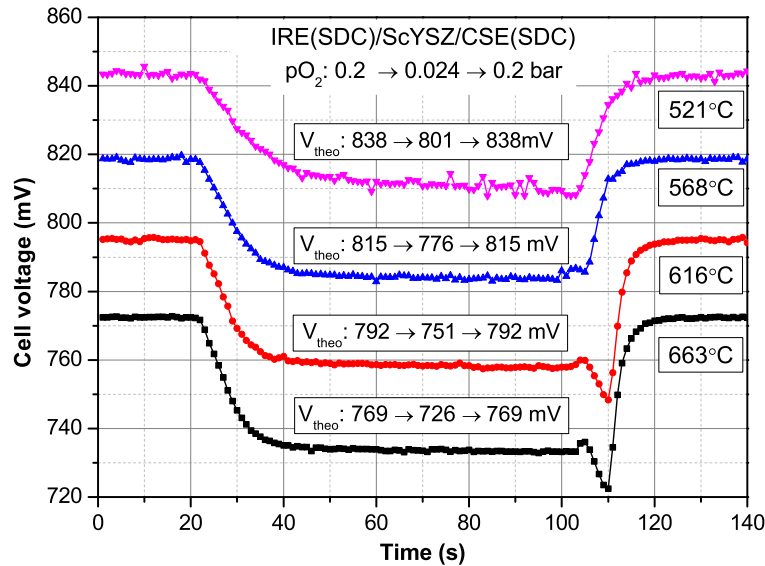
Figure 4.5. Cell voltage variation during pO_2 cycling between 0.2 and 0.024 bar in the small setup. Dips in cell voltage seen when pO_2 was changed back to 0.2 bar were possibly caused by the PID setting of the mass flow controllers. The response time observed in the small setup depended on temperature and the direction of pO_2 change.

Figure 4.6 shows response time tests carried out in the large setup at four temperatures, i.e., 359, 469, 568 and 663 °C. The pO_2 inside the large setup was cycled between that of air (pO_2= 0.21 bar) and nitrogen (pO_2= 1.5×10^{-4} bar). The response time behaved also asymmetrically. Changing pO_2 from low to high took a much shorter time but the response time showed little temperature dependent. The response time at a low temperature such as 359 °C was almost equal to that at a high temperature such as 663 °C. At an identical temperature of 663 °C the response time observed in the large setup was substantially prolonged from that observed in the small setup. The theoretical cell voltage at pO_2= 0.024 bar and 663 °C is 726 mV. For an almost identical pO_2 variation from 0.2 to 0.024 bar, the response time observed in the small and large setup were 30 seconds and 15 minutes, respectively. Figure 4.7 shows cell voltage variations of different cell structures when the atmosphere was changed from air to nitrogen in the large setup. The response time is seen to be little dependent of cell structures.
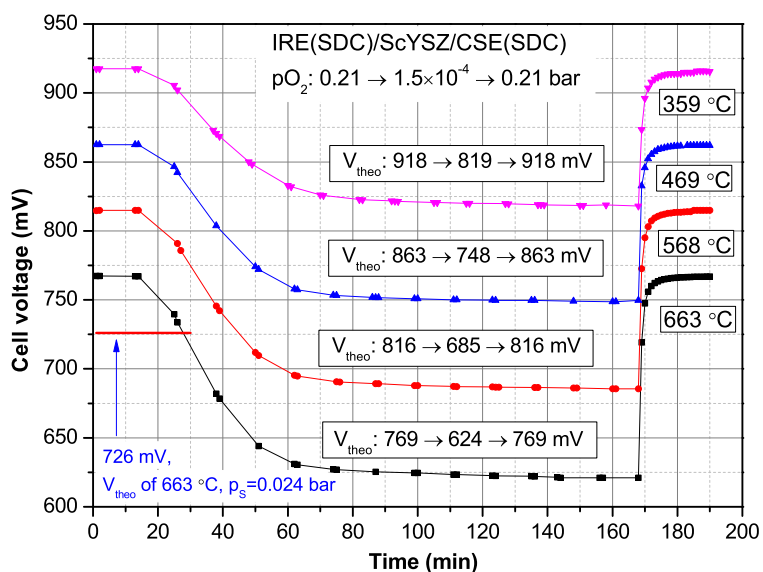
Figure 4.6. Cell voltage variation during pO_2 cycling between 0.21 and 1.5×10^{-4} bar in the large setup. The response time was independent of temperature but dependent on the direction of pO_2 change.
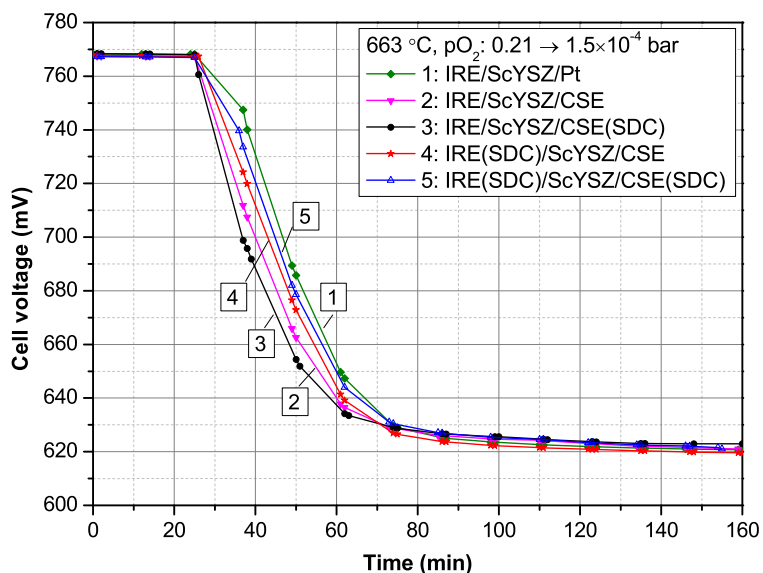
Figure 4.7. Cell voltage variation when pO_2 inside the large setup was changed from 0.21 (air) to 1.5×10^{-4} bar (N_2) in the large setup. The response time was little dependent on cell structures.

4.5 Stability, recoverability and thermal cycling

Figure 4.8 shows the cell voltages over time of two cells with different initial IRE reduction degree. Both cells had a structure of (Au)IRE/8YSZ/Pt and their IREs were reduced at -1.1 V. The '(Au)' to the left of the 'IRE' in the cell structure notation means that the IRE has an Au coating. One IRE (filled squares) had 67 % of NiO reduced while the other (filled circle) had 11 % of NiO reduced. The voltage of the former cell showed no voltage decrease after 90 h, whereas the voltage of the latter cell started to decrease after 15 h. However, with a recovery ("recharge") at -1.1 V for 3 h the voltage of the latter cell was restored, meaning that the cell voltage decrease due to Ni depletion was recoverable.
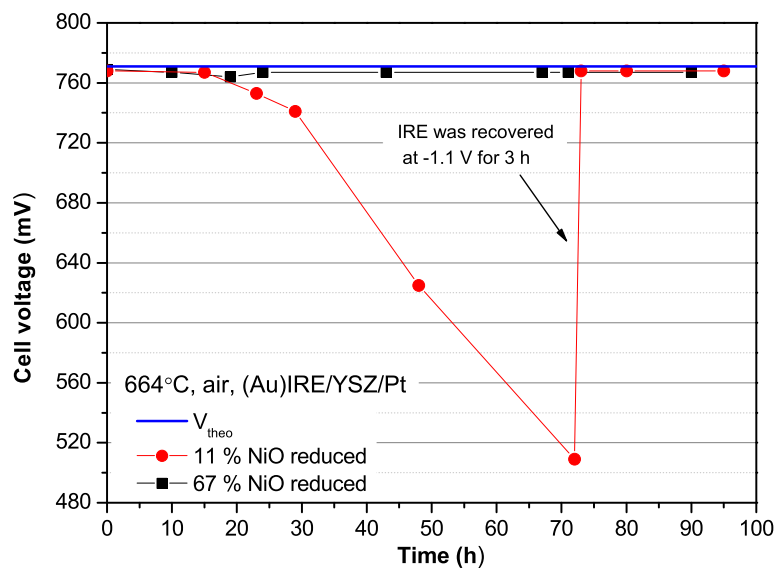
Figure 4.8. Effects of IRE reduction degree on the stability of cell voltage. Both cells had a structure of (Au)IRE/8YSZ/Pt. The stable cell had 67 % of NiO reduced. The cell with 11 % of NiO reduced had a voltage decrease after 15 h, but the cell voltage was recovered.

Figure 4.9 shows the stability test of a cell with structure IRE(SDC)/ScYSZ/CSE(SDC). The cell had both electrodes impregnated by SDC. The test included pO_2 cycling between 0.024 and 0.2 bar every 12 h and gave cell voltages at two levels. The IRE of the cell was reduced at -1.0 V for 50 minutes, corresponding to a reduction of 43 % of NiO, and had no any recovery operation during the test. Due to disturbances from

impedance spectroscopy and slight operation condition variations such as temperature fluctuations, minor fluctuations of a few mV in the cell voltage were seen. The cell voltage was stable in a period of about 6600 h (> 9 months). Since the setup had a small leak, the cell voltage at the low pO_2 level was slightly higher, ca. 4 mV, than the nominal. The noticeable cell voltage increase at ca. 6600 h was found to be related with a large drop in the atmospheric temperature. The gas cylinders were placed outdoor and at that time the atmospheric temperature had a sharp drop of ca. 15 °C. The cell voltage was subjected to a noticeable decrease after the cell voltage increase and the decrease in the cell voltage became faster from ca. 8000 h. The stability test was stopped at 8677 h and the furnace was cooled down with a rate of 2 °C·min^{-1}. Figure 4.10 presents the cell after the stability test. A crack was seen in the glass seal but it is unknown if the crack was formed during cell operation or during the process of cooling down.

Figure 4.11 (a) presents the cross sections of the IRE of the cell after the stability test and (b) presents an SDC impregnated IRE of an unreduced and untested cell. No evident change in microstructure was seen and the SDC particles that were in a size of tens of nano meters survived in the operation of 8677 h. Figure 4.12 shows the cross sections of (a) the SE of the cell after the stability test and (b) an SDC impregnated SE of an untested cell. No evident change in microstructure was seen. The acceleration voltage used in the SEM was 15 kV, which would give a radius of ca. 1 μm for the interaction volume, based on the calculation of CASINO v2.42 [1]. As the sizes of the particles of LSM25 and 8YSZ were close and smaller than the radius of the interaction volume, it is difficult to identify the individual particle composition. As the SDC particles had a much smaller size than LSM25/8YSZ (see Figure 3.8 in Chapter 3) they can be identified.
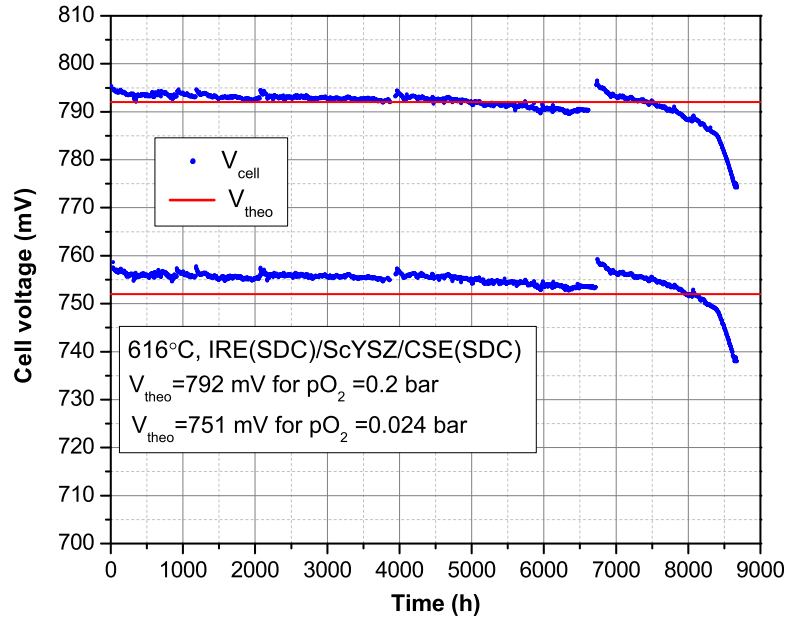
Figure 4.9. Stability test of a cell with structure IRE(SDC20)/ScYSZ/CSE(SDC20). The test included pO_2 cycling between 0.024 and 0.2 bar every 12 h. Due to a small leak of the test setup the cell voltage at the low pO_2 level was slightly higher, ca. 4 mV, than the theoretical. The stability test proceeded from 8677 h. The noticeable cell voltage increase at ca. 6600 h was found to be related with a sudden atmospheric temperature drop.
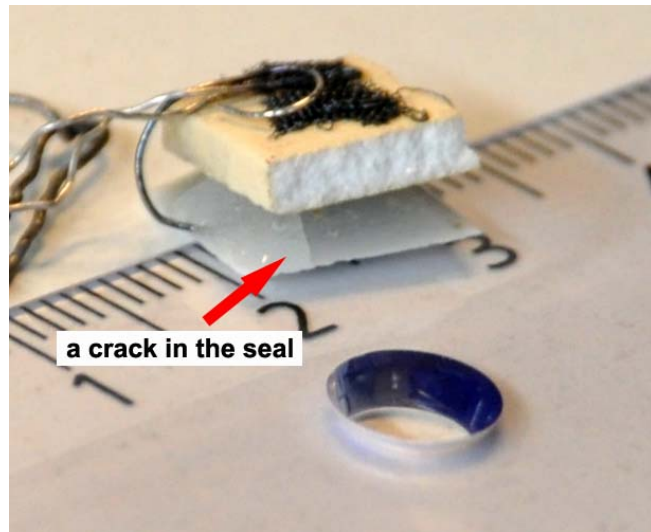
Figure 4.10. The cell after the stability test of 8766 h.
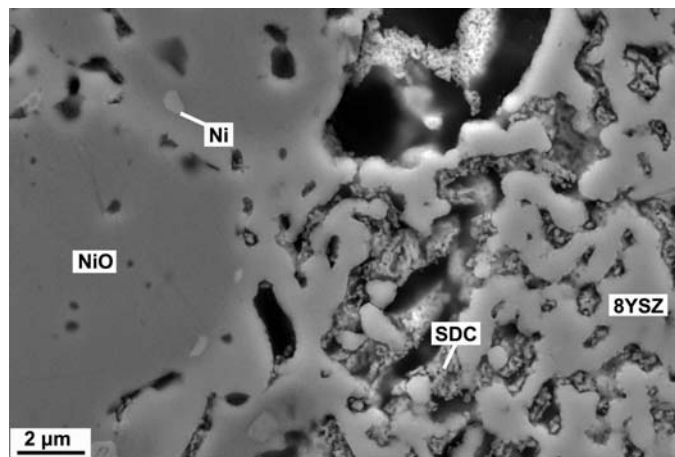
(a)
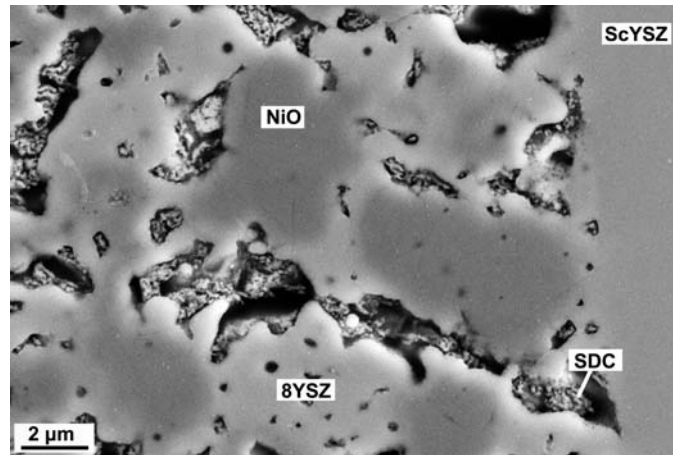
(b)

Figure 4.11. The cross sections of (a) the IRE of the cell after the stability test of 8677 h and (b) an SDC impregnated IRE of an unreduced and untested cell. The images were taken with a secondary electron detector and the acceleration voltage was 15 kV. No evident change in microstructure was seen and the nano sized SDC particles survived in the long term operation.
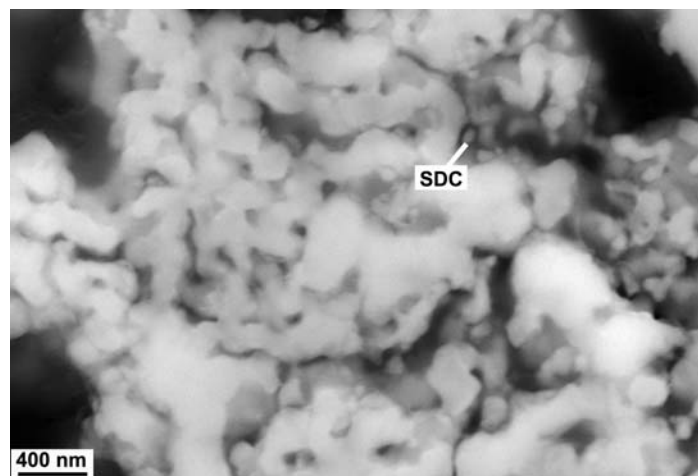
(a)
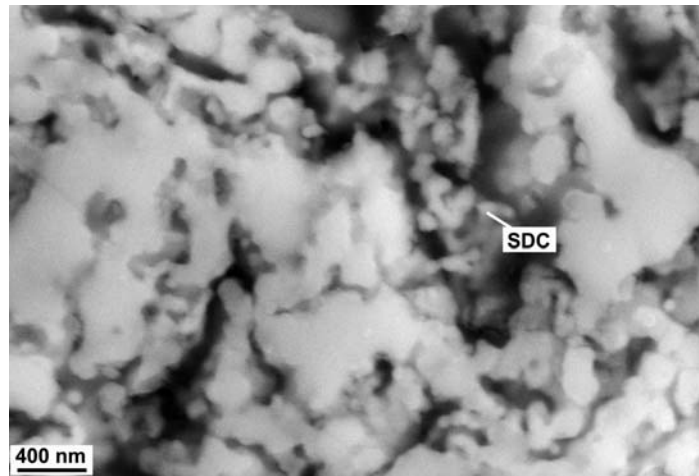
(b)

Figure 4.12. The cross sections of (a) the SE of the cell after the stability test and (b) an SDC impregnated SE of an untested cell. The images were taken with a secondary electron detector and the acceleration voltage was 15 kV. No evident change in microstructure was seen.

A thermal cycling between 684 and 25 °C was applied on a cell and Figure 4.9 shows the impedance spectra before and after the thermal cycling. The impedance spectrum varied slightly after the thermal cycling, and the cell voltage changed only 1 mV, indicating that the cell electrochemical properties were not significantly affected by the thermal cycling, and the thermal expansion match among cell components had been realized to a large extent.
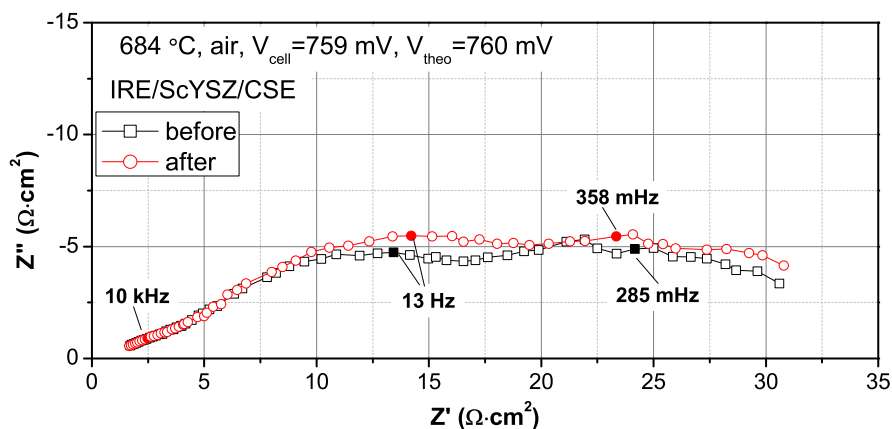
Figure 4.13. The impedance spectra and cell voltage before and after a thermal cycling between 684 and 25 °C. The cell structure was IRE/ScYSZ/CSE. Electrochemical properties of the cell were well maintained in the thermal cycling.

4.7 Discussions

The binary mixture of Ni/NiO was formed *in situ* by electrochemical reduction of NiO after electrode sintering and sealing, a method introduced by van Setten et al. [2] before. By this means the preparation of IRE can start from NiO instead of the mixture of Ni and NiO normally applied [3-5], and the inadvertent oxidation of Ni during cell fabrication is avoided. The IRE of the cell fabricated by van Setten et al. [2] consisted only of Ni and NiO. In the presented cells the IREs were composite and included a network of 8YSZ, as shown in Figure 4.11. The reduction of NiO is thus capable of taking place within whole electrode and is no longer confined to a rather narrow section of the interface of IRE/electrolyte.

The small peak at ca. -100 mV, occurring in the first sweep of Figure 4.3, corresponds to a removal of the residual oxygen sealed in the IRE. This process requires a relatively low polarization and the amount of residual oxygen was about 1.5×10^{-8} mol, known from the chronoamperometry. After the first sweep, the binary mixture of Ni/NiO had been formed, indicated by a stable open circuit voltage. This open circuit voltage, 767 mV is rather close to the theoretical value of 770 mV. As the residual oxygen sealed in the IRE had been depleted during the first sweep, the peak of oxygen removal did not reappear in the following sweeps. In cases that

66

oxygen was pumped into the IRE during a cyclic voltage sweep, it reacted by the already formed Ni particles into NiO.

In Figure 4.3 the potential from which the current density started to significantly increase is seen to numerically decrease from ca. -1.05 V in the first sweep to -0.85 V in the second sweep. When the sweep started from 0 V in the first sweep, Ni particles had not been formed. As the formation of Ni nuclei needs an extra polarization [6, 7], the significant increase in the current density took place at a more negative potential such as below -1.05 V. However, once the Ni nuclei were formed, the extra polarization was not required. Therefore in the second sweep the current density started to increase from a numerically smaller potential such as -0.85 V. The significant increase in the current density corresponds to the reduction of NiO. Due to the same kinetics both sweeps have an almost identical slope when the sweep potential was very negative, i.e., below -1.05 V.

Stability has been a challenge preventing the commercialization of IROSes and is influenced by several factors including leak of the seal, reactions and mismatching of thermal expansion among cell components [2, 5, 9]. The material systems such as the sealing glass and electrode materials of the cells show in this study are carefully selected to assure a general compatibility between cell components. Due to an improved electrochemical performance, the presented cells are able to work well even at a moderate temperature, i.e., < 500 °C, thus reducing reactions between cell components and prolonging the stable service period.

As known from Chapter 2, an error in cell voltage, ΔV, will cause an error, Δp_S, in pO$_2$ measurement for a potentiometric oxygen sensor and the relative error is given by:

$$\frac{\Delta p_S}{p_S} = \exp(\frac{4F}{RT}\Delta V) - 1 \tag{4.1}$$

A slight error of ±1 mV in cell voltage results in a relative error of ±5 % in pO$_2$ measurement at 663 °C. As shown in Figure 4.4(b), cell 5 that had both electrodes impregnated by SDC had a cell voltage error of -13 mV in air at 263 °C. The moderate errors such as 13 mV and -13 mV in cell voltage give relative errors of 208 % and -68 % at 263 °C, respectively. A small error in cell voltage measurement can cause a relatively large error in pO$_2$ measurement as the voltage error takes a position at the exponent in Eq. (4.1). In order to get very precise pO$_2$ measurements calibration with certified gases are necessary. The voltage errors of the cells based on composite sensing electrodes were less than 4 mV above 359 °C. The errors in cell voltage of other published IROSes may be known/estimated from references [2-5, 8, 9]. They were usually larger than 10 mV even at a temperature higher than 600 °C. In some references, the voltage errors were larger than 100 mV [2, 5]. It is believed that the

quite accurate voltage measurements of the presented cells can make them good and stably functioning oxygen sensors.

Unlike an air reference oxygen sensor, the reference pO_2 of an IROS is evidently influenced by temperature as discussed in Chapter 2. Particularly care must be taken with respect to temperature measurements so that an IROS is able to determine pO_2 with a good accuracy. The temperature difference across the IRE should be as small as possible and the thermocouple detecting cell temperature should be placed as close to the IRE as possible. Calculating the pO_2 at the sensing electrode by assuming a cell temperature equal to the set point temperature of the sensor furnace may reduce the accuracy [9]. Provided that the IROS temperature is kept very constant, the accuracy can be obtained by proper calibration of an IROS.

A non-hermetic sealing, a not 100 % equilibrated binary mixture of Ni/NiO, incorrectly measured cell temperature and limitations due to measuring devices, i.e., input resistance of the voltmeter is not high enough, can cause errors. An experimental consideration about the accuracy may be worth noting. At low temperature, the resistance of an IROS may increase to such an extent that the resistance of the voltmeter reading the cell voltage starts to affect the measured cell voltage. For example, at 263 °C in air, the impedance of cell 2 (IRE/ScYSZ/CSE) was 830 kΩ at 0.1 Hz. If the input resistance of a voltmeter is not large enough, the measured cell voltage will be lowered when the cell is connected to the voltmeter. The input resistance of Keithley 2700, which was used to measure cell voltage in this study, is higher than 10 GΩ. Thus, the cell voltage was not influenced to any significant extent in the tests shown in Figure 4.4. The impregnation of SDC is effective to decrease cell impedance. The ASRs at 315 °C in air were 33 kΩ·cm^2, 17 kΩ·cm^2, 27 kΩ·cm^2 and 13 kΩ·cm^2 at 0.1 Hz for cells 2 - 5, respectively. Cell 2 had no SDC impregnation and its ASR was relatively high. Cell 3 and cell 5 had SDC impregnated into the sensing electrode and their ASRs were noticeably smaller. SDC seems effective to lower the cell impedance when it is impregnated into the sensing electrode.

The cells with the IRE impregnated by SDC showed voltages higher than the theoretical in the temperature range of 260 - 360 °C. Errors on IRE temperature measurement may possibly account for that. More experiments need to be carried out to study the phenomena. NiO nonstoichiometry might cause an error in the calculated theoretical voltage depending on how the Gibbs free energy values were obtained. The nonstoichiometry of NiO is due to nickel vacancies ($Ni_{1-x}O$), and the concentration of Ni vacancies increase with pO_2 and temperature [10, 11]. A calculation based on reference [11] shows that x is around 10^{-5} and 10^{-9} at 663 and 260 °C with a pO_2 of 1 bar, respectively. As the NiO nonstoichiometry is expected to be even further decreased under reducing conditions, this is most probably not contributing to the large errors at low temperature seen in Figure 4.4. The

deviation from the theoretical voltage at low temperature depends seemingly on the details of the sensing electrode (oxygen electrode), and the reason for the low temperature error may be found here. It is suggested that at low temperature, the electrode reaction $O_2 + 4\,e^- \leftrightarrows 2\,O^{2-}$ is not reaching equilibrium, and the cell is not at equilibrium but at a steady state [12]. The quasi-equilibrium $O_2 + 2\,e^- \leftrightarrows O_2^{2-}$, i.e. formation of the peroxide ion, might be the dominant reaction with a much lower equilibrium voltage, similar to the low open circuit voltage observed in low temperature fuels cells like the polymer electrolyte membrane fuel cell (PEMFC) [12, 13].

The response times observed in both setups show an evident asymmetry, i.e., the response time when pO_2 is changed from low to high is shorter than that of the inverse change of pO_2. Similar asymmetric response behaviors were previously reported [14, 15], and were attributed to the logarithmic dependence of the cell voltage upon the pO_2 at the sensing electrode. As discussed in Chapter 2 (see section 2.2), the asymmetrical variation in cell voltage during a pO_2 cycling is the characteristic of the process of gas mixing and should show little temperature dependence. The response times observed in the tests carried out in the small setup (Figure 4.5) is definitely temperature dependent. Therefore, kinetic factors such as electrode processes that are usually very temperature dependent may play a substantial role in the tests. This on the other hand indicates that the rate of electrode processes may in a comparable magnitude of the rate of gas mixing. The gas flow rates of the test at 663 °C in the small setup is equal to that set in the numerical simulations of Figure 2.10, i.e., 8.9 mm·s^{-1}. The numerical simulation predicted a response time of ca. 30 seconds, very close to the observed one.

The response time observed in the large setup (Figure 4.6), is absolutely longer than that observed in the small setup and show almost no dependence on temperature (Figure 4.6) and cell structure (Figure 4.7). In the tests carried out in the large setup, the gas flow rate was 1.2 mm·s^{-1}, much smaller than that in the small setup. The time of gas mixing was prolonged (see section 2.2) in the large setup so much that the response time of electrode process were in fact invisible. Due to the limitation of both setups the response time of electrode processes cannot be observed.

The tests shown in Figure 4.8 reveal that the IRE depletion is an important factor accounting for the cell voltage decrease. Though a cell voltage decrease may be attributed to various factors, i.e., electrode degradation and poisoning, IRE depletion is one of the most direct factors. Since the equilibrium pO_2 of Ni/NiO is very small, i.e., 6×10^{-18} bar at 664 °C, the depletion of an IRE, in most of cases, is due to Ni depletion instead of NiO depletion. The IRE depletion caused by a non-hermetic sealing is rather common in most of cases [2, 3, 5, 9]. In this situation, the cell voltage will be stable only in a short term, i.e., a few hours as the gas leak rate is in general fast and the oxidation of Ni is rapid at high temperature. It might be worth noting that the polarization resistance of

an IROS reaches a minimum when 2 -11 % NiO in the IRE is reduced (see more detail in Chapter 5), indicating a maximum rate of Ni oxidation/NiO reduction. In the tests shown in Figure 4.8 the initial amount of reduced NiO was 11 % for the cell subjected to a decrease in cell voltage after 15 h. The reduction amount of 11 % may account partly for the cell voltage decrease in the short period.

The stability test shown in Figure 4.9 indicates that the cell is able to serve stably for ca. 6600 h with a slight voltage drift within 5 mV. Based on the prediction of Chapter 2 the depletion period due to an electronic conduction of electrolyte should be $>10^4$ h for identical operation conditions. But it should be noted that the prediction is based on an electrolyte of 8YSZ and the cell of the test shown in Figure 4.9 used an electrolyte of ScYSZ. The simulation was based on 8YSZ as a systematic study of the electronic conduction of ScYSZ employed in this thesis is absent. The cell voltage started to decrease with a considerable rate after the voltage increase at ca. 6600 h, which might be caused by the large drop in the atmospheric temperature at that time. A large temperature drop in the inlet gas might cause cracks in the glass seal as seen in Figure 4.10. Noticeably the voltage decreased with a high rate at the end of the stability test, indicating that the Ni is oxidized with an increasing rate. Nevertheless, as the cell voltage has been proved to be able for 6600 h the cell developed in this work is suitable for practical use.

The amount of reduced NiO depends on cell structures and reduction conditions and will be discussed in details in Chapter 5. The IRE of the cells shown in Figure 4.8 were reduced at -1.1 V for 18 minutes and 755 minutes, respectively, which corresponded to the amounts of reduced NiO of 11 % and 67 %, respectively. The IRE of the cell shown in Figure 4.9 was reduced for 50 minutes at -1.0 V, which corresponded to an amount of reduced NiO of 43 %. A depleted IRE can be recovered by the electrochemical method as shown in Figure 4.8. The recoverability of the IRE may result from the composite structure. The Ni recovery needs a joint participation of oxide ion, nickel oxide and electrons. If there is no oxide ion passage within the IRE, the whole IRE cannot be recovered except the parts closely confined to the interface of IRE/electrolyte. The IRE of the presented cells used a composite electrode and the ionic passage is realized by a network of 8YSZ and/or SDC, which makes the whole IRE recoverable.

4.8 Conclusion

Durable internal reference oxygen sensors, which use the equilibrium pO_2 of the binary mixture of Ni/NiO as the reference, are demonstrated. The cells may use suitable composite sensing electrode or Pt sensing electrode, but the composite sensing electrode is proven advantageous over Pt with respects to the error in cell voltage at temperatures below 450 °C, cell resistance and working temperature range. The presented cells were fabricated by a flexible and potentially low cost method. The cell performance was elaborately evaluated in terms of accuracy, stability, response time, tolerance to thermal and pO_2 cycling and the recoverability, which are the key features for a commercial product. More than 200 cells have been fabricated and more than 30 cells have been tested. Both cell fabrication and performance are highly reproducible. Thus a well performing and reproducible internal reference oxygen sensor that can be applied in practice has been developed.

References

1. D. Drouin, A. R. Couture, R. Gauvin, P. Hovington, P. Horny, CASINO(v2.42), http://www.gel.usherb.ca/casino/.
2. E. van Setten, T. M. Gür, D. H. A. Blank, J. C. Bravman and M. R. Beasley, Miniature Nernstian oxygen sensor for deposition and growth environments, Rev. Sci. Instrum., 73(2002) 156-161.
3. A. G. Mortimer and G. P. Reed, Development of a robust electrochemical oxygen sensor, Sens. Actuators, B, 24-25 (1995) 328-335.
4. F. J. G. Monreal and G. Vitter, Measurement of low oxygen pressures with a solid-state electrolyte miniaturized sensor, J. Phys. E: Sci. Instrum., 16(1983) 361-364.
5. A. K. M. S. Chowdhury, S. A. Akbar, S. Kapileshwar, and J. R. Schorr, A Rugged Oxygen Gas Sensor with Solid Reference for High Temperature Applications, J. Electrochem. Soc., 148(2001) G91-G94.
6. K. J. Vetter, Electrochemical kinetics: theoretical aspects, Academic Press, New York, London, 1967.
7. H. Schmalzried, Chemical kinetics of solids, Wiley-VCH, Weinheim, 1995.
8. D. M. Haaland, Internal-Reference Solid-Electrolyte Oxygen Sensor, Anal. Chem., 49(1977) 1813-1817.
9. J. V. Spirig, R. Ramamoorthy, S. A. Akbar, J. L. Routbort, D. Singh and P. K. Dutta, High temperature zirconia oxygen sensor with sealed metal/metal oxide inernal reference, Sens. Actuators, B, 124(2007) 192-201.

10. W. C. Tripp, N. M. Tallan, Gravimetric Determination of Defect Concentrations in NiO, J. Am. Ceram. Soc., 53(1970) 531-533.

11. S. P. Mitoff, Electrical Conductivity and thermodynamic equilibrium in Nickel Oxide, J. Chem. Phys., 35(1961) 882-889.

12. J. P. Hoare, Rest potentials in the Platinum-oxygen-acid system, J. Electrochem. Soc., 109(1962) 858-865.

13. J. Zhang, Y. Tang, C. Song, J. Zhang, H. Wang, PEM fuel cell open circuit voltage (OCV) in the temperature range of 23 °C to 120 °C, J. Power Sources, 163(2006) 532-537.

14. J. E. Anderson and Y. B. Graves, The transient response of ZrO_2 oxygen sensors to step changes in gas composition, J. Appl. Electrochem., 12(1982) 335-341.

15. J. Fouletier, H. Seinera and M. Kleitz, Measurement and regulation of oxygen content in selected gases using solid electrolyte cells. I. Discontinuous use of gauges, J. Appl. Electrochem., 4 (1974) 305-315.

5 Electrochemical reduction of NiO

Electrochemical reduction of NiO is discussed in this chapter. The composites of $(La_{0.75}Sr_{0.25})_{0.95}O_{3\pm\delta}$ (LSM25) and 8 mol % yttria stabilized zirconia (8YSZ) is verified to be superior oxygen electrode materials over Pt in terms of a lower overpotential. The electrochemical reduction of NiO may exhibit an induction period, and the maximum reduction rate is obtained when 2 - 11 % NiO is reduced. The kinetics of electrochemical reduction of NiO can be described by the Avrami equation. Parts of this chapter have been submitted as Q. Hu, T. Jacobsen, K. V. Hansen and M. Mogensen, "Electrochemical reduction of NiO in a composite electrode", Solid State Ionics (2012).

5.1 Introduction

The internal reference electrode (IRE) of the IROS must be reduced partially to form the binary mixture of Ni/NiO before the cell becomes functional. As introduced before (see chapter 3) generating the binary mixture of Ni/NiO *in situ* by electrochemical reduction of NiO can avoid the inadvertent oxidation of Ni during cell fabrication and can be used to control sophisticatedly the reduction degree of the internal reference electrode.

Compared with the studies on the reduction of NiO by hydrogen [4-7], occasionally by carbon [8-10], the study focusing on electrochemical reduction of NiO rarely attracts attention. In the studies of reducing NiO by hydrogen, the remarkable effects of steam partial pressure, pH_2O, on the reduction rate and an induction period have been revealed [11, 13]. José et al. [11] did elaborate work on the reaction between NiO and hydrogen, theoretically and experimentally, and found that 1) the transformation from NiO to Ni is direct and no accumulation of any intermediate phase occurs during the reduction; 2) the surface defects such as O vacancies that may form during crystal growth directly correlate with the reduction rate. During the induction period, surface defect sites are created that provide a high efficiency for the dissociation of H_2.

5.2 Experimental

The cell fabrication details are given in chapter 3. In the study of electrochemical reduction of NiO, the cells were placed in an alumina test house with an inner diameter of 69 mm, a length of 495 mm, and room for four

cells to be tested in one batch (see chapter 4). The pO_2 inside the test setup was controlled by mass flow controllers and the source gas species included compressed air, oxygen and nitrogen. The minimum and maximum flow rate of the mass flow controllers were 0.1 and 6 slph (standard liters per hour), respectively. Provided the electrolyte is an (almost) pure oxide ion conductor, which is the case for ScYSZ and 8YSZ, the cell voltage, V_{cell}, the pO_2 at the internal reference electrode, p_R, and the pO_2 at the sensing electrode (SE), p_S, satisfy the Nernst equation:

$$V_{cell} = \frac{RT}{4F} \ln \frac{p_S}{p_R}$$

(5.1)

So the pO_2 at the internal reference electrode, p_R, can be determined if the pO_2 at the sensing electrode, p_S, and the cell voltage, V_{cell}, are known, and vice versa. For example, if the binary mixture of Ni/NiO is not formed within the internal reference electrode, then the p_R can be known by measuring the cell voltage, V_{cell}, and setting the p_S by mass flow controllers. On the other hand, if the binary mixture of Ni/NiO is formed the p_R is then well defined by the thermodynamic equilibrium of Ni/NiO and the pO_2 at the sensing electrode, p_S, can be determined by measuring the cell voltage. Denoting the potential of the internal reference electrode versus SE by E_{IRE}, the cell voltage defined by Eq. (5.1) is in fact equal to the negative potential of the internal reference electrode:

$$E_{IRE} = -V_{cell}$$

(5.2)

followed by a specification of the conditions at the sensing electrode, i.e., pO_2 and temperature.

Voltage sweeps were performed, with a rate of 1, 5, 10 and 20 $mV \cdot s^{-1}$, respectively, on cells based on a Pt sensing electrode or a composite sensing electrode (CSE) of LSM25/8YSZ. The voltage sweeps should not be regarded as real potential sweeps on the internal reference electrode as the resistance of the sensing electrode was not negligible in experiments (see chapter 6).

Internal reference electrodes were reduced at a constant cell voltage of 0.9 or 1.1 V that corresponded to an E_{IRE} of -0.9 or -1.1 V, below the equilibrium potentials of Ni/NiO at the relevant conditions. Chronoamperometry was carried out for voltage sweeps and for the reduction of NiO at a constant voltage. From the curve of current vs. time the amount of NiO reduced can be determined. Electrochemical impedance spectroscopy (EIS) was performed with a voltage applied on the cell. When the binary mixture of Ni/NiO was not formed a cell voltage was applied on the cell for a time sufficient (> 5 minutes) to ensure that the current passing through the cell was less than 5 microampere, and then the impedance spectroscopy was performed with this voltage. The formation of the binary mixture of Ni/NiO made the cell immediately have a stable and well defined open circuit voltage (OCV), which was very close to the thermodynamic value [1]. In this case the impedance spectroscopy was

carried out at the OCV. All of the electrochemical tests were performed with a Solartron 1250 frequency response analyzer along with a Solartron SI 1287 electrochemical interface. The electrochemical measurement software was Elchemea 6.0 that was developed in-house. The involved thermodynamic calculations were carried out by FactSage[TM] 5.5 [14].

Electrochemical reduction of NiO was stopped when the desired reduction degree was reached. The temperature was then decreased with a rate of 5 ºC·min^{-1}. After sample polishing, microstructure, morphology and chemical composition of NiO at different degrees of reduction were investigated in a Zeiss Supra 35 field emission gun scanning electron microscope, equipped with a Noran System Six Model 3000 energy dispersive X-ray spectrometer.

5.3 Results

5.3.1 Voltage sweeps

1) Effects of sweep rate

The first voltage sweeps from 0 to 2 V, corresponding to the potential of the internal reference electrode from 0 to -2.0 V, are shown in Figure 5.1. The shown sweep curves were collected from four newly fabricated cells because the sweep curve was different from the following curves that all were identical to the second sweep curve (see chapter 4) [1]. The sweep rates were 1, 5, 10 and 20 mV·s^{-1}, respectively, and the sweeps were performed on cells based on a Pt sensing electrode at 664 ºC in air. The equilibrium potential of Ni/NiO, $E_{Ni/NiO}$, is -770 mV vs. SE (p_S=0.21 bar) at 664 ºC but the current density is seen to increase discernibly from more negative potentials. The sweep rates influenced the sweep results. Increasing the sweep rate from 1 to 5 mV·s^{-1} the current density started to increase from a more negative potential, i.e., from ca. -1.05 to ca. -1.10 V. Further increasing the sweep rate, i.e., to 5, 10 and 20 mV·s^{-1}, only slight changes were observed for this potential. The reduction current density started to decay when the potential of the internal reference electrode was below -1.6 V for the sweeps with a relatively high rate such as 10 or 20 mV·s^{-1}. For the sweeps with a relatively low rate such as 1 or 5 mV·s^{-1}, two peaks can be recognized. The voltage interval between the two peaks decreased when the sweep rate was increased from 1 to 5 mV·s^{-1} and vanished when the sweep rate was increased to 10 mV·s^{-1}. The peak current density in general increased with increasing sweep rate. Though the peak current densities of the sweeps with a rate of 10 and 20 mV·s^{-1} were equal, the current density was maintained at a higher level for the faster sweep after the decay in current density. For example the current density at -1.9 V for the sweep with a

75

rate of 20 mV·s^{-1} was -35 mA·cm^{-2} and it was -26 mA·cm^{-2} for the sweep with a rate of 10 mV·s^{-1}. It has been verified by tests of more than 40 cells that if the reduction of NiO is initiated the cell will develop a stable OCV that is fairly close to the thermodynamic value, indicating the formation of a metallic Ni phase in contact with NiO [1].

Figure 5.2 shows the sweep sections between 0 and -0.6 V of Figure 5.1. The peak current density and peak position were found also to be influenced by sweep rates. The peaks shown in Figure 5.2 corresponded to removal of the residual oxygen sealed in the porous internal reference electrode [1]. It is noticed that the currents were anodic when the voltage sweeps were initiated at 0 V, showing that the pO$_2$ in the gas enclosed during the sealing process after cooling was lower than that in air.

Figure 5.1. Current density as a function of the potential of the internal reference electrode versus the sensing electrode for the first voltage sweeps with varied sweep rates. Each sweep was made on a newly fabricated cell with Pt as the sensing electrode. Note that the x axis has increasing negative numbers in the direction towards right. The apparent peaks below -1.0 V corresponded to NiO reduction.

Figure 5.2. Current density as a function of the potential of the internal reference electrode versus the sensing electrode for the first voltage sweeps with varied sweep rates. Each sweep was made on a newly fabricated cell with Pt as the sensing electrode. The plots were magnified section between 0 and -0.6 V of Figure 5.1. The apparent peaks corresponded to removal of the residual oxygen sealed in the internal reference electrode.

2) Effects of counter electrode

Figure 5.3 presents sweep curves that were obtained on cells with the sensing electrodes made from Pt and the composite of LSM25/8YSZ, respectively, and the sweep rates were 1 mV·s⁻¹. For the cell based on the composite of LSM25/8YSZ the sweep curve was seen to move towards less negative potentials, meaning that the current density indicating NiO reduction increased from a lower cell voltage. Particularly the two peaks were better separated. For the cell with a Pt electrode the two peaks merged partially.

Figure 5.3. Current density as a function of the potential of the internal reference electrode versus the sensing electrode for the first voltage sweeps. The voltage sweeps were carried out on cells with the sensing electrode made from Pt and the composite of LSM25/8YSZ, respectively. Each sweep was made on a newly fabricated IROS.

3) Effects of temperature

Figure 5.4 shows effects of temperature on the first voltage sweeps. The sweep rate was 5 mV·s^{-1} and the experimental temperatures were 617, 664 and 684 ºC, respectively. The sweep results were collected from three cells based on the composite sensing electrode of LSM25/8YSZ. An increase in temperature increased the peak current density and made the peak steeper. Due to the higher sweep rate the distinct peaks shown in Figure 5.3 were less pronounced and at 684 ºC they merged into one sharp peak.
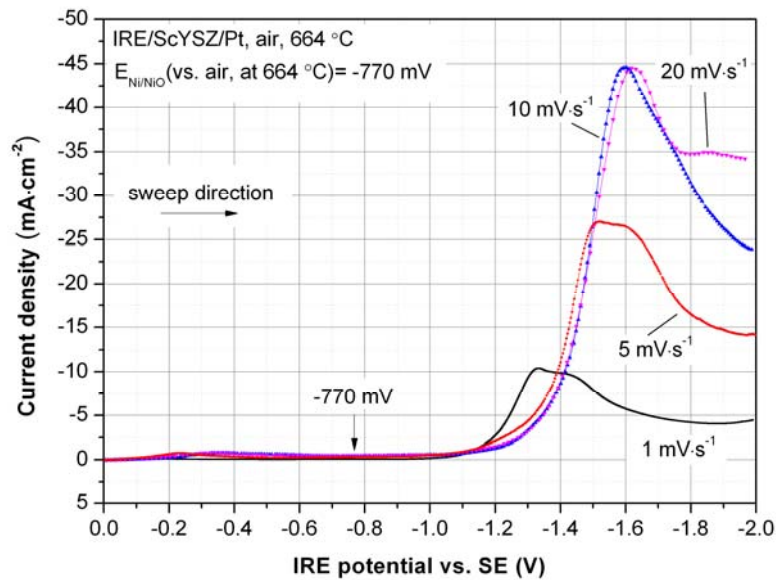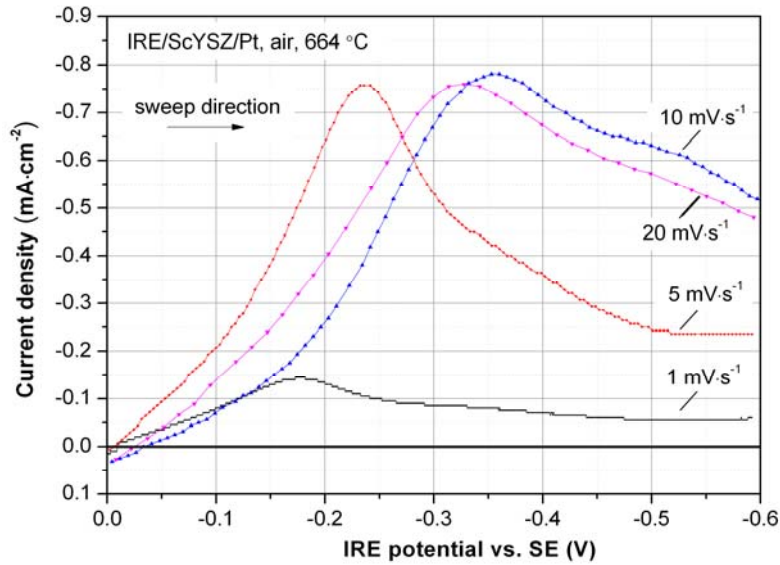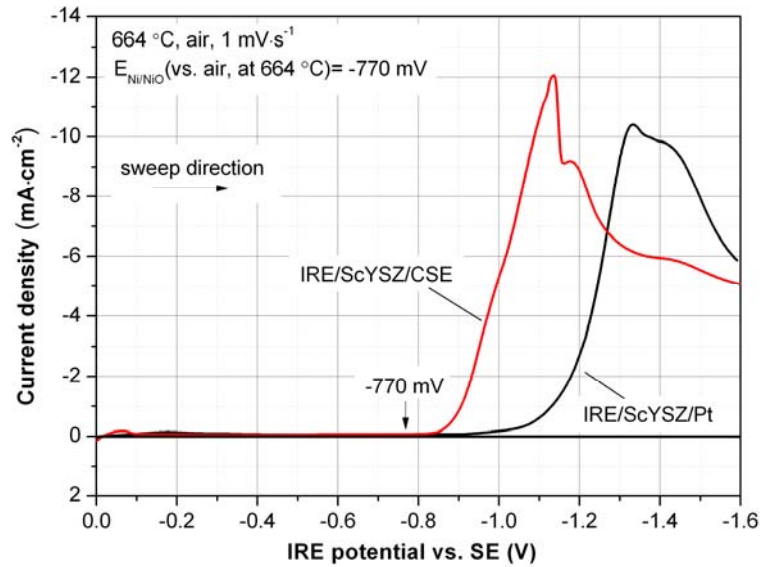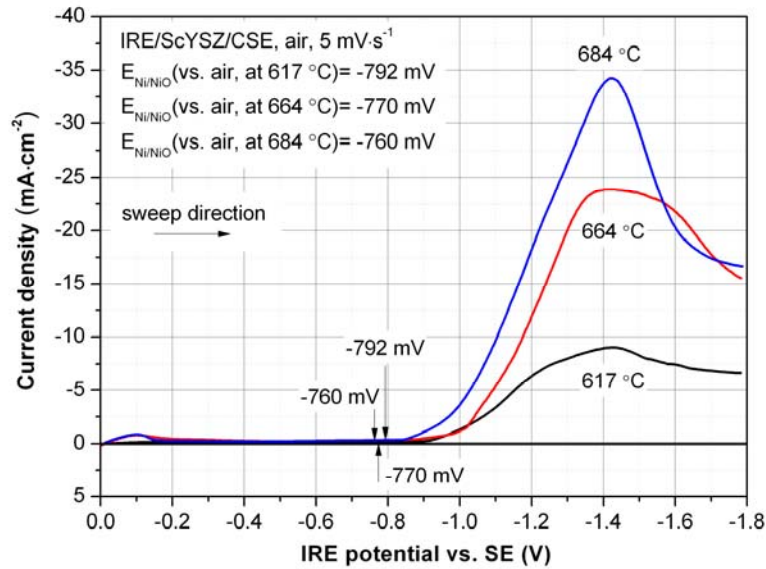
Figure 5.4. Current density as a function of the potential of the internal reference electrode versus the sensing electrode for the first voltage sweeps. The voltage sweeps were carried out on cells based on the composite of LSM25/8YSZ. Each sweep was made on a newly fabricated cell. The experimental temperatures were 617, 664 and 684 °C, respectively.

5.3.2 Reducing NiO at a constant cell voltage

Figure 5.5 shows the variation in current density when the internal reference electrode is reduced at a constant cell voltage that corresponded to the potential of the internal reference electrode, E_{IRE}, below the equilibrium potential of Ni/NiO at the corresponding condition. The three reduction conditions were: 1) V_{cell} = 0.9 V at 664 °C; 2) V_{cell} = 0.9 V at 684 °C; 3) V_{cell} = 1.1 V at 664 °C. The temperature was increased by 20 °C from experiment 1 to 2, which resulted in a higher current density. Increasing the voltage by 200 mV from experiment 1 to 3 also resulted in a much higher peak current density. In all experiments the current densities decreased initially, which, as mentioned above, corresponded to removal of the residual oxygen sealed in the internal reference electrodes. From the charge passed after the current density had initially decreased to the minimum the amount of reduced NiO was calculated. The degree of reduced NiO, as a function of time, is shown with respect to the right axis. The time was counted from the start of applying the cell voltage and the time scales are given in minutes (bottom axis) and seconds (top axis) respectively. The current density passed a broad minimum before it started to increase. From experiment 1 to 2, an increase in temperature by 20 °C narrowed the period slightly

79

whereas the increase in cell voltage by 200 mV shortened the period significantly. The peak current density after the minimum corresponded to a small fraction of reduced NiO. At the peak current density the degrees of reduced NiO in experiment 1, 2 and 3 were 5, 11 and 2 %, respectively. In the decay of the current density an approximately logarithmic dependence of the reduction degree of NiO on time was seen.
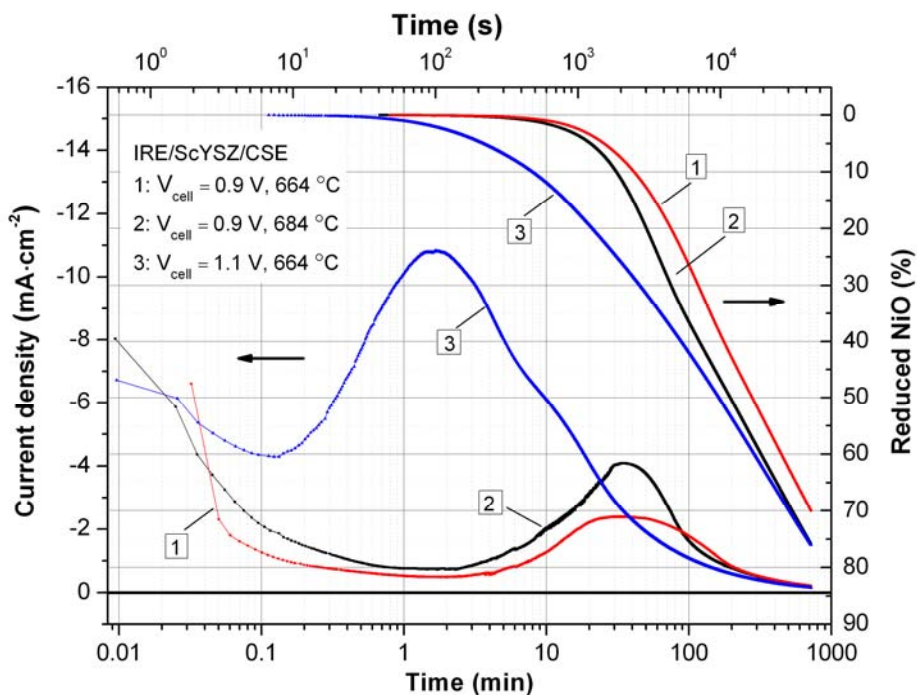
Figure 5.5. The variation in current density when the internal reference electrode is reduced at a constant cell voltage. The current density is shown with respect to the left axis and the degree of reduced NiO is shown with respect to the right axis. The time, counted from the start of applying the cell voltage, are shown in minutes (bottom axis) and seconds (top axis) respectively. The chronoamperometry was performed from the time when the current density had initially decreased to the minimum. At the peak current density the degree of reduced NiO in experiment 1, 2 and 3 were 5 %, 11 % and 2 %, respectively.

5.3.3 Microstructures of NiO at different reduction degrees

Internal reference electrodes with different degrees of reduced NiO were prepared. The reduction of theses electrodes were performed at 664 °C and on cells with the composite LSM25/8YSZ as the sensing electrode. The reduction cell voltage was 0.9 V, corresponding to the condition of experiment 1 in Figure 5.5.

Figure 5.6 shows the microstructures of Ni/NiO particles. (a) shows an unreduced NiO particle. (b) presents the cross section of Ni/NiO particles when 2 % of NiO was reduced. (c) and (d) show the cross section and morphology of Ni/NiO particles when 54 % of NiO was reduced. When 2 % NiO was reduced the current density was increasing rapidly. As seen from (b) Ni particles in a size of tens of nanometers were forming at the surface of the NiO particles. When 54 % of NiO was reduced the current density was decaying. As seen from (c) a large amount of Ni particles in nano scale covered the NiO particles, and the ex-NiO particle became a particle with many "large" holes as shown in (d).
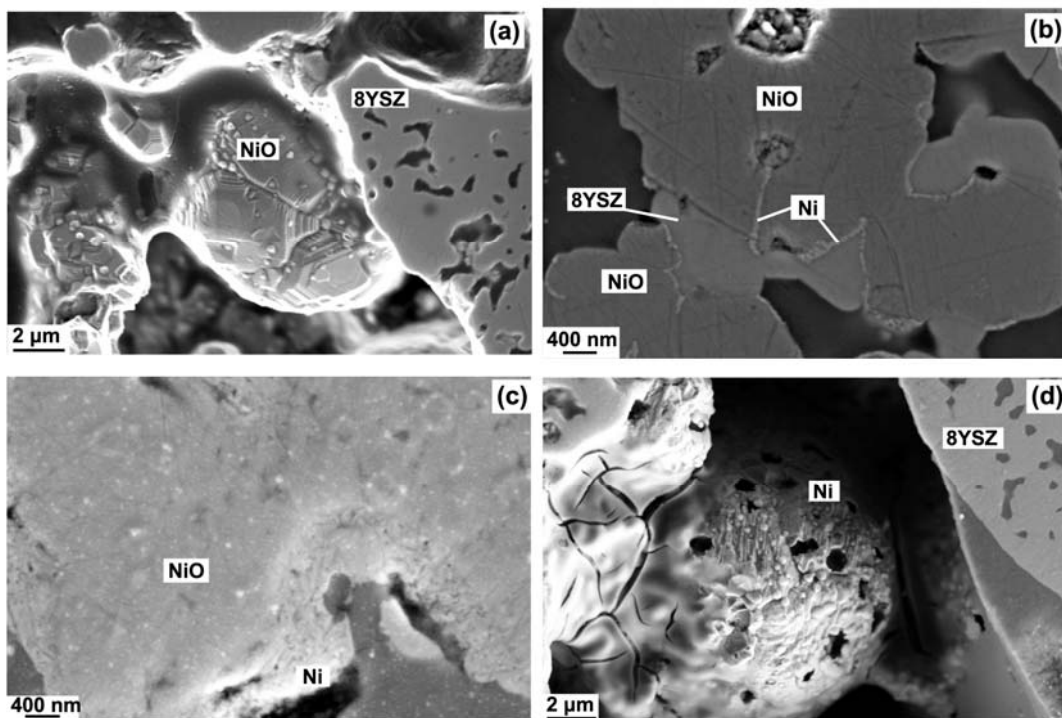
Figure 5.6. Microstructures of NiO particles at different reduction degrees. (a) An unreduced NiO particle. (b) The cross section of Ni/NiO particles when 2 % of NiO was reduced. (c) The cross section, (d) The morphology of Ni/NiO particles when 54 % of NiO was reduced.

5.3.4 Impedance spectroscopy during NiO reduction

All the impedance spectra employed in this chapter are listed in Table 5.1 and they were measured at 684 ℃ with the pO_2 at the sensing electrode equal to 1.01 bar. At these conditions, the equilibrium potential of Ni/NiO is -792 mV. From spectrum 1 to 3 the potential of the internal reference electrode was above the equilibrium

potential during the impedance spectroscopy. Preceding the measurements of spectrum 4 and 5 the internal reference electrode was applied a potential of -800 mV for 5 and 60 minutes, respectively, which did not make the cell develop a stable OCV, so the impedance spectroscopy was carried out with a potential of -800 mV applied on the internal reference electrode. From spectrum 6 to 12 the internal reference electrode was applied a potential of -900 mV before the impedance spectroscopy, which made the cell develop a stable OCV of -791 mV, very close to the equilibrium potential. Therefore spectra 6 to 10 were all measured with the potential of -791 mV, instead of -900 mV, applied on the internal reference electrode. The stable OCV indicated the reduction of NiO. From spectrum 6 the degrees of reduced NiO were counted.

Table 5.1. List of impedance spectra.

Experimental conditions for the impedance spectroscopy on the cell with a structure of IRE/ScYSZ/CSE: temperature, 684 °C, pO_2 at the sensing electrode, 1.01 bar. The equilibrium potential of Ni/NiO versus SE (p_S=1.01 bar) is -792 mV.

No.	E_{IRE} (before EIS)	E_{IRE} (during EIS)	OCV	p_R	time	Reduced NiO
	(mV)	(mV)	(mV)	(bar)	(min)	(%)
1	-30	-30	N/A	0.24	N/A	N/A
2	-50	-50	N/A	9.1×10^{-2}	N/A	N/A
3	-100	-100	N/A	7.9×10^{-3}	N/A	N/A
4	-800	-800	N/A	1.4×10^{-17}	5	0
5	-800	-800	N/A	1.4×10^{-17}	60	0
6	-900	-791	791	2.1×10^{-17}	5	0.2
7	-900	-791	791	2.1×10^{-17}	15	0.6
8	-900	-791	791	2.1×10^{-17}	35	3.3
9	-900	-791	791	2.1×10^{-17}	95	20.9
10	-900	-791	791	2.1×10^{-17}	155	36.3
11	-900	-791	791	2.1×10^{-17}	275	51.5
12	-900	-791	791	2.1×10^{-17}	515	63.7

Nyquist plots of spectrum 1 to 3 are shown in Figure 5.7 and the sections of high frequency are presented in the inset. From spectrum 1 to 3 the potential of the internal reference electrode was -30, -50, -100 mV, respectively,

and the reduction of NiO was not initiated. The spectra consisted of three arcs that were tagged with A1, A2 and A3 from high to low frequency. For illustration the three arcs are indicated for spectrum 1. Arc A1 and A2 were suppressed arcs and arc A2 increased significantly with decreasing pO_2 at the internal reference electrode. In the frequency range applied, the imaginary part of arc A3 increased almost vertically with decreasing the frequency, which is the characteristic of the impedance spectrum of a capacitor. As indicated by the inset, the sections of high frequency moved towards larger impedance when the pO_2 at the internal reference electrode was reduced.
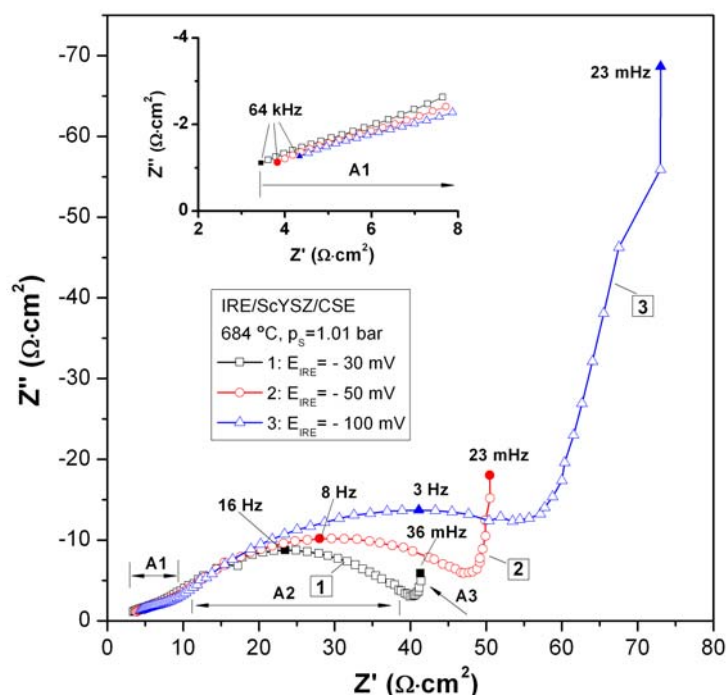
Figure 5.7. Nyquist plots of spectrum 1, 2 and 3. The potentials of the internal reference electrode were -30, -50 and -100 mV, respectively. The sections of high frequency are shown in the inset.

Nyquist plots of spectrum 4 to 7 are shown in Figure 5.8 and the sections of high frequency are presented in the inset. The arcs constituting the spectra are tagged from B1 to B3. In spectrum 4 and 5, arc B2 was dominant and arc B3 was invisible. Applying a potential of -800 mV that was below the equilibrium potential on the internal reference electrode for 60 minutes did not make the cell develop a stable OCV. From spectrum 4 and 5, applying a potential of -800 mV on the internal reference electrode for 55 minutes more made only a slight decrease in arc B2, and the section of high frequency, shown in the inset, kept unchanged. After applying a potential of -900 mV on the internal reference electrode for 5 minutes, the impedance of spectrum 6, including the section of high frequency, was noticeably lower than that of spectrum 5, and spectrum 6 comprised three arcs again. From spectrum 6 to 7 the potential of -900 mV was applied for 10 minutes more on the internal reference electrode.

Arc B2, B3 and the high frequency impedance kept decreasing, meanwhile the summit frequency of arc B2 increased from 226 to 715 mHz.
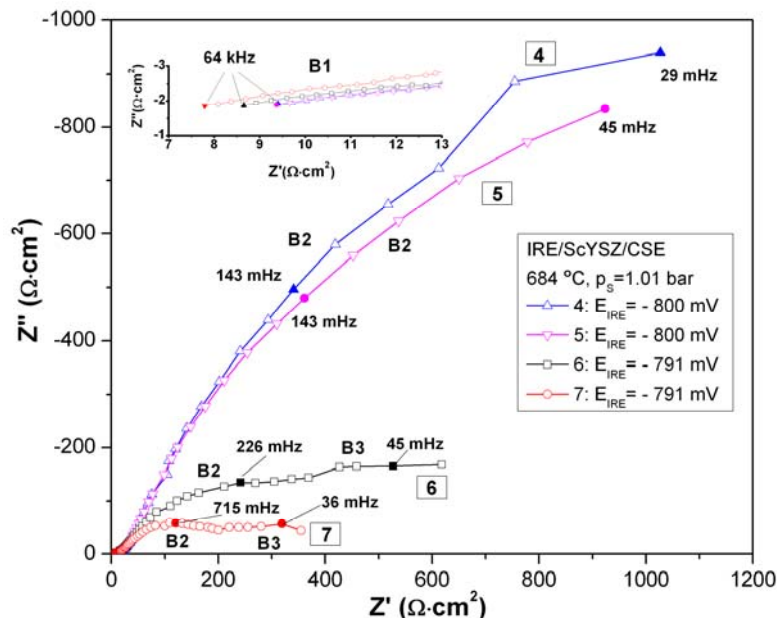
Figure 5.8. Nyquist plots of spectrum 4 to 7. For spectrum 4 and 5 the potential of the internal reference electrode was -800 mV during the impedance spectroscopy. The potential of the internal reference electrode of spectrum 6 and 7 was -900 mV before the impedance spectroscopy and was -791 mV during the impedance spectroscopy. See more information of the spectra in Table 5.1. Reduction of NiO caused a significant decrease in arc B2 and B3, meanwhile the high frequency impedance was reduced.

Figure 5.9 shows the impedance spectra, from 8 to 12, when more than 3.3 % of NiO were reduced. (a) presents all Nyquist plots except spectrum 11, with the sections of high frequency shown in the inset. (b) shows the Bode plots of imaginary part of spectrum 9 to 12. Spectrum 11 has been omitted in (a) for the reason of clarity. From spectrum 7 (Figure 5.8) to spectrum 9 (Figure 5.9(a)) the degree of reduced NiO was increased from 0.6 to 20.9 % and the polarization resistance of the cell decreased substantially due to a major decrease in arc B2 and B3. The polarization resistance decreased from ca. 400 $\Omega \cdot cm^2$ to ca. 30 $\Omega \cdot cm^2$ and arc B3 was invisible in spectrum 9. As seen in the inset the impedance of high frequency was also decreased. Further reducing NiO from 20.9 % (spectrum 9) to 63.7 % (spectrum 12), the polarization resistance started to increase but the impedance of high frequency was unchanged. In Figure 5.9(a) the increase of polarization resistance was seen to be represented by the reoccurrence of arc B3. In the Bode plot of Figure 5.9(b), the summit frequency of arc B2 is clearly shown to be held at 13 Hz and the increase of the polarization resistance was exclusively reflected by the increase in arc B3.
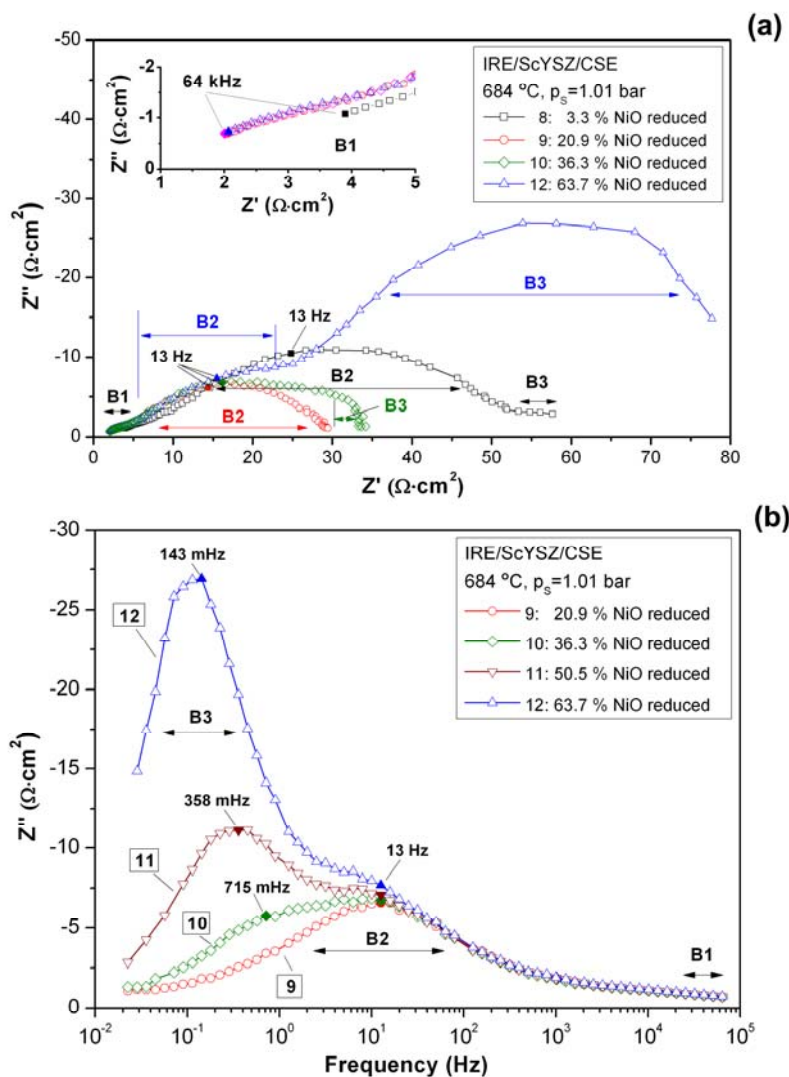
Figure 5.9. Impedance spectra measured when the degree of reduced NiO was above 3.3 %. (a) Nyquist plots of spectrum 8 to 12 except spectrum 11. The sections of high frequency are shown in the inset. (b) Bode plots of imaginary part of spectrum 9 to 12. See more details of impedance spectra in Table 5.1.

5.4 Discussion

In the voltage sweeps shown from Figure 5.1, 5.3 and 5.4, overpotentials are seen and the current densities start to increase discernibly from a potential below the equilibrium potential of Ni/NiO at the condition. In general the slower the voltage sweep the closer is this potential to the equilibrium potential. In Figure 5.3 the composite of

LSM25/8YSZ shows evident superiority as the electrode materials over Pt for oxygen sensors in terms of a lower overpotential. It might be worthy estimating the electronic current density of the electrolyte during voltage sweeps. Based on the calculation given in chapter 2 the electronic current densities is ca. 7×10^{-4} mA·cm^{-2} when the IRE potential is -0.8 V at 664 °C, i.e., negligible compared with the current density observed.

Two peaks can be recognized in Figure 5.3 during the voltage sweeps. The two peaks are more evident at a smaller sweep rate (Figure 5.1), a lower temperature (Figure 5.4) and for the cell based on the composite of LSM25/8YSZ (Figure 5.3). The peaks manifest themselves regardless of the sensing electrode, so they indicate electrochemical processes occurring in the internal reference electrodes, particularly the reduction of NiO. The NiO powder used for the internal reference electrodes contained a calcined part and an uncalcined part. As calcination will make the particles of NiO larger there is a distribution of NiO particles with two major sizes in the internal reference electrodes and the two peaks of current density may correspond to the reduction of NiO taking place over the NiO particles with the different sizes.

The contacts between Ni and NiO are changing during NiO reduction, which may account for the increase in current density followed by a decay. The electrochemical reduction of NiO can in general be expressed as:
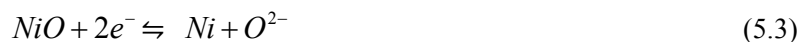
$$NiO + 2e^- \leftrightarrows Ni + O^{2-}$$

(5.3)

A joint participation of NiO, Ni and O^{2-} is necessary for the reaction to proceed. As seen in Figure 5.6(a) and (b) the contact between metallic Ni and NiO increases initially by forming Ni particles on the surface of NiO particles/agglomerates. However once the surface of NiO is covered by Ni particles the effective contact area between Ni and NiO starts to decrease. Approximating Ni particles by a sphere model the contact area between Ni/NiO is proportional to the square of the equivalent radius of the NiO particle. With reduction of NiO the radius of NiO particles decreases, resulting in a reduced contact area between Ni and NiO. Though an increase in the contact area between Ni and 8YSZ is indicated by Figure 5.6(b), it will be counteracted by a corresponding decrease in the contact area between NiO and 8YSZ.

The peak(s) of current density during NiO reduction may also be understood by the mechanism of the nucleation and growth of Ni particles [17], which results in a similar variation in the contact area between Ni and NiO particles. The reason for each peak may be that soon after the nucleation of Ni particles, the NiO will become depleted near the growing Ni nuclei and thus the current density decreases. Two different nucleation regions or nucleation site populations, i.e. over the surfaces of calcined and uncalcinated NiO particles, will give the two

86

peaks of the current density during NiO reduction. The size of the Ni particles shown in Figure 5.6(c) is ca. 40 nm, which may result from this nucleation-depletion mechanism.

In Figure 5.5 a period in which the current passes a broad minimum is seen. Though the period may result from a balance between the decreasing current of the residual oxygen removal and the increasing current of NiO reduction, it very likely indicates that an induction period is required for the electrochemical reduction of NiO. An induction period has been observed in the reduction of NiO by hydrogen [11]. In the induction period not only nucleation of Ni particles, but also the generation of oxide vacancies in NiO may take place. Though metallic vacancies are the prevailing defects in NiO crystals [18, 19], oxide vacancies may be formed at a very low pO_2 via:

$$O_X^X \leftrightharpoons \frac{1}{2}O_2(g) + V_O^{\cdot\cdot} + 2e^{'} \tag{5.4}$$

The increasing oxygen vacancy concentration can make the structure of NiO more and more unstable and end up with a collapse of the crystal, i.e., via the reactions:

$$Ni_{Ni}^X + O_X^X + 2e^- \leftrightharpoons Ni + O^{2-} \tag{5.5}$$

or

$$V_O^{\cdot\cdot} + V_{Ni}^{''} = nil \tag{5.6}$$

The kinetics of NiO reduction by hydrogen was previously discussed via the Avrami equation [4]:

$$x_{NiO} = 1 - \exp(-kt^m) \tag{5.7}$$

where x_{NiO} is the fractional conversion of NiO at time t, k is an overall rate constant, and m is an exponent whose value (0.5 - 4) depends on the grain geometry and the limiting step (i.e., chemical nucleation or diffusion) [4]. The Avrami equation [20-22] fits well the corresponding fractions of reduced NiO shown in Figure 5.5. With the time scale of second, the parameters for the three experiments are: k= (1.19±0.01) $\times 10^{-3}$ and m=0.65±0.01 for experiment 1, k= (2.72±0.01) $\times 10^{-3}$ and m=0.59±0.01 for experiment 2, and k= (7.31±0.01) $\times 10^{-3}$ and m=0.49±0.01 for experiment 3. In case of the electrochemical reduction of NiO, the exponent, m, is in a relatively narrow range of 0.5 - 0.7 that may indicate a mechanism of the nucleation and growth of Ni particles, and the overall rate constant, k, increases with temperature and the applied voltage, especially the latter.

In Figure 5.6(b) Ni particles are found to be able to form at the cracks inside NiO particles. It is reasonable to believe that oxide ions can migrate among Ni particles because these cracks have very likely no access to the oxide ion conducting 8YSZ. Oxygen ions may be removed via a gaseous mechanism but it will be very difficult

due to the significant difference in electronegativity between Ni and oxygen. A bulk diffusion of oxide ion through NiO particles might be active during NiO reduction. By this mechanism, the diffusion of oxide ions is driven by the difference in the vacancy concentration of oxide ions within NiO particles. The removal rate of oxide ions by this mechanism will be slow due to a rather limited concentration of oxide vacancies.

In Figure 5.9 (a) the minimum polarization resistance is observed when 20.9 % of NiO is reduced. But the reduction degree of 20.9 % may not correspond to the real minimum polarization resistance during NiO reduction since the impedance spectroscopy was carried out intermittently and the real minimum polarization was possibly missed. In fact in the uninterrupted the experiments shown in Figure 5.5, the degrees of reduced NiO are 5, 11 and 2 % at the peak current density for experiment 1, 2 and 3 respectively, indicating that the maximum reduction rate is obtained when 2 - 11 % NiO is reduced.

It is quite interesting that the increasing resistance for NiO reduction can be exclusively reflected by the increasing arc B3 as shown by Figure 5.9(a). In the entire range investigated, 3.3 - 63.7 % of reduced NiO, the impedance does not change by orders of magnitude and is indeed suited for practical applications. In Figure 5.8 arc B2 decreases substantially on the reduction of NiO, showing that NiO reduction/Ni oxidation, i.e., the reaction indicated by Eq. (5.3), is the active process.

In Figure 5.7 the impedance spectra measured before the reduction of NiO consist of two suppressed circular arcs, A1 and A2 in series with a capacitor A3. This is expected for an oxygen electrode in contact with a limited volume of oxygen [23] and demonstrates the effective sealing of the compartment of the internal reference electrode. A hermetic sealing of the internal reference electrode is vital for producing a functional IROS [24], impedance spectroscopy therefore can be used as an effective tool to diagnose the hermaticity of the seal prior to the reduction of the internal reference electrode.

5.5 Conclusion

Overpotentials were seen in the voltage sweep curves of NiO reduction. The composite of LSM25/8YSZ can be superior electrode materials over Pt for oxygen sensors in terms of a lower overpotential.

Peak(s) of current density are seen during the electrochemical reduction of NiO and they may result from the variation in contact area between Ni/NiO and/or the nucleation of Ni particles. The effective contact area between Ni/NiO changes during NiO reduction. It initially increases with more Ni particles formed but hereafter decreases with more NiO reduced when the surface of NiO particles is covered by Ni particles. Similarly the Ni particles nucleate during NiO reduction, and the NiO will become depleted near the growing Ni nuclei and thus the current density decreases. The formed Ni particles are found in a size of ca. 40 nm.

The kinetics of electrochemical reduction of NiO may be described by the Avrami equation. In the experiments the exponent of the Avrami equation was in a relatively narrow range of 0.5 - 0.7 that may indicate a nucleation and growth mechanism. The overall rate constant varies from 1.19 to 7.73 $x10^{-3}$ and increases with temperature and the applied voltage, especially the latter.

The maximum rate of NiO reduction is obtained when 2 - 11 % NiO is reduced. The increasing resistance during NiO reduction can be exclusively expressed by one arc at low frequencies in the impedance spectra. When NiO is not reduced the impedance spectrum of a cell consists of two suppressed arcs in series with a capacitor, which may be used to diagnose the hermaticity of the sealed NiO/8YSZ electrode.

References

1. Q. Hu, T. Jacobsen, K. V. Hansen and M. Mogensen, Improved internal reference oxygen sensor with composite ceramic electrodes. J. Electrochem. Soc., 159(2012) B811-B817.
2. A. Nakamura and J. Bruce Wagner, Jr., Defect structure, ionic conductivity, and diffusion in yttria stabilized zirconia and related oxide electrolytes with fluorite structure, J. Electrochem. Soc., 133(1986) 1542-1548.
3. V. V. Kharton, F. M. B. Marques and A. Atkinson, Transport properties of solid oxide electrolyte ceramics: a brief review, Solid State Ionics, 174(2004) 135-149.
4. J. T. Richardson, R. Scates and M. V. Twigg, X-ray diffraction study of nickel oxide reduction by hydrogen, Appl. Catal., A, 246(2003) 137-150.
5. J. T Richardson, R. M Scates and M.V. Twigg, X-ray diffraction study of the hydrogen reduction of NiO/α-Al$_2$O$_3$ steam reforming catalysts, Appl. Catal. A, 267 (2004) 35-46.

6. B. Janković, B. Adnađević and S. Mentus, The kinetic study of temperature-programmed reduction of nickel oxide in hydrogen atmosphere, Chem. Eng. Sci. 63(2008) 567-575.

7. B. Janković, Isothermal reduction kinetics of nickel oxide using hydrogen: Conventional and Weibull kinetic analysis, J. Phys. Chem. Solids, 68(2007) 2233-2246.

8. S. K. Sharma, F. J. Vastola and P. L. Walker Jr, Reduction of nickel oxide by carbon: I. Interaction between nickel oxide and pyrolytic graphite, Carbon, 34(1996) 1407-1412.

9. S. K. Sharma, F. J. Vastola and P. L. Walker Jr, Reduction of nickel oxide by carbon: II. Interaction between nickel oxide and natural graphite, Carbon, 35(1997) 529-533.

10. S. K. Sharma, F. J. Vastola and P.L. Walker Jr, Reduction of nickel oxide by carbon: III. Kinetic studies of the interaction between nickel oxide and natural graphite, Carbon, 35(1997) 535-541.

11. J. A. Rodriguez, J. C. Hanson, A. I. Frenkel, J. Y. Kim, and M. Pérez, Experimental and theoretical studies on the reaction of H2 with NiO: role of O vacancies and mechanism for oxide reduction, J. Am. Chem. Soc., 124(2002) 346-354.

12. M. D. Towler, N. L. Allan, N. M. Harrison, V. R. Saunders, W. C. Mackrodt and E. Aprà, Ab initio study of MnO and NiO, Phys. Rev. B, 50(1994) 5041-5054.

13. R. P. Furstenau, G. McDougall and M. A. Langell, Initial stages of hydrogen reduction of NiO(100), Surf. Sci., 150(1985) 55-79.

14. C. W. Bale, E. Bélisle, P. Chartrand, S. A. Decterov, G. Eriksson, K. Hack, I.-H. Jung, Y.-B. Kang, J. Melançon, A. D. Pelton, C. Robelin and S. Petersen, FactSage Thermochemical Software and Databases – Recent Developments, Calphad, 33(2009) 295-311.

15. T. Jacobsen and M. Mogensen, The course of oxygen partial pressure and electric potentials across an oxide electrolyte cell, ECS trans., 13(2008) 259-273.

16. M. Mogensen, T. Jacobsen, Electromotive potential distribution and electronic leak currents in working YSZ based SOCs, ECS trans., 25(2009) 1315-1320.

17. Y. Koga, L.G.Harrison, in C. H. Bamford, C. F. H. Tipper, R. G. Compton (Eds.), Comprehensive chemical kinetics, vol. 21. Elsevier, Amsterdam, 1984, 119-149.

18. S. P. Mitoff, Electrical Conductivity and thermodynamic equilibrium in Nickel Oxide, J. Chem. Phys. 35(1961) 882-889.

19. W. C. Tripp and N. M. Tallan, Gravimetric Determination of Defect Concentrations in NiO, J. Am. Ceram. Soc., 53(1970) 531-533.

20. M. Avrami, Kinetics of phase change. I General theory, J. Chem. Phys., 7(1939) 1103-1112.

21. M. Avrami, Kinetics of phase chang. II Transformation Time relations for random distribution of nuclei, J. Chem. Phys., 8(1940) 212-224.

22. M. Avrami, Granulation, phase change, and microstructure kinetics of phase change. III, J. Chem. Phys., 9(1941) 177-184.

23. T. Jacobsen and K. West, Diffusion impedance in planar, cylindrical and spherical symmetry, Electrochim. Acta, 40(1995) 255-262.

24. H. Kaneko, W. C. Maskell and B. C. H. Steele, Miniature oxygen pump-gauge. I. Leakage considerations, Solid State Ionics, 22(1987) 161-172.

6 Resistance of sensing electrodes

The resistance of sensing electrodes of the IROSes is discussed in this chapter. The pO_2-dependent part of the resistance of sensing electrode is determined for the composite electrode of $(La_{0.75}Sr_{0.25})_{0.95}MnO_{3\pm\delta}$ (LSM25) and 8 mol % yttria stabilized zirconia (8YSZ), with/without samaria doped ceria (SDC) impregnation, for two temperatures, 568 and 664 °C. SDC impregnation can significantly decrease the resistance of the composite electrode LSM25/8YSZ and increase the dependence of the electrode resistance on pO_2.

6.1 Introduction

The sensing electrode of oxygen sensors plays a very important role in cell performance. The resistance of sensing electrode indicates the rate of the electrode processes taking place at the sensing electrode and determines to a considerable extent the response time of an oxygen sensor. Thus quantitative evaluation of the resistance of a sensing electrode is necessary. The resistance of sensing electrode consists of a part depending on pO_2 and a part independent of pO_2. For the composite sensing electrode (CSE) based on strontium doped manganite and yttria doped zirconia such as $(La_{0.75}Sr_{0.25})_{0.95}MnO_{3\pm\delta}$ (LSM25) and 8 mol % yttria stabilized zirconia (8YSZ), the pO_2-dependent part is the major constituent of the electrode resistance [1]. Therefore it is worthwhile determining the pO_2-dependent part of the resistance of sensing electrode.

6.2 Theory

The resistance of an IROS, R_{cell}, comprises in serial the resistances of the internal reference electrode, R_{IRE}, the electrolyte, R_{Elyt}, and the sensing electrode, R_{SE}.

$$R_{cell} = R_{IRE} + R_{Elyt} + R_{SE} \tag{6.1}$$

The resistance of sensing electrode, R_{SE}, comprises two parts, according to the pO_2 dependence:

$$R_{SE} = R_{od,SE} + R_{oi,SE} \tag{6.2}$$

where $R_{od,\,SE}$ and $R_{oi,\,SE}$ denote the pO_2-dependent part and pO_2-independent part of the resistance of sensing electrode, respectively.

If the internal reference electrode is isolated hermetically from environments and the electrolyte is dense, the resistance of internal reference electrode, R_{IRE}, will not change with the pO$_2$ at the sensing electrode. In the stability test shown in chapter 4 the internal reference electrode is seen to be able to survive in a period of more than 6600 hours so it is reasonable to assume that the resistance of internal reference electrode, R_{IRE}, is unchanged in a short period such as tens of hours that usually is sufficient to perform an electrochemical test. In an IROS the electrolyte is made from a heavily doped zirconia such as yttria doped zirconia or scandia and yttria co-doped zirconia. The resistance/conductance of the electrolyte is fixed by the concentration of the dopants and is (almost) pO$_2$ independent. So if the pO$_2$ at the sensing electrode is changed, the only changed constituent of the cell resistance, R_{cell}, is the pO$_2$-dependent part of the resistance of sensing electrode, $R_{od, SE}$.

For the sensing electrode made from the composite based on strontium doped manganite and yttria doped zirconia such as LSM25/8YSZ, it is found that the resistance of the composite electrode increases with decreasing pO$_2$ [2-4]. Assuming that the pO$_2$-dependent part of the resistance of the sensing electrode based on LSM25/8YSZ can be expressed as:

$$R_{od.SE} = k_0 p_S^{-a} \, , a > 0 \tag{6.3}$$

where p_S is the pO$_2$ at the sensing electrode in a unit of bar, and k_0 and a are unknown coefficient and exponent, respectively, then the resistance difference of sensing electrode when p_S is varied from 1 bar is:

$$R_{od,SE} - R_{od,SE,0} = k_0 (p_S^{-a} - 1) \tag{6.4}$$

where $R_{od, SE, 0}$ denotes the pO$_2$-dependent part of the resistance of sensing electrode when p_S equal to 1 bar.

In an IROS, only the pO$_2$-dependent part of the resistance of sensing electrode varies with pO$_2$, so the left hand side of Eq. (6.4) is equal to the corresponding variation in the cell resistance, meaning:

$$R_{od,SE} - R_{od,SE,0} = R_{cell} - R_{cell,0} \tag{6.5}$$

where $R_{cell, 0}$ indicates the cell resistance when p_S equal to 1 bar. In the light of Eq. (6.3) and (6.5), one has:

$$k_0 (p_S^{-a} - 1) = R_{cell} - R_{cell,0} \tag{6.6}$$

In Eq. (6.6) only two parameters, the exponent a and the coefficient k_0, which characterize the pO$_2$-dependent part of the resistance of sensing electrode are unknown and they can be determined from measuring the differences in cell resistance when the pO$_2$ at sensing electrode, p_S, varies from 1 bar.

6.3 Experimental

Three cells were fabricated with details given in chapter 3. The cell structures were: IRE/ScYSZ/CSE (cell 1), IRE(SDC)/ScYSZ/CSE(SDC) (cell 2), and IRE/ScYSZ/CSE(SDC) (cell 3), respectively. In the notations of cell structure, '(SDC)' to the right of electrode means that the electrode has SDC impregnation, and 'CSE' denotes the composite sensing electrode made from LSM25/8YSZ. The three cells were tested in one batch in the alumina test house shown in chapter 4. Provided the electrolyte is an (almost) pure oxide ion conductor, which is the case for ScYSZ, the cell voltage, V_{cell}, the pO_2 at internal reference electrode, p_R, and the pO_2 at sensing electrode, p_S, satisfy the Nernst equation:

$$V_{cell} = \frac{RT}{4F} \ln \frac{p_S}{p_R} \tag{6.7}$$

To make cells functional, their internal reference electrodes must be reduced. Reduction of the internal reference electrodes was carried out by applying a cell voltage of 0.9 V at 664 °C for 65 minutes. The formation of the binary mixture of Ni/NiO made the cell immediately have a stable and well defined open circuit voltage (OCV), which was very close to the thermodynamic value [5]. The impedance spectra of these cells were measured at a variety of pO_2 and the electrochemical impedance spectroscopy was performed with a voltage equal to the OCV of the cell.

6.4 Results

Figure 6.1 shows two impedance spectra of cell 1. The two spectra, Z_1 and Z_0, were measured when p_S=0.0164 and 1 bar, respectively and the temperature was 664 °C. Both spectra had no intercept on the real axis, but it is evident that the cell resistance increased when decreasing the pO_2 at the sensing electrode. Figure 6.2 shows the difference impedance spectrum difference (DIS) of Z_1 and Z_0, DIS= Z_1(p_S=0.0164 bar)-Z_0 (p_S=1 bar), which is a slightly suppressed semicircle. The intercepts of high frequency and low frequency can be recognized. Noticeably the intercept of high frequency was very closes to the origo. From the two intercepts, the difference of the cell resistance, R_{cell}-$R_{cell,0}$, which is equal to the difference of the pO_2-dependent part of the resistance of sensing electrode, $R_{od, SE}$-$R_{od, SE,0}$, is determined to be 10.7 $\Omega \cdot cm^2$. Figure 6.3 shows the difference impedance spectra measured on the cell with the sensing electrode impregnated by SDC. The difference resistance of the sensing electrode is seen to decrease significantly and the summit frequency of the difference impedance spectra

was increased from 11 to 20 Hz. Figure 6.4 shows the difference impedance spectra measured at a lower temperature of 568 °C. The summit frequency of the difference impedance spectra is decreased to 2.5 Hz and the difference resistance is increased to ca. 15 $\Omega \cdot cm^2$.
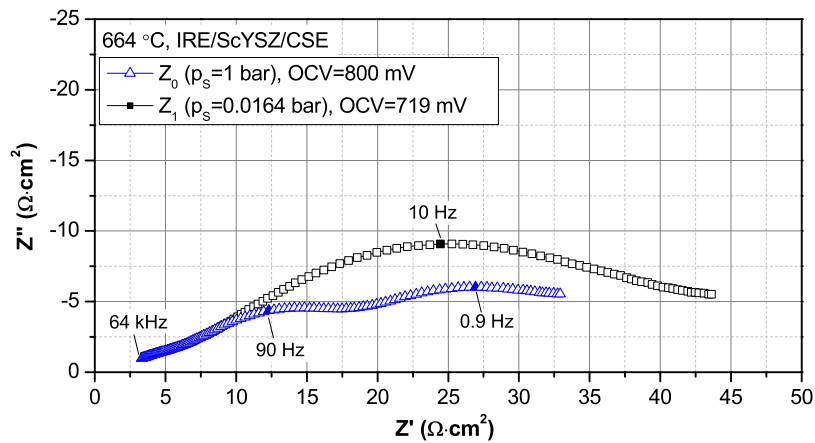

Figure 6.1. Impedance spectra of an IROS with a structure of IRE/ScYSZ/CSE. The Impedance spectra were measured with p_S=1 and 0.0164 bar, respectively. The open circuit voltages of the cell were 800 and 719 mV when p_S was 1 and 0.0164 bar, respectively. The nominal voltages calculated by FactSage[TM] 5.5 [6] are 801 mV for p_S=1 bar and 718 mV for p_S=0.0164 bar. The nominal and the measured values agree very well. The intercepts of the two spectra on the real axis were not retrievable, but it is evident that the cell resistance increased with decreasing the pO_2 at the sensing electrode.
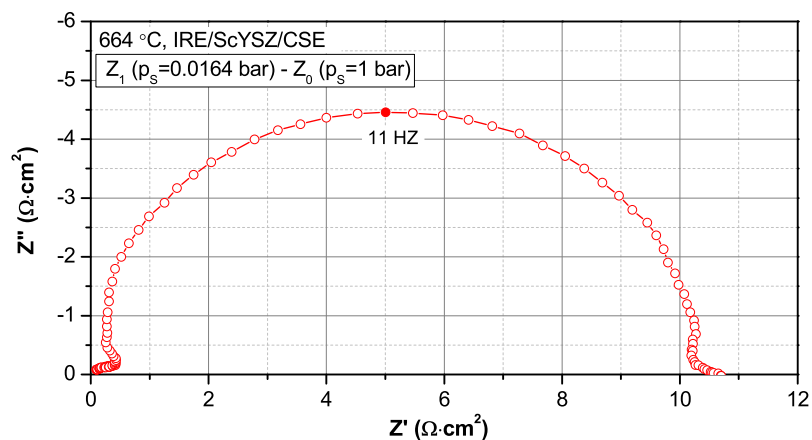
Figure 6.2. The difference impedance spectra of two impedance spectra that were measured for p_S=0.0164 and 1 bar and shown in Figure 6.1. The cell structure was IRE/ScYSZ/CSE. The intercepts on the real axis can be obtained easily.

Figure 6.3. The difference impedance spectra measured on the cell with a structure of IRE(SDC)/ScYSZ/CSE(SDC). With SDC impregnation into the sensing electrode the difference resistance is decreased and the summit frequency of the difference impedance spectra is increased.

Figure 6.4. The difference impedance spectra (DIS) at a lower temperature of 568 C. The cell structure is IRE(SDC)/ScYSZ/CSE(SDC). The difference resistance is increases substantially and the summit frequency of the difference impedance spectra is decreased.
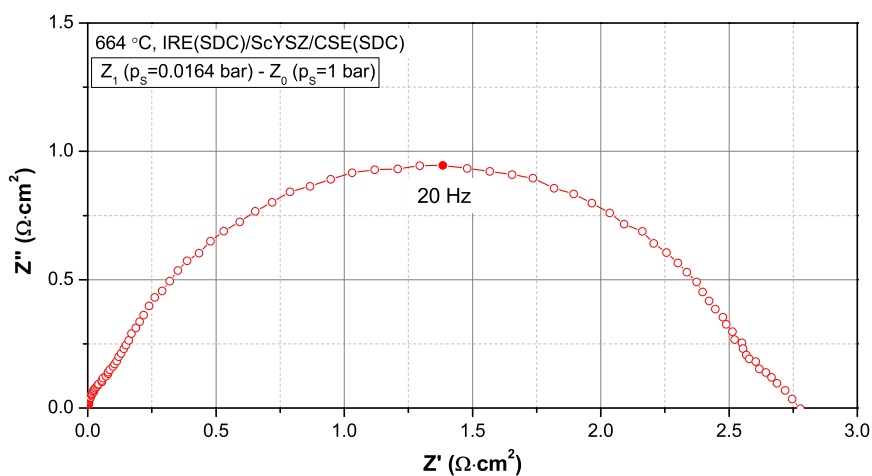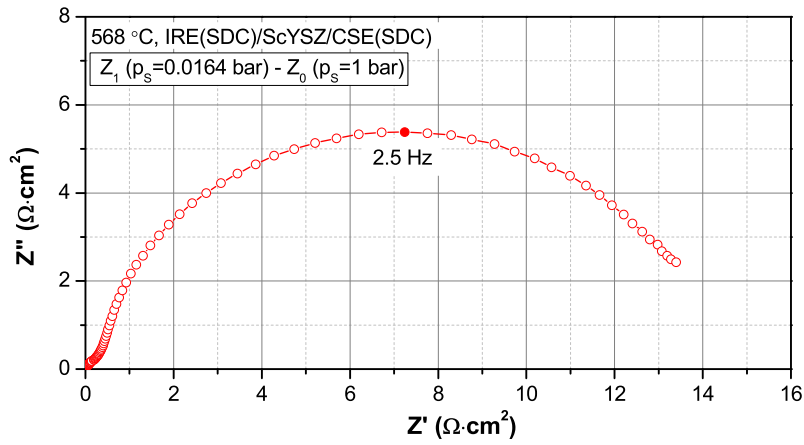
Changing the pO_2 at the sensing electrode to 2.10×10^{-1}, 7.69×10^{-2}, 1.64×10^{-2} and 1.5×10^{-4} bar, respectively, four resistance differences can be obtained. Fitting these resistance differences to Eq. (6.6), the parameters, a and k_0, were determined: $a=0.31\pm0.01$ and $k_0=4.01\pm0.41$. Therefore the resistance of the sensing electrode can be calculated as:

$$R_{od,SE} = (4.01 \pm 0.41) p_S^{-(0.31 \pm 0.01)} \tag{6.8}$$

Similar procedures were applied to measurements carried out at 568 °C and with other two cells, cell 2 and 3, whose structures were IRE(SDC)/ScYSZ/CSE(SDC) and IRE/ScYSZ/CSE(SDC), respectively. Fit results are summarized in Table 6.1. The exponent, a, is larger for the electrodes impregnated by SDC. Decreasing the temperature the coefficient, k_0, increased rapidly but the exponent, a, changed a little. Figure 6.5 and 6.6 shows the measured resistance difference and the corresponding fit curves of three cell structures at 568 and 664 °C, respectively. The measured and the fitted results agree well.

Table 6.1. The parameters in equation $R_{od,SE} = k_0 p_S^{-a}$ obtained at two temperatures, 568 and 664 °C, and on three cell structures.

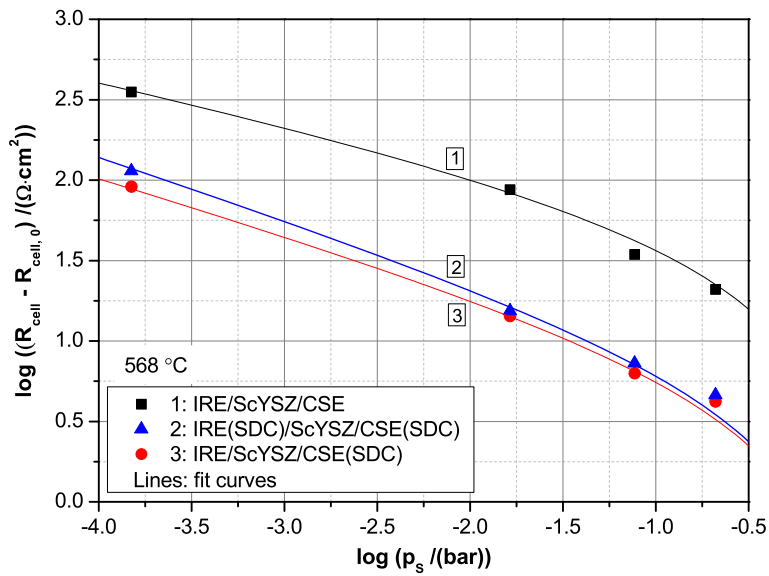| Cell No.	Cell structure	568 °C		664 °C	
		k_0	a	k_0	a
1	IRE/ScYSZ/CSE	49.43±8.92	0.24±0.02	4.01±0.41	0.31±0.01
2	IRE(SDC)/ScYSZ/CSE(SDC)	4.31±0.50	0.38±0.01	0.81±0.02	0.36±0.01
3	IRE/ScYSZ/CSE(SDC)	4.65±0.44	0.34±0.01	0.16±0.01	0.55±0.01

Figure 6.5. Measured resistance differences and fit curves of three cell structures at 568 °C. The parameters used in the fit curves are listed in Table 6.1.
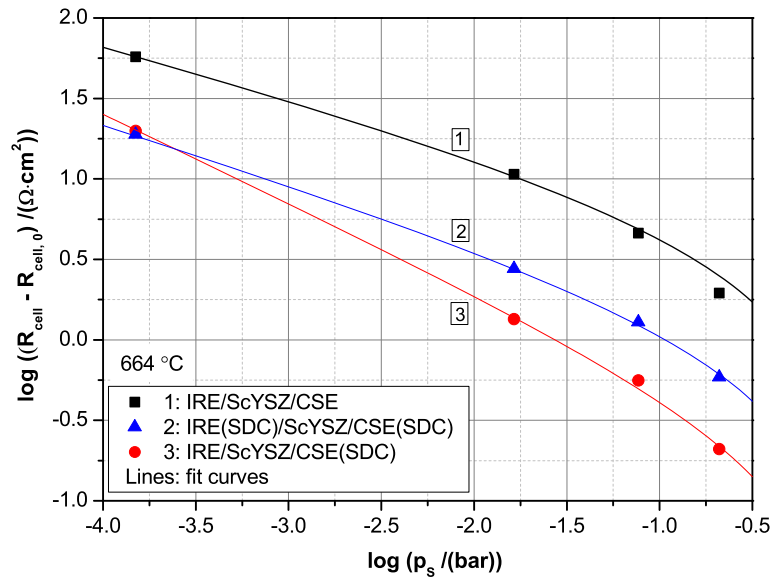
Figure 6.6. Measured resistance differences and fit curves of three cell structures at 664 °C. The parameters used in the fit curves are listed in Table 6.1.

6.5 Discussion

The resistance of the sensing electrode should not depend on the internal reference electrode. But parameters listed in Table 6.1 are different for cell 2 and 3 that both have an SDC impregnated sensing electrode. That is believed to be caused by the different amount of SDC impregnation. In cell 3 only the sensing electrode was impregnated and the amount of SDC is exactly determined to be 3 mg·cm^2. In cell 2 the exact impregnation amount is not known for individual electrodes, as both electrodes were impregnated at the same time. The total impregnation amount of cell 2 was 7.6 mg·cm^2 that is smaller than the sum of usual impregnation amounts of the internal reference electrode, 6 mg·cm^2 and the sensing electrode, 3 mg·cm^2. The sensing electrode of cell 2 is very likely to have less SDC impregnation than that of cell 3. It is seen in Figure 6.5 and 6.6 that the measured resistance differences of cell 2 are between those of cell 1 and 3 in most of pO$_2$ regions.

The impregnation of SDC decreases the pO$_2$-dependent part of the resistance of sensing electrode significantly, and therefore the resistance of the sensing electrode. At 664 °C and p$_S$=1 bar, the pO$_2$-dependent part of the

resistance of the composite electrode LSM25/8YSZ is 4.0 $\Omega\cdot cm^2$, but it can be decreased to 0.2 $\Omega\cdot cm^2$ if the composite of LSM25/8YSZ is impregnated by SDC, as calculated from the parameters of cell 1 and 3 given in Table 6.1. It is noticeable that the impregnation of SDC increases the pO_2 dependence of the electrode resistance. The exponent of the unimpregnated electrode is 0.31 at 664 °C while it is 0.55 for the SDC impregnated electrode. The coefficient, k_0, is seen to increase rapidly when the temperature is decreased, which is expected as this coefficient should reflect a thermal activated process.

The pO_2-dependent part is the major constituent of the resistance of the sensing electrode based on the composite of strontium doped manganite and yttria doped zirconia [1]. Consequently, the resistance of the sensing electrode may be approximated by its part dependent on pO_2. Thus the parameters listed in Table 6.1 may be used to calculate the resistance of the composite sensing electrodes.

As the influence of any electrode process that is pO_2 independent, i.e. the ohmic resistance, will be eliminated in the difference impedance, the intercept of high frequency of the difference impedance spectrum may be used to examine the validity of the method used in this chapter. Including the difference impedance spectrum shown in Figure 6.2, all the difference impedance spectra used to get the parameters listed in Table 6.1 have the intercept of high frequency very close to, if not at, the origo.

6.6 Conclusion

The pO_2-dependent part of the resistance of sensing electrode is determined for three cell structures at two temperatures, 568 and 664 °C. The validity of measurements can be examined by the intercept of high frequency in the difference impedance spectra. SDC impregnation can significantly decrease the resistance of the composite electrode LSM25/8YSZ and increase the dependence of the electrode resistance on pO_2.

References

1. M. J. Jørgensen and M. Mogensen, Impedance of Solid oxide fuel cell LSM/YSZ composite cathodes, J. Electrochem. Soc., 148 (2001) A433-A442.

2. S. P. Jiang, Activation, microstructure, and polarization of solid oxide fuel cell cathodes, J. Solid State Electrochem., 11 (2007) 93–102.

3. S. P. Jiang, Development of lanthanum strontium manganite perovskite cathode materials of solid oxide fuel cells: a review, J. Mater. Sci., 43(2008) 6799–6833.

4. E. V. Tsipis and V. V. Kharton, Electrode materials and reaction mechanisms in SOFC: a brief review, J. Solid State Electrochem., 12(2008) 1367-1391.

5. Q. Hu, T. Jacobsen, K. V. Hansen and M. Mogensen, Improved internal reference oxygen sensor with composite ceramic electrodes. J. Electrochem. Soc., 159(2012) B811-B817.

6. C. W. Bale, E. Bélisle, P. Chartrand, S. A. Decterov, G. Eriksson, K. Hack, I.-H. Jung, Y.-B. Kang, J. Melançon, A. D. Pelton, C. Robelin and S. Petersen, FactSage Thermochemical Software and Databases – Recent Developments, Calphad, 33(2009) 295-311.

7 General discussion and conclusion

In this chapter the results shown in pervious chapters are discussed and final conclusions drawn. It is possible to replace Pt by oxides to serve as the electrode materials in oxygen sensors. The oxide electrode can improve cell performance significantly. Attempts are made to define a standard "response time" with corresponding measurement procedures in order to reduce the uncertainty in identifying the response time and make the comparison of response times obtained from varied test conditions have a common basis. It is possible to study the response time of sensing electrode by impedance spectroscopy. Electrode processes of the internal reference electrode and the sensing electrode are coupled in the impedance spectra shown in this thesis. Techniques such as analysis of difference in impedance spectra (ADIS) and deconvolution of impedance spectra (DRT) may be used to interpret the impedance spectra.

7.1 Discussion

Pt is the dominant electrode material due to historical reasons, however, the composite electrode based on $(La_{0.75}Sr_{0.25})_{0.95}MnO_{3\pm\delta}$ (LSM25) and 8 mol % yttria stabilized zirconia (8YSZ), with/without samaria doped ceria (SDC), is verified superior in terms of an extended working temperature range (chapter 4) and a lower polarization resistance (chapter 5). It is thus possible to replace Pt by composites based on oxides. Including the advantage of a lower cost, electrode material based on oxides can be more active and more robust. For example, cobaltites such as $Sm_{0.6}Sr_{0.4}CoO_3$ and ferrites such as $La_{0.6}Sr_{0.4}Fe_{0.8}Co_{0.2}O_3$ can be more active electrode material than manganites such as lanthanum strontium manganite that are used in this thesis [1]. On the other hand, oxides such as $La_{0.4}Sr_{0.6}TiO_3$ are found more tolerant to sulfur that is poisonous to most of electrode material including Pt [2].

As seen in numerical simulations (Figure 2.8, 2.9 and 2.10 in Chapter 2) and experimental results (Figure 4.5 and 4.6 in Chapter 4), during the response time tests the variations in cell voltage and oxygen fraction are asymptotical and it is difficult to determine the exact time an experimental setup with a cell inside takes to respond completely to a pO_2 change. Thus it is worthwhile defining a standard procedure to reduce the uncertainty in identifying the response time and make the comparison of response times measured from varied test conditions have a common basis. According to the suggestion from Abrahamsen [3] , a response time "T_{99}"

may be defined as the time a cell setup takes to display 99 % of the pO_2 change when changing the sample gas from 20.9 % O_2 to 1000 ppm O_2, i.e., the time required to reach a reading below 3080 ppm O_2 with the a specified gas flow rate and N_2 as the balance gas.

It is known from the discussion of Chapter 2 that the response time measured from experiments including the part from the setup, i.e., the process of gas mixing, and the part from the cell, i.e., the electrode processes at the sensing electrode. If the gas mixing dominates the experiments the response time of sensing electrode is invisible. In the experiments performed in the larger setup (Figure 4.6 in Chapter 4), the measured response times are seen independent on temperature and cell structure. In the smaller experimental setup, the temperature dependence of response time is reveal to a discernible extent, i.e., the response time of the setup is suppressed so that the response time of the sensing electrode is observable.

The response time of a setup can be suppressed but cannot be eliminated, which increases the difficulties in determination of the response time of a sensing electrode. The response time of a sensing electrode is characterized by the capacitive contributions from electrode processes [4]. It is thus possible to study the response time of a sensing electrode by electrochemical methods such as the impedance spectroscopy. In Chapter 6, the resistances of sensing electrodes are determined by a method of impedance difference. It is known from the obtained formulae (Table 6.1) that the resistances of the sensing electrodes increase by about 4.5 times when p_S is decreased from 1 to 0.0164 bar. Therefore the difference impedance spectra made between a high and a very low pO_2, to a considerable extent, may reflect the impedance spectra of the sensing electrodes. The response time of the composite sensing electrode LSM25/8YSZ, with SDC impregnation, is supposed be in a range of 0.1 – 10 seconds since its contribution to the observed response time is discernible but not dominant and the observed response time (cell and setup) is around 30 seconds, as seen in Figure 4.5. The summit frequencies of the difference impedance spectra measured on an identical cell structure is 20 and 2.5 Hz at 664 and 568 °C, respectively, as seen from Figure 6.3 and 6.4, which correspond to the response times of the sensing electrodes of 0.05 and 0.4 seconds, respectively. The response times indicated by the impedance spectroscopy are a bit lower but close to the supposed ones.

The impedance spectra of sensing electrodes are not separated from the impedance spectra of whole cell in this thesis. As seen in Chapter 5 and 6 the impedance spectra of the whole cell vary with pO_2 at the sensing electrode and the reduction degree of NiO that means the electrode processes of the internal reference electrode and the sensing electrode couple\overlap in the impedance spectra under the investigation conditions. In order to reduce the uncertainty in determining the resistance of the sensing electrodes, the pO_2-dependent part of the resistance

of sensing electrode is determined by the method of impedance difference (see Chapter 6) instead of the method of directly fitting the spectra by equivalent circuits. However, it is worthwhile attempting to identify and separate the individual electrode processes from the impedance spectra of the whole cell by the techniques such as differential impedance analysis (DIA) [5, 6], deconvolution of impedance spectra (DRT) [7] and analysis of difference in impedance spectra (ADIS) [8]. The method used in Chapter 6 may be regarded as a simplified case of ADIS and it uses the difference impedance spectra to determine the pO_2-dependent resistance of the sensing electrodes.

7.2 Conclusion

IROSes of excellent performance are demonstrated. The composite sensing electrodes based on LSM25/8YSZ, with/without SDC impregnation, are verified superior to Pt in terms of a lower polarization resistance and an extended working temperature range. IROSes show high accuracy, good stability, fast response, good tolerance to thermal and pO_2 cycling and easy recoverability when Ni is depleted. Both cell fabrication and performance show good reproducibility. Apart from the excellent performance the IROSes are fabricated by an inexpensive and flexible method, therefore the IROSes presented in this thesis may be commercialized in the future.

Though the electronic leak of the electrolyte of an IROS is usually unavoidable, it can be minimized to make the depletion period satisfy the target application up to duration of years. The methods that may be used to modify the depletion period of an internal reference electrode include adjusting the electrolyte thickness and the amount of metallic Ni in the internal reference electrode.

As the reference pO_2 that is the equilibrium pO_2 of Ni/NiO for the cells of this thesis depends on temperature, errors in pO_2 measurement are sensitive to errors in temperature measurement. Errors in temperature measurement can be mitigated by optimized cell assembly design.

The response time of an experimental setup may make the response time of a sensing electrode invisible, it is worthwhile defining a standard measurement procedure to reduce the uncertainty in identifying the response time and make the comparison of response times measured from varied test conditions have a common basis. It is possible to determine the response time of a sensing electrode by impedance spectroscopy.

The kinetics of electrochemical reduction of NiO can be described by the Avrami equation. The electrochemical reduction of NiO may require an induction period. The maximum reaction rate is obtained when 2 - 11 % NiO is reduced. The increasing resistance in NiO reduction can be exclusively ascribed to one arc in impedance spectra. The pO_2-dependent part of the resistances of composite sensing electrodes is determined. SDC impregnation reduces significantly the polarization resistance of the composite of LSM25/8YSZ.

References

1. E. V. Tsipis and V. V. Kharton, Electrode materials and reaction mechanisms in SOFC: a brief review, J. Solid State Electrochem., 12 (2008) 1367-1391.
2. R. Mukundan, E. L. Brosha, and F. H. Garzon, Sulfur Tolerant Anode for SOFCs, Electrochem. Solid-State Lett., 7(2004) A5-A7.
3. R. B. Abrahamsen, IROS tailored for handheld application, personal communication(2011).
4. A. Lund, Robust high temperature oxygen sensor electrodes, PhD thesis, Techinical University of Denmark, Kongens Lyngby, Denmark (2011).
5. A. Barbucci, M. Viviani, P. Carpanese, D. Vladikova and Z. Stoynov, Impedance analysis of oxygen reduction in SOFC composite electrodes, Electrochim. Acta, 51(2006) 1641-1650.
6. D. Vladikova, P. Zoltowski, E. Makowska and Z. Stoynov, Selective study of the differential impedance analysis-comparison with the complex non-linear least squares method, Electrochim. Acta, 47(2002) 2943-2951.
7. H. Schichlein, A.C. Müller, M. Voigts, A. Krügel and E. Ivers-Tiffёe, Deconvolution of electrochemical impedance spectra for the identification of electrode reaction mechanisms in solid oxide fuel cell, J. Appl. Electrochem., 32(2002) 875–882.
8. S. H. Jensen, A. Hauch, P. V. Hendriksen, M. Mogensen, N. Bonanos, and T. Jacobsen, A Method to Separate Process Contributions in Impedance Spectra by Variation of Test Conditions, J. Electrochem. Soc., 154(2007) B1325-B1330.

8 Outlook

This chapter presents an outlook on cell fabrication and optimization. Attempts to develop the IROS into a self-supported style and a chip style are outlined. It is possible to use the concepts and fundamentals obtained from IROS to develop internal reference sensors detecting other gas species such as hydrogen, chlorine and bromine. Parts of this chapter are included in a filed patent application, "Novel internal reference electrode and novel sensing electrode for an internal reference oxygen sensor, sensor employing same and use of the sensor", EP81909JHtra.

8.1 Cell fabrication and optimization

Fabrication procedures given in Chapter 3 are not optimized. For fabrication of the internal reference electrode, both composition and heat treatment schemes can be further improved. Experiments have shown that the polarization resistance of a cell can be decreased significantly if the sintering temperature is lowered to 1300 ºC from 1350 ºC that is used so far for preparing the internal reference electrode. Experimental results have shown that a lower polarization resistance and an equally accurate response can be achieved by replacing 8YSZ by gadolinia doped ceria (GDC) and adjusting the ratio of NiO to 8YSZ. A systematic study on optimizations needs to be carried out in the future.

The binary mixture of Ni/NiO is selected in this study as other candidate binary mixtures were reported not to work well, without concrete reasons. As discussed in Chapter 2, the equilibrium pO_2 of other binary mixtures such as Fe/FeO and Co/CoO have a smaller dependence on temperature. It is worthwhile practicing these binary mixtures.

The microstructure of the sensing electrode also needs to be further improved as agglomerates of LSM/8YSZ were found to distribute non-uniformly within the sensing electrode that may account for the considerable contribution of the sensing electrode to the polarization resistance of the whole cell. It is possible to reduce the resistance of the sensing electrode by optimizing the ink preparation and the heat treatment schemes.

The composite electrodes based on LSM25/8YSZ have been proved superiors over Pt to serve as the sensing electrode. It is possible to develop electrode materials based on oxides for particular applications. For example, the pO_2 measurement in an environment with high content of sulfur has been a challenge for oxygen sensors based on Pt. The oxides based materials such as $La_{0.4}Sr_{0.6}TiO_3$/YSZ [1] and terbia doped YSZ [2, 3], have been found sulfur resistant as electrode materials. As oxygen sensors are usually used in an environment with a high content of sulfur, it is worthwhile carrying out studies to equip an IROS with a specific sensing material more tolerant towards sulfur. Furthermore oxides more tolerant towards phosphorus and carbon (deposition) may also be developed and applied to IROSes.

The glass, YS2B, used for the seal is selected for a low temperature application, i.e., < 600 ºC that was prescribed on initiation of the PhD project. As successful prototypes of IROSes have been demonstrated, studies on cells applicable at a higher temperature such as > 800 ºC may be worthwhile. In this case the glass needs further development.

8.2 Electrode processes

Electrode processes of an IROS need to be further studied. Interpretation of the impedance spectra of whole cell requires further work to indentify individual contributions from the internal reference electrode and the sensing electrode. Both the larger setup and the smaller setup used in this thesis are not suitable for the study on the response time of the sensing electrode as the gas mixing in the setups hid the response of the sensing electrodes. The numerical simulation developed in Chapter 2 can be used to preliminarily estimate the time of gas mixing and thus may be helpful to design a suitable experimental setup.

8.3 Self-supported cells for portable applications

IROSes can be fabricated with/without a thermocouple as shown in Chapter 3. Nevertheless an operation of these cells needs an external heat source to maintain a temperature high enough to make the cell functional. These external heat sources comprise usually a furnace and are too cumbersome for a portable application.

It is possible to develop an IROS for portable applications. A self-supported IROS is designed and illustrated in Figure 6.1. The cell is equipped with a thermocouple and a heater. With a heater integrated the external heat source such as the furnace is not required anymore. Additionally the temperature distribution of the cell may be more uniform if the distribution of the heaters is optimized.
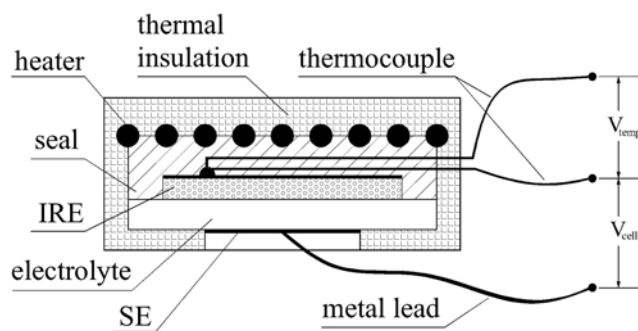
IRE: internal reference electrode
SE: sensing electrode
V_{cell} : voltage between IRE and SE, a measure of pO_2
V_{temp} : voltage of the thermocouple, a measure of cell temperature

Figure 8.1. A self-supported IROS with an integrated thermocouple and heater.

The heater can be designed to be an independent unit. Figure 8.2 shows a heater with the heating elements screen printed on both sides of the heater board. Oxides such as $(La_{0.45}Sr_{0.45}MnO_3)$ may be used as the heating element due to a relatively large resistivity. The minimum resistivity of $La_{0.45}Sr_{0.45}MnO_3$ is 3.13×10^{-5} $\Omega \cdot m^{-1}$ at 300 °C, and the resistivity increases with increasing temperature when it is above 300°C [4], which is very important for the reason of safety. If the heater is overheated, the current of the heater will decrease due to the increasing resistivity. It needs to be noted that Pt and nichrome are not suitable heating element in this case as their resistivity is too low. The resistivities of Pt and nichrom are 1×10^{-7} and 1.5×10^{-6} $\Omega \cdot m^{-1}$, respectively, much lower than that of $La_{0.45}Sr_{0.45}MnO_3$. A low resistivity indicates a large length of the heating element, not helpful to reduce the heater size.

A preliminary design shows that with 2 - 3 pieces of the heaters shown in Figure 8.2 the temperature of whole cell assembly, in a size of Φ 10×10 cm including the thermal insulation, can reach 400 ºC in ca. 7 minutes, and the power consumption is ca. 1.5 W.
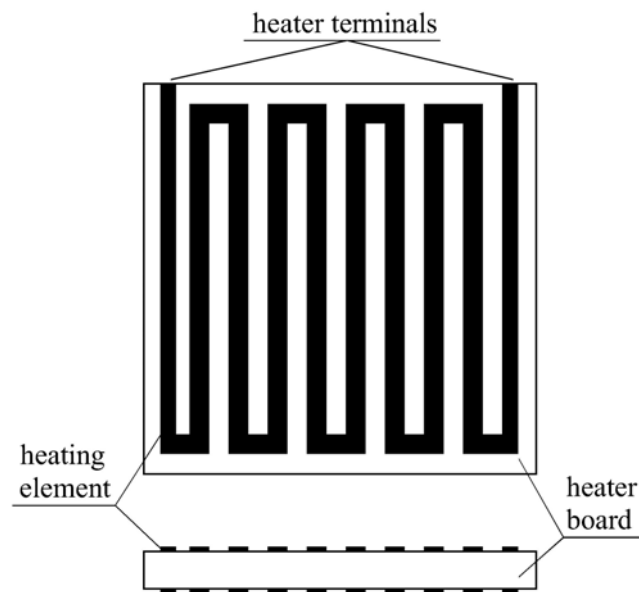
Figure 8.2. An independent heater that may be used for the self-supported IROS. The heating elements that may be made from $La_{0.45}Sr_{0.45}MnO_3$ are screen printed on both sides of the heater board.

8.4 Chip applications

It is possible to further miniaturize the IROS for a chip application, as illustrated in Figure 8.3. The fabrication techniques may refer to those widely used in chip industries such as photolithography, pulsed laser deposition (PLD) and chemical vapor deposition (CVD). A substrate such as a silicon wafer may be etched to form a layered cavity on which the internal reference electrode, the electrolyte and the sensing electrode are deposited in sequence. Apart from the function of supplying oxide ion conduction, the electrolyte in this case also serves as a seal for the internal reference electrode. The circuits used to read cell voltage can be easily realized in this design. The thickness of entire assembly can be less than 0.3 mm.
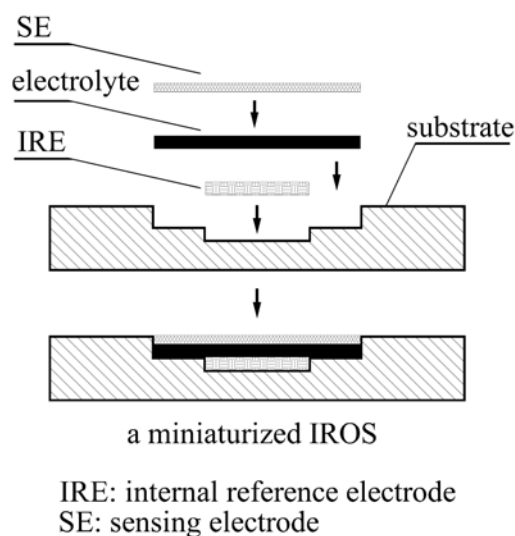
Figure 8.3. The chip design of an IROS. A substrate such as a silicon wafer is etched to form a layered cavity on which the IRE, the electrolyte and the SE are deposited in sequence. The thickness of entire assembly can be less than 0.3 mm.

8.5 Internal reference sensors for other gas species

The concepts and fundamentals revealed in this thesis may be extended to cells detecting other gas species. For example, it may be possible to develop an internal reference hydrogen sensor that uses the binary mixture of metal and its hydride, i.e., Al/AlH_3, Ca/CaH_2 and Mg/MgH_2 to provide the reference pH_2, and proton conductors made from calcium, strontium and/or barium zirconates [5, 6] can serve as the electrolyte. Similarly, internal reference sensors detecting chlorine and bromine might be developed.

References

1. R. Mukundan, E. L. Brosha, and F. H. Garzon, Sulfur Tolerant Anode for SOFCs, Electrochem. Solid-State Lett., 7(2004) A5-A7.
2. E. L. Brosha, Amperometric oxygen sensors based on dense Tb–Y–Zr–O electrodes, Solid State Ionics, 109(1998) 73–80.

3. E. L. Brosha, R. Mukundan, D. R. Brown, and F. H. Garzon, Sulfur resistant oxygen sensors for industrial boiler control, Electrochem. Soc. Proc., 99-13 (1999), 374-381.

4. A. Mackor, T. P. M. Koster, J. G. Kraaijkamp, J. Gerretsen, Influence of La-substitution and – substoichiometry on conductivity, thermal expansion and chemical stability of Ca- or Sr- doped lanthanum manganites as SOFC cathodes, Proceedings of the second international symposium on solid oxide fuel cells, (1991) 463-471.

5. H. G. Bohn and T. Schober, Electrical conductivity of the high temperature proton conductor $BaZr_{0.9}Y_{0.1}O_{2.95}$, J. Am. Ceram. Soc., 83(2000) 768-772.

6. H. Iwahara, T. Yajima, T. Hibino, K. Ozaki and H. Suzuki, Protonic conduction in calcium, strontium and barium zirconates, Solid State Ionics, 61(1993) 65-69.

Publications

1. Q. Hu, K. V. Hansen, M. Mogensen, Novel Internal Reference Electrode and novel Sensing Electrode for an Internal Reference Oxygen Sensor, Sensor employing same and Use of the Sensor, EP81909JHtra (filed).

2. Q. Hu, T. Jacobsen, K. V. Hansen, M. Mogensen, Improved Internal Reference Oxygen Sensors with Composite Ceramic Electrodes, J. Electrochem. Soc., 159(2012) B811-B817.

3. Q. Hu, T. Jacobsen, K. V. Hansen, M. Mogensen, The depletion period due to an electronic conduction of the electrolyte of the internal reference oxygen sensor, Solid State Ionics, (submitted).

4. Q. Hu, T. Jacobsen, K. V. Hansen, M. Mogensen, Electrochemical reduction of NiO in a composite electrode, Solid State Ionics, (submitted).